Development of Gas Circuit Breaker Chambers with Low Operating Energy Based on Gas-Flow Simulation

Tadashi Mori

The Thesis submitted to Nagoya University

February 2011

Contents

Chapter 1 Introduction

1.1 Background

Demands for electric power have greatly increased in the 1980s and 1990s and power networks have expanded. In Japan, for example, the power-system voltage has risen to 550 kV. To safely and efficiently operate power-systems, substations have been constructed in appropriate locales. The role of a substation is to switch between transmission lines and to change the voltage levels. For the switching task, circuit breakers (CBs) are one of the important substation components. The CBs must interrupt all types of currents such as large fault currents, load currents, small capacitive currents, etc. In Japan, the electric power-system has been designed so that any eventual fault current to be interrupted does not exceed 63 kA.

In earlier periods, oil- or air-insulated CBs were used for power networks. In the USA, SF_6 gas circuit breakers (GCBs) were first adopted in the 1950s because they were expected to provide good dielectric insulation characteristics and high current interruption performance. Since then, many research efforts have been devoted to the study and development of GCBs.

This thesis describes various contributions to the fundamental research and development of GCBs.

1.2 Typical structure and operation of conventional GCBs

1.2.1 Typical structure of puffer-type GCBs

The early SF_6 GCBs had a gas tank that contained, for example, a reserve of 20 MPa high-pressure gas, which was blasted to extinguish arcs. Under these conditions, the high-pressure

SF_6 gas liquefies, even at room temperature. Thus, reserved-tank-type GCBs needed equipment not only to maintain the high pressure but also to vaporise the liquefied SF_6 gas, and this equipment was complex and expensive. However, these GCBs became obsolete after puffer-type GCBs were invented, which were widely adopted because of their simple structure.

Figure 1.1 shows a typical structure of a puffer-type GCB enclosed by a dead tank. This type of GCB has an operating mechanism to drive movable parts including movable contacts, a puffer cylinder, and a nozzle. The movable contacts consist of arcing contacts and a main contact. Corresponding to the movable contacts, the GCB has a stationary arcing contact and a stationary main contact. The tips of the arcing contacts are usually made of copper tungsten, and the nozzle is made of polytetrafluoroethylene (PTFE).

1.2.2 Typical operation of puffer-type GCBs

Figure 1.2 shows the steps involved in opening a GCB. When a GCB is to be opened, the operating mechanism drives the movable parts towards the left side as shown in the figure. First, a movable main contact separates from the stationary main contact, and the current flows through the arcing contacts. In the second stage, the movable arcing contact separates from the stationary contact, and an arc ignites between the arcing contacts. The puffer cylinder then moves towards the operating mechanism, while the puffer piston remains stationary, so SF_6 gas in the puffer chamber is compressed, its pressure rises and it is blown into the area between the arcing contacts. Before the nozzle throat passes the tip of the stationary arcing contact, the gas can flow only towards the movable arcing contact. After the nozzle throat passes the tip of the stationary contact, the gas may flow in two directions: either towards the movable arcing contact or towards the stationary arcing contact. The arc is cooled by the gas-flow and may be extinguished successfully at current zero, thereby accomplishing current interruption.

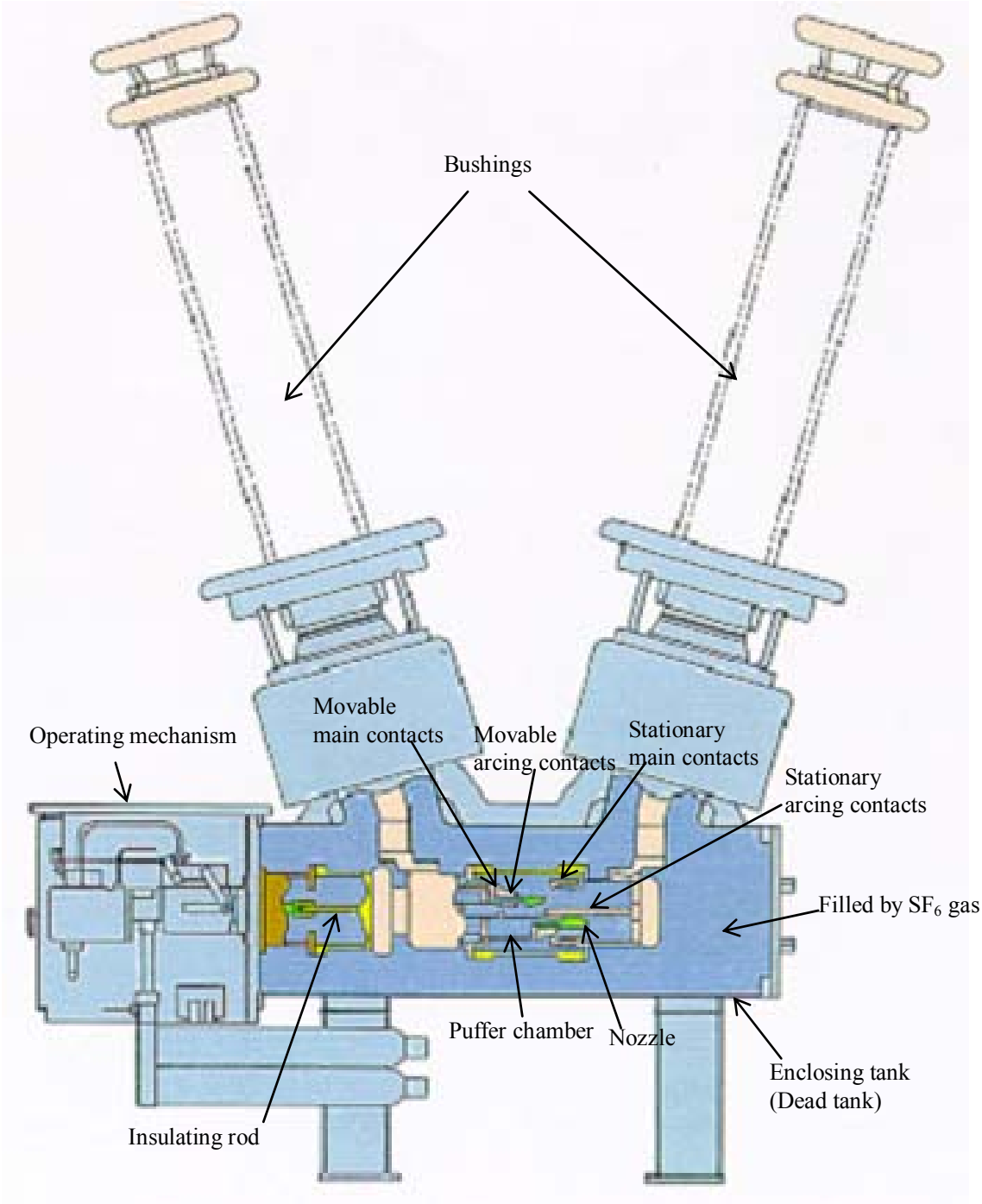

Figure 1.1 Typical structure of a puffer-type GCB

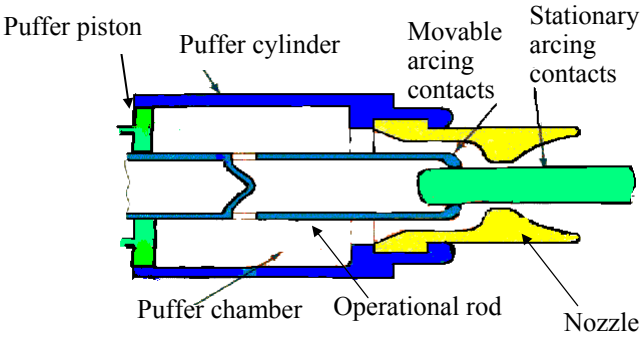

(a)Closed position

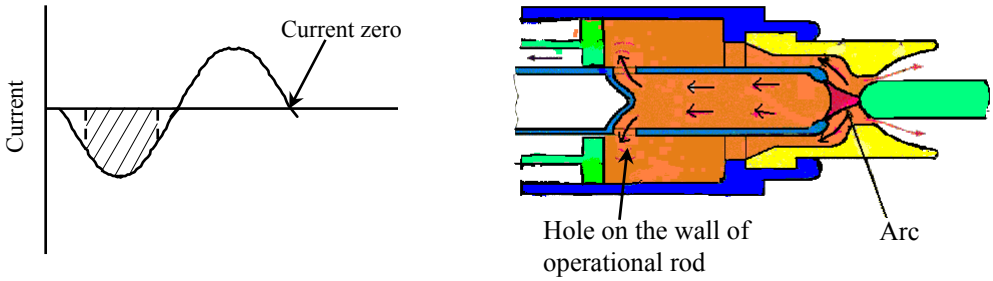

(b) Early period of interruption

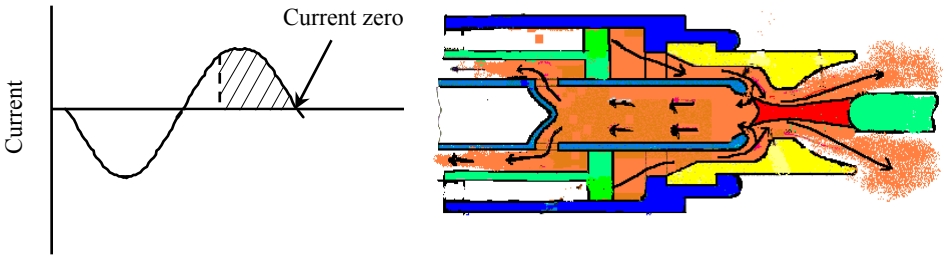

(c) End period of interruption

Figure 1.2 Interruption process of the Hybrid-puffer^{TM}-type chamber

Figure 1.3 shows examples of current waveforms and contact-separation timings for single-phase and symmetric current interruption. In Fig. 1.3(a), the contacts separate at time t_s and the current is interrupted at the current zero time $t_{zi} > t_s$. In Fig. 1.3(b), the contacts open at time t_s', which is a short time Δt_s after t_s, and the current cannot be interrupted at the

first current zero time t_{zi} because the arcing time $t_{zi}-t_s'$ is too short to successfully interrupt the current. During this short time interval, the current cannot be interrupted because the gas pressure in the puffer chamber does not reach a sufficiently high level, and the electric field is high because of the small separation between the contacts. In addition, the gas-flow is not

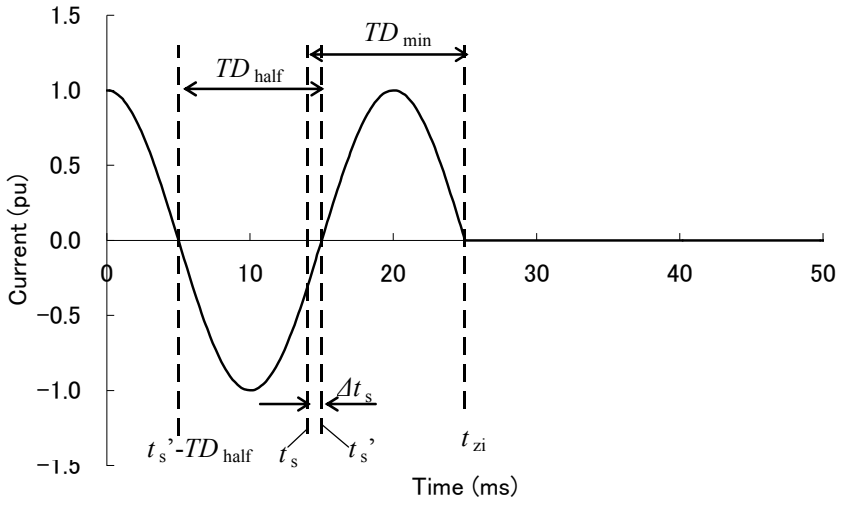

(a) Case of minimum arcing time

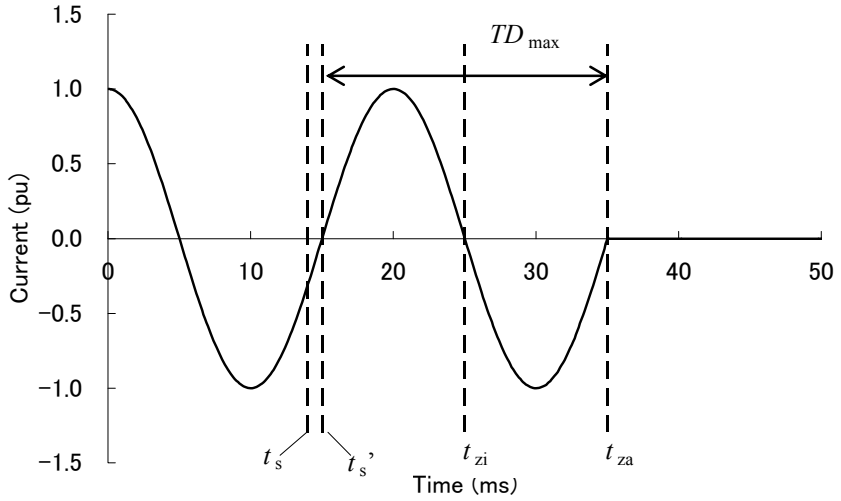

(b) Case of longest arcing time

Figure 1.3 Current waveforms and timings of contact separations

sufficient because the nozzle throat has not yet passed the tip of the stationary arcing contact. In this case, the current is interrupted at the second current zero time t_{za}, which is a half cycle from t_{zi}. The time duration $TD_{min}=t_{zi}-t_s'$ is referred to as the minimum arcing time, and the time duration $TD_{max}=t_{za}-t_s'$ is referred to as a maximum arcing time. As shown in Fig. 1.3(a), the GCB can interrupt the current at t_{zi} whenever the contacts open between $t_s'-TD_{half}$ and t_s, where TD_{half} is a half cycle of the symmetric current, which corresponds to 10 ms for a 50-Hz system and 8.3 ms for a 60-Hz system.

1.2.3 Basic GCB current-interruption phenomena

When a GCB interrupts a current that is much less than the GCB current-interruption rating, the diameter of the arc is much smaller than that of the nozzle throat. In such cases, the gas flows continuously from the puffer chamber into the arcing area, as shown in Fig. 1.4(a). However, when the arc current is large, the diameter of the arc becomes larger so that it fills the nozzle throat, as shown in Fig. 1.4(b). The gas-flow through the nozzle throat gets blocked by the arc during this time, and this situation is called 'nozzle clogging'. As the current decreases, the arc shrinks and the gas resumes flow through the nozzle throat towards the stationary arcing contact. Next, the gas-flow cools the arc and its surrounding gas, until the arc is finally extinguished at the current zero time.

1.3 Interruption requirements for GCBs

The interruption requirements for GCBs are specified by standards; for instance, those supplied by the Japanese Electrotechnical Committee (JEC), International Electrotechnical Commission (IEC), or American National Standards Institute (ANSI). The interruption requirements are generally affected by the current being interrupted and the transient recovery voltage (TRV), which is determined by the power line or apparatus that is connected and the voltage that is applied after current interruption. The most severe duty might be different for

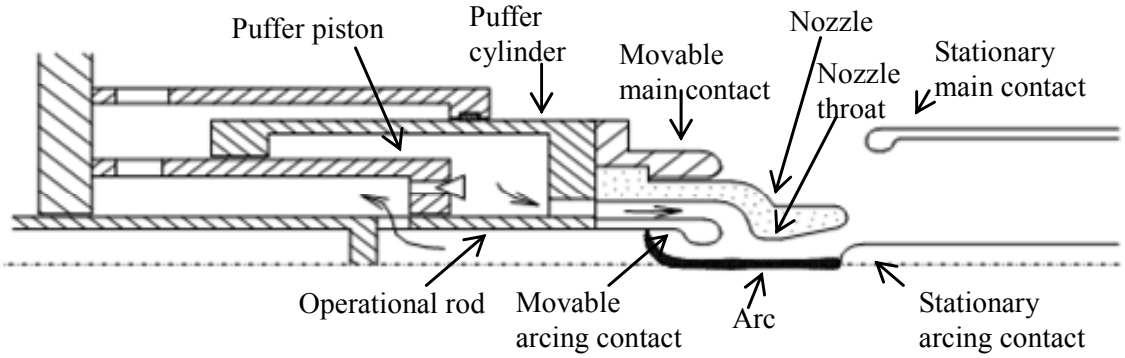

(a) Case of small current arcs

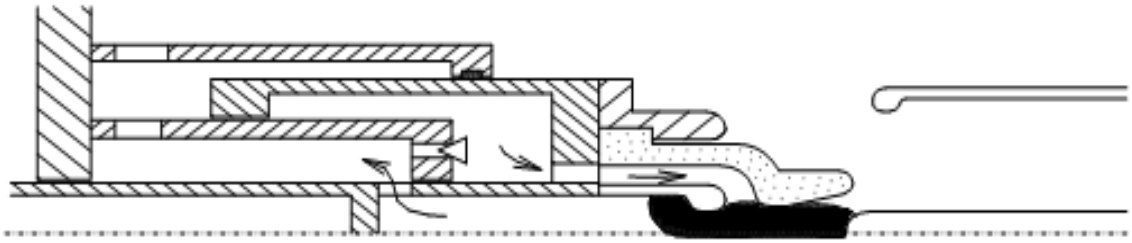

(b) Case of large current arcs

Figure 1.4 Nozzle throat clogging

each type of GCB, but the three most severe are, in general, breaker-terminal faults (BTFs), short-line faults (SLFs), and small capacitive current interruptions. Table 1.1 shows the major interruption test items required by IEC [1]. Physical phenomena and problems encountered during the execution of these duties are explained in this section.

1.3.1 BTF interruption

1.3.1.1 Phenomena in power-system

The interruption duty for a BTF corresponds to a grounding failure at a circuit-breaker terminal, as shown in Fig. 1.5. The fault current is the largest of the three major fault conditions. Thus, this fault current determines the rated interruption current for the GCB.

Table 1.1 Major interruption test items required by IEC [1]

Fault	Items	Ratio of interruption current against rated interruption current	Features
BTF	T10	10 %	Corresponding to a fault current through one transformer. Rate of rise of TRV is highest in BTF.
	T30	30 %	Corresponding to a fault current in the case of disconnecting several lines or cables. Rate of rise of TRV is relatively high.
	T60	60 %	Corresponding to a fault current in the case of disconnecting several lines or cables, and a larger fault than T30. Rate of rise of TRV is lower than that of T30.
	T100s	100 %	Corresponding to a short circuit current in the case of connecting all of transformers and lines.
	T100a	100 %	Same case with T100s, but the current includes DC component.
SLF	L75	75 %	Corresponding to a fault with short line. Interruption current is 75 % of rated interruption current Rate of rise of initial TRV is high, but lower than that of L90.
	L90	90 %	Interruption current is 90 % of rated interruption current Rate of rise of initial TRV is high..
Small capacitive current	LC/CC	Less than several %	Corresponding to interrupting cables or lines without loads. Interruption current is up to several hundreds amperes. Recovery voltage is high.

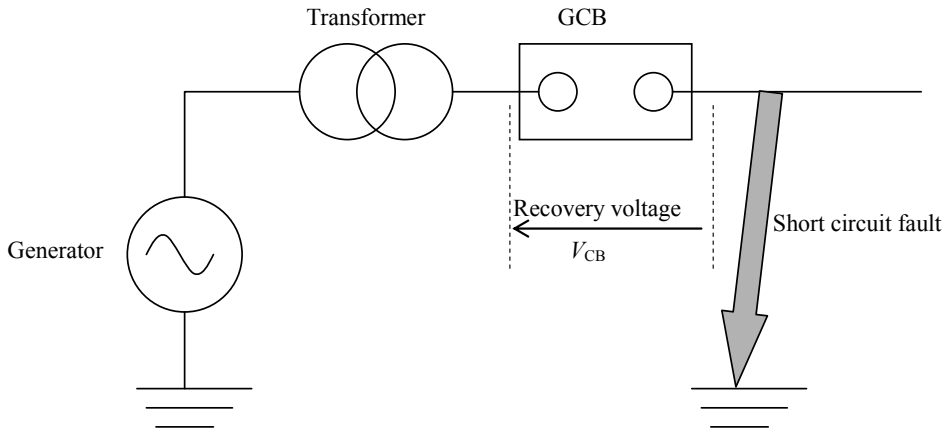

Figure 1.5 Schematic circuit of BTF

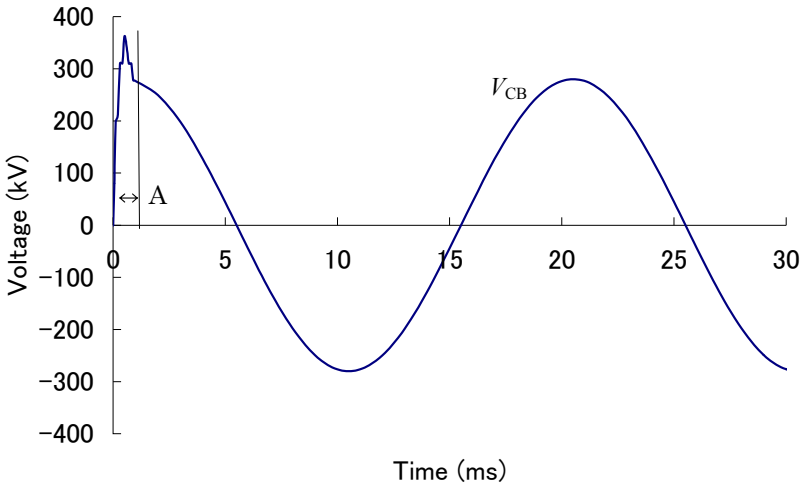

(a) Recovery voltage

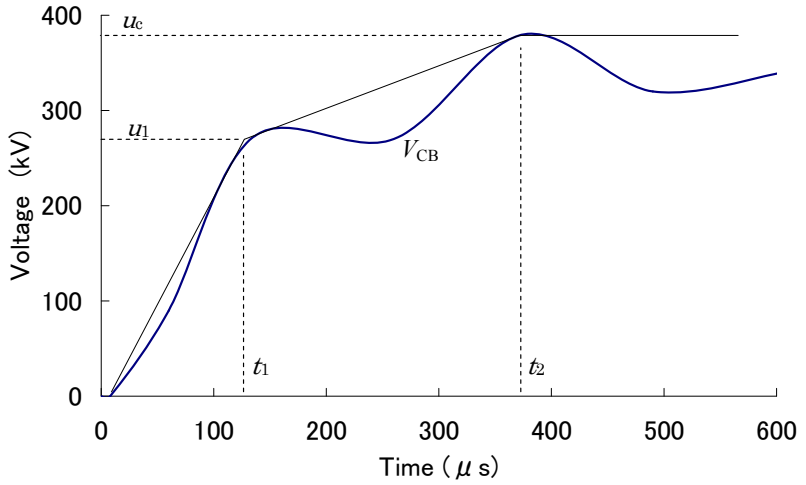

(b) Expanded figure of time duration 'A'

Figure 1.6 Schematic figure of TRV

The interruption-current rating represents an rms value of a symmetric current component and DC component. At the same time, a relatively high TRV is implied on the terminal source side because of the impedance of the transformers. Figure 1.6 shows an example of a TRV waveform, which can sometimes include high-frequency oscillations. To represent the TRV waveform, the standards specify a first reference voltage u_1, which occurs at t_1, and a TRV

peak value u_c, which occurs at t_2, as shown in Fig. 1.6(b). The rate of rise in the TRV is defined by u_1/t_1. As examples, the standard values of prospective TRV of T100s for 245-kV 50-kA GCB are 195 kV for $\boldsymbol{u}_1$, 98 μs for t_1, 364 kV for u_c, and 392 kV for t_2, then the u_1/t_1 is 2.0 kV/μs. The T100s corresponds to fault currents for the case of all of transformers and lines being connected at a large-capacity substation. When a GCB interrupts the current through transformers, or when a GCB is installed in smaller-capacity substations, the current becomes smaller than T100s or T100a, and the TRV becomes higher. IEC defines T10, T30, and T60 as 10%, 30%, and 60% of the interrupting current of T100s, respectively. Generally, T100s and T100a represent the most severe conditions for GCB BTF duties.

1.3.1.2 Phenomena in GCB

During T100a or T100s current interruptions, an arc spans between the arcing contacts and generates a high-temperature low-density gas (hot gas). The hot gas remains in the space between the arcing contacts even after the current zero time. Moreover, when the hot gas is exhausted from the arcing space, it spreads to other spaces that are situated between high-voltage parts and the enclosing GCB tank wall. The hot gas might cause a dielectric breakdown in the arcing space and the high-voltage areas because of the low dielectric strength of the hot gas, as described below.

In general, the GCB performance is determined by the dielectric characteristics of the SF_6 gas whether or not a dielectric breakdown occurs. Figure 1.7 shows the critical electric field strength E per unit gas number density N for a dielectric break down in SF_6 as a function of gas temperature [2]. When the gas temperature is less than 1500 K, a dielectric breakdown cannot occur for E/N less than $350 \times 10^{-17}\ \mathrm{V \cdot cm^{-2}}$ ($3.5 \times 10^{-19}\ \mathrm{V \cdot m^{-2}}$). When the gas temperature exceeds almost 2500 K, for example, the critical value of E/N drops to $50 \times 10^{-17}\ \mathrm{V \cdot cm^{-2}}$ ($5 \times 10^{-20}\ \mathrm{V \cdot m^{-2}}$), which is only one seventh of the normal value. Therefore, the risk of a dielectric breakdown is much higher in a higher-temperature gas.

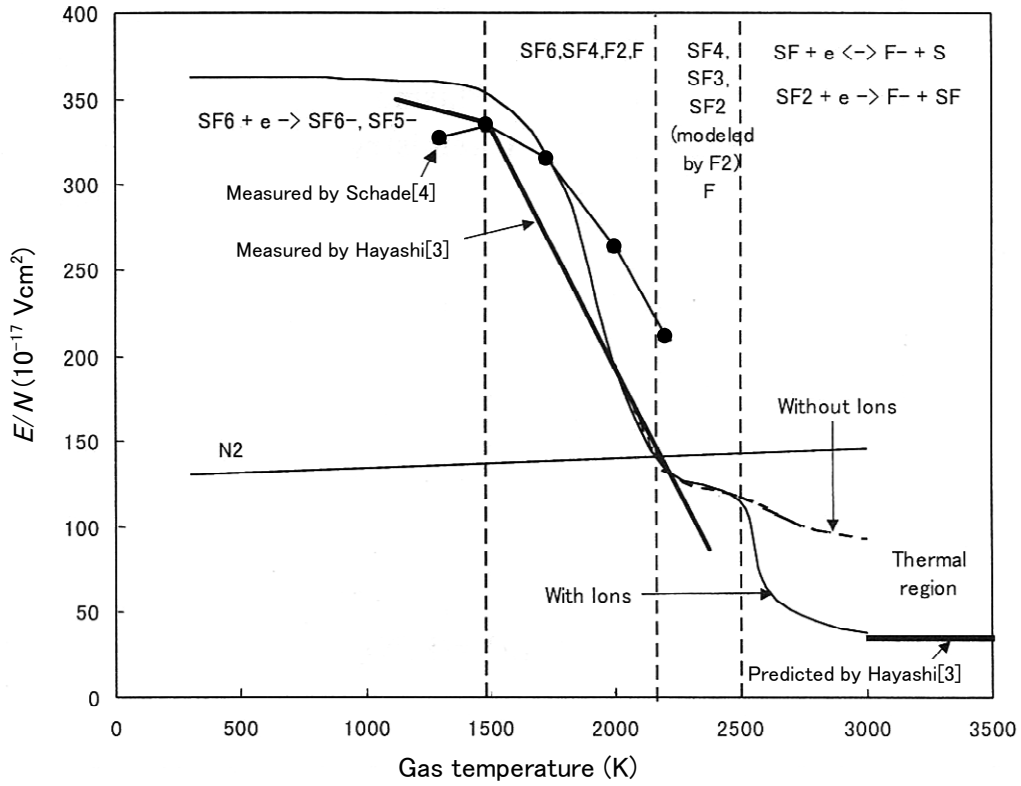

Figure 1.7 Dielectric strength of SF_6 gas against temperature [2]

1.3.1.3 Problems and associated countermeasures

The hot gas should be sufficiently cooled at the current zero time to lower the gas temperature in the arcing space, and the hot gas exhausted to the space between the high-voltage parts and the enclosing dead tank should be cooled as well. To cool the gas in the arcing space, the gas should flow laminarly and have no irregular stagnation or vortices. Therefore, the form of the gas-flow path should be carefully designed with this in mind, which is why gas-flow simulations have been developed and adopted.

Another issue involves the puffer chamber pressure. In general, a higher puffer chamber pressure blows out the hot gas more effectively. One way to achieve higher puffer pressure is to increase the size of the puffer piston. However, one must not forget that the repulsive force on the puffer-piston that resists opening increases in proportion to the piston's cross-sectional

area. If this repulsive force is too large, the velocity with which the contacts open decreases or even reverses, and such travel characteristics may degrade the interruption performance. In general, when a GCB interrupts a T100a or T100s current, the pressure in the puffer chamber attains its maximum value, so the movable parts of the GCB move slower or even reverse their direction because of the repulsive forces. Therefore, it is necessary to consider the travel characteristics of the movable parts for duties involving T100a or T100s currents.

The T100a and T100s test items also represent the most severe tests for the dielectric insulation between high-voltage parts and the grounded enclosure, because the arc generates a large amount of a hot low-density gas. To avoid a dielectric breakdown in GCBs, an exhaust path should be designed to cool the hot gas and reduce the electric field strength [5].

1.3.2 SLF interruption

1.3.2.1 Phenomena in power-system

The interruption duty for an SLF corresponds to that for a grounding fault that occurs several kilometres from the GCB on the load-side line, as shown in Fig. 1.8. Because of line impedance, the fault current is smaller than that for a BTF. However, the voltage is distributed over the power line between the GCB and the fault point when the current is interrupted. Since this voltage distribution is not influenced by the source-side voltage after the current is interrupted, the voltage travelling wave travels over the line to the right and left

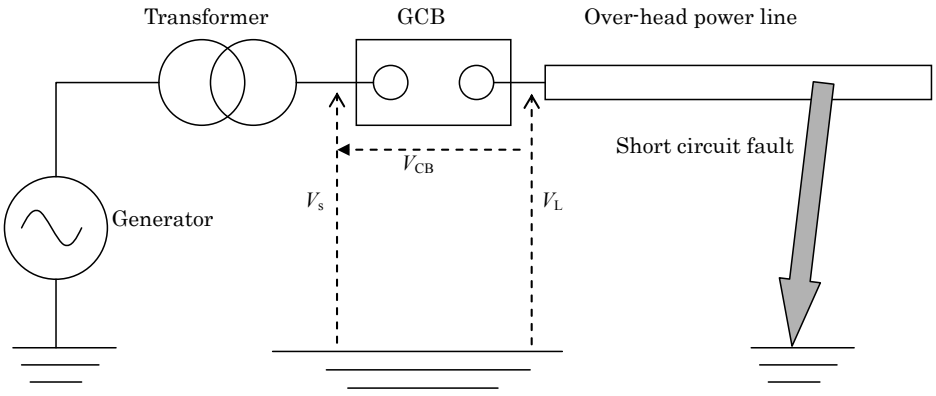

Figure 1.8 Schematic circuit of SLF

sides with each half value of the initial voltage distribution. The voltage travelling wave reflects from the breaker terminal and from the fault point on the power line. Thus, at the breaker terminal, the voltage waveform consists of a triangular oscillation with a fast rise time, as shown in Fig. 1.9.

Starting at the current zero time, the recovery voltage starts to rise steeply with basically no time delay. However, if capacitive components are present, the rise in the recovery voltage experiences a time delay. Therefore, because of the capacitance of GISs, GCBs for GISs are allowed 0.5 μs delays following the current zero time in interruption tests. As an example, the standard values specified by IEC [1] are 32 kV for u_L and 3.56 μs for t_L for 245-kV 50-kA 50-Hz GCBs. Therefore, the rate of rise of the recovery voltage (rrrv), u_L/t_L for 245-kV 50-kA 50-Hz is 9.0 kV/μs which, for instance, is much higher than that for T100s, which is u_1/t_1 = 2.0 kV/μs.

1.3.2.2 Phenomena in GCB

For SLF interruption, the recovery voltage rises immediately after the current zero time with a high rrrv, whereas the recovery voltage for BTF interruption rises with a time delay and a low rrrv. Therefore, for SLF fault conditions, when the voltage is applied between contacts, the hot gas in the arcing area may conduct electricity, which is enough to cause a post-arc current flow. This post-arc current generates Joule heat as determined by the current and resistance of the hot gas and thus heats the arcing area. However, the arcing area is cooled by convection to the surrounding gas whose temperature is low. Consequently, successful interruption can be achieved only when the cooling effect is larger than the heating effect.

1.3.2.3 Problems and associated countermeasures

It is generally accepted that the gas pressure in the puffer chamber is one of the significant factors affecting the interruption performance for SLFs. The following relationship is well known [6]-[8]:

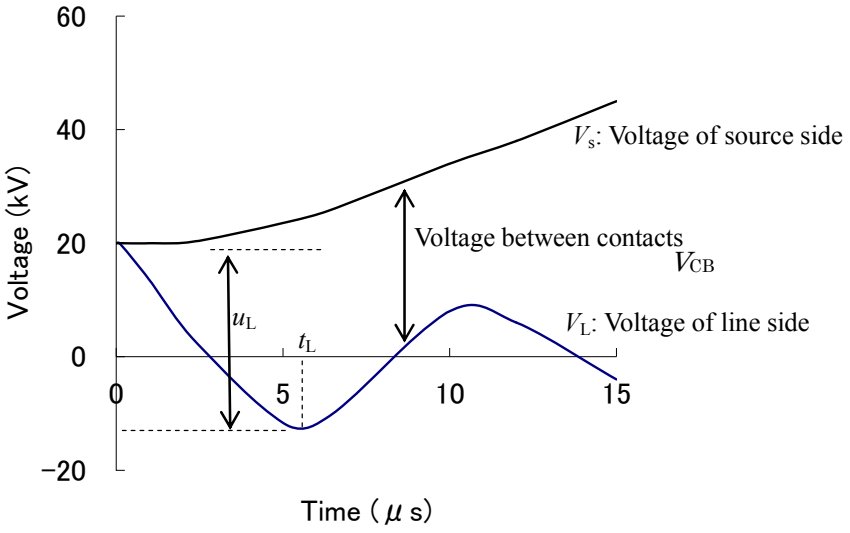

(a) Voltage of source and line side terminals of a circuit breaker

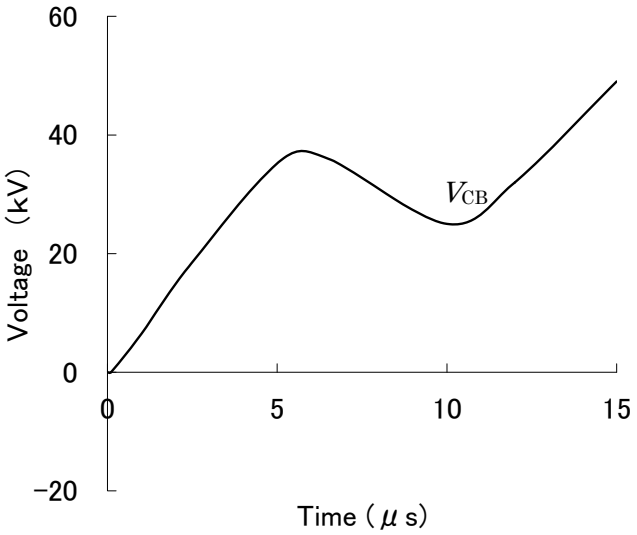

(b) Voltage between circuit breaker terminals

Figure 1.9 Schematic waveform of initial TRV of SLF

$$K \cdot {P_{\min}}^{\alpha} = \frac{\mathrm{d}u}{\mathrm{d}t} \cdot \left(\frac{\mathrm{d}i}{\mathrm{d}t} \right)^{\beta} \tag{1.1}$$

where u is the recovery voltage, i is the current, $P_{\min}$ is the minimum pressure needed in the puffer chamber at current zero time to successfully clear the SLF, K is a constant shape factor that includes the effects of each chamber configuration, and α and β are constants. One approach to improve the SLF interruption ability is to raise the puffer chamber pressure above $P_{\min}$.

The rrrv can be reduced by inserting a capacitive component in the line side or between the contacts. This would cause the factor du/dt in Eq. (1.1) to decrease so that K or $P_{\min}$ could be reduced. As a countermeasure to clear SLFs, some GCBs have capacitance between the contacts or between lines and ground.

1.3.3 Small capacitive current interruption

1.3.3.1 Phenomena in power-system

Interrupting small capacitive currents corresponds to interrupting no-load transmission lines or capacitor banks, as shown in Fig. 1.10. The current to be interrupted is only several tens or hundreds of amperes, which can be easily interrupted even, for instance, at 1 ms after

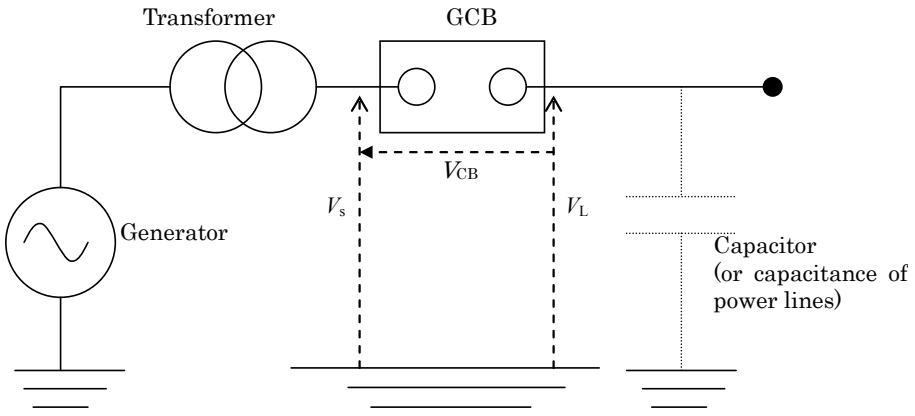

Figure 1.10 Schematic circuit of capacitive current interruption

contact separation. As shown in Fig. 1.11, the DC voltage after current interruption may remain on the load side, whereas the source side experiences an AC voltage. This results in a high voltage corresponding to twice the AC voltage being applied between the contacts.

This applied voltage can become larger than the source voltage because of the Ferranti

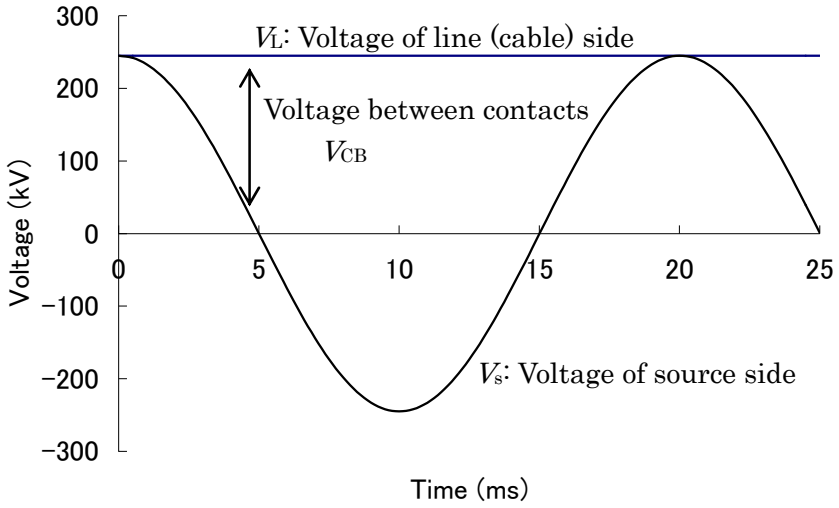

(a) Voltage of source and line side terminals of a circuit breaker

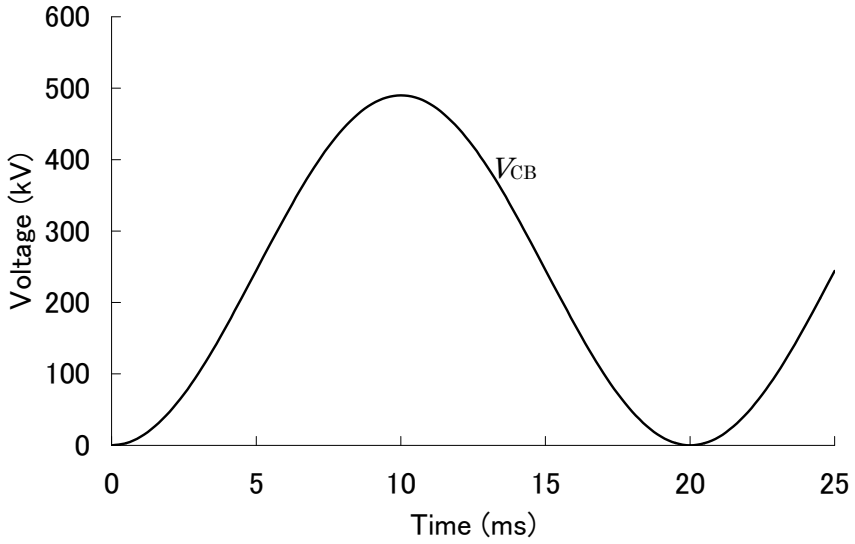

(b) Voltage between circuit breaker terminals

Figure 1.11 Schematic waveform of recovery voltage after capacitive current interruption

effect, and the multiplicative factor k that gives the recovery voltage needed to counter this AC voltage is called the voltage factor. A voltage factor of k = 1.4 is sometimes required for 245-kV GCBs, which means that the peak recovery voltage after small capacitive current interruption is 560 kV [1].

1.3.3.2 Phenomena in GCB

Successful small capacitive current interruption can be achieved at a smaller contact separation than for BTFs or SLFs, and then, the high recovery voltage discussed above may be applied between the minimally separated contacts. Therefore, the electric field at the contact surfaces rises to a high level and, in severe cases, results in a dielectric breakdown. During small capacitive current interruptions, the gas temperature between contacts can remains almost 300 K, so the breakdown characteristics are determined by the electric field and the gas density.

1.3.3.3 Problems and associated countermeasures

To improve capacitive current interruption, it is necessary to increase the dielectric strength between the contacts. One method to raise the dielectric strength is to increase the opening speed, which reduces the electric field. In the design of many GCBs, the conta-opening speeds are determined by this rationale.

Another approach to improve capacitive current interruption is to reduce gas-pressure friction within areas of high electric field. When the GCB opens, the gas pressure in the puffer chamber rises, and the compressed gas flows downstream where the arcing contacts are installed and a nozzle forms a flow channel. Fig. 1.12 schematically shows the pressure distribution along a throated gas-flow channel. When the inlet gas pressure p_{i} is not significantly higher than the outlet gas pressure p_{o}, the gas-flow speed is generally subsonic, and a minimum pressure appears at the throat. When the inlet gas pressure p_{i}' is much higher than the outlet gas pressure p_{o}', the gas-flow becomes supersonic, and the gas pressure between throat and outlet decreases below the value at the nozzle throat. The gas pressure can

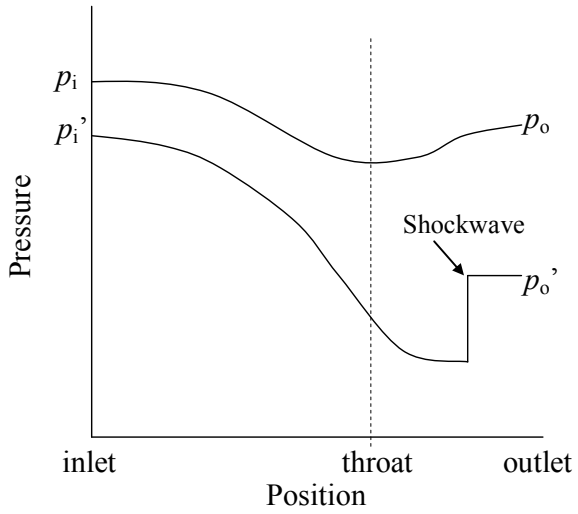

Figure 1.12 Schematic graph of pressure along gas-flow in channel with a throat

change abruptly, such as for a shockwave, as shown in Fig. 1.12 [9]. When the pressure in the puffer chamber exceeds a certain value, the gas-flow speed becomes supersonic, and the gas pressure in the area between the arcing contacts can decrease [10][11], which may result in low dielectric strength. Therefore, pressure friction should be avoided by a using a nozzle of proper shape.

1.4 Hybrid-puffer^{TM}-type chamber

The 1980s saw an expansion in the demand for electric power, so utilities needed high-voltage and larger-capacity GCBs such as 300-kV 63-kA or 550-kV 63-kA. Manufacturers, in turn, made efforts to release compact-sized GCBs. To develop higher-voltage and larger-capacity GCBs, the strong gas-flow needed to overcome the problems described above can be obtained if the puffer chamber is made larger. However, making the puffer chamber larger may result in GCBs becoming undesirably large. Moreover, a large puffer chamber generates large repulsive force, which requires more operating energy. This means that GCBs require larger operating mechanisms and a higher mechanical strength, which might cause larger

oscillations or operation noise as well as higher costs. Therefore, the demand for compact-sized, high-voltage, and large-capacity GCBs that require low operating energy increased. It was in this setting that the Hybrid-puffer^{TM}-type chamber [12] was invented.

Figure 1.2 shows a schematic of the interruption chamber. In the closed position, the puffer chamber and the internal area of the operational rod are connected through holes in the wall of the operational rod. At the beginning of interruption, the hot gas generated by the arc flows into the puffer chamber through these holes, which increases the pressure in the puffer chamber. In the last step of the interruption process, these holes no longer connect with the puffer chamber, so the gas in the puffer chamber is simply compressed by the mechanical piston and the gas pressure continues to rise. This scheme was adopted for 72/84-kV GCB chambers in 1980 [12] and for 550-kV GCB chambers in 1992 [10].

1.5 Rotary-arc-type chamber

From the viewpoint of mechanical requirement, the best solution for the interruption chambers is a self-blast-type chamber, which does not need to mechanically compress the gas. If further reductions in operating energy or cost are required, a self-blast-type chamber should be developed. Kittaka et al. [13] and Barrault et al. [14] reported a self-blast-type chamber for a 72-kV GCB. They adopted a mechanism consisting of rotary-arcs driven into the self-blast-type chamber by electromagnetic forces. This GCB achieves the highest voltage rating of all self-blast-type chambers developed thus far. Young et al. [15] have made an effort to develop a 145-kV GCB that has a small puffer chamber and an arc-rotating mechanism.

In the rotary-arc-type GCB chamber, more complex phenomena occur than in puffer-type GCBs. In particular, the motion of the arcs themselves is unique among GCBs. Rotary-arcs in switching devices have been observed by several researchers, who have pointed out that the rotary-arcs may cause the efficient expansion of the hot gas, which may be cooled by the

surrounding gas because of the continuous motion of the arcs. Piotrowski et al. [16] suggested that the arc voltage of rotary-arcs in a narrow chamber might relate to the arc lengths. Ennis [17] made experimental studies of rotary-arcs and found 'pumping effects' in which rotary-arcs generate gas motion not only by expanding hot thermal gas but also by pumping up gases due to the rotation of spiral arcs, which might contribute to the cooling effects of arcs. Kweon et al. have evaluated influence of swirling flow by the arc rotation by gas-flow simulation [18], and investigated 25.8-kV GCB with rotary arcs driven by permanent magnet [19]. Lee et al. [20] have investigated thermal expansion characteristics in a model GCB.

However, further studies are needed to understand the details of real-scale rotary-arc chambers for high voltage GCBs.

1.6 Simulation technologies used to develop GCB chambers

Procedures to develop GCBs include investigations of the specifications and configurations of the GCBs, manufacturing prototypes, performing dielectric tests, mechanical endurance tests, interruption tests, etc. If the results of the tests are not satisfactory, the prototype chamber can be improved until the required performance is achieved. Because such procedures are time consuming and expensive, their repetitions should be minimised. Therefore, for successful tests or improvements, it is very important to understand and predict such GCB phenomena. Towards this end, many types of simulations have been employed in the development of GCB chambers, including electric field simulations, mechanical endurance simulations, oscillation simulations, simulations combining puffer chamber pressure and the travelling characteristics, hot-gas-flow simulations, calculations of thermodynamic and transport properties of the hot gas, etc. This thesis focuses in particular on the latter three simulations. History and recent trends are summarised in the next section.

1.6.1 Combined simulation of puffer-chamber pressure and travelling characteristics

The gas pressure generated in a puffer chamber is one of significant factors that determine the interruption performance, as explained in Section 1.4. When the gas pressure in a GCB puffer chamber rises, repulsive forces are generated because of the compressed gas in the puffer chamber, and they act in opposition to the desired motion of the operating mechanisms. These repulsive forces may reduce the operating speed, which also affects puffer pressure. Because the puffer pressure and the travelling speed affect each other in this way, they should be considered simultaneously. In such combined simulations, gas-flow phenomena, arcing phenomena, gas compression phenomena, and the dynamic characteristics of the operating mechanism should be taken into account. Practical methods for one-dimensional models have been developed by many industrial researchers [21]-[25].

1.6.2 Hot-gas-flow simulations

1.6.2.1 Trends in hot-gas-flow simulations for GCBs

If the hot gas generated by arcs remains between the arcing contacts, the restrike probability increases. Furthermore, if the hot gas spreads towards the enclosing dead-tank wall, the probability of grounding faults also rises. These phenomena cannot be evaluated by the one-dimensional simulation described above, so two-dimensional hot-gas simulations have been developed and adopted.

A hot-gas-flow simulation for GCBs requires the following features:

a. Compressive flow

   The gas-flow in a GCB is compressive, which is generally more complex and difficult to solve.

b. Subsonic and supersonic flows

   The GCB gas-flow speed can be subsonic or supersonic. The gas-flow speed may be subsonic or supersonic, depending on the application, and conventional gas-flow

simulation tools are designed to solve either phenomenon. In general, solving both of them is a difficult problem.

c. Transient phenomena

The phenomena in a GCB are transient and are, therefore, generally more complex and difficult to solve.

d. High temperature

The existence of arc plasmas causes the GCB gas temperature to rise as high as 10000 K, which is extremely high in comparison with other applications. Therefore, many phenomena are very complex and difficult to simulate correctly. Furthermore, it is difficult to compare simulation results with real phenomena (to improve the accuracy of the simulation) because it is very difficult to measure or observe these phenomena because of the high-temperature atmosphere in which they occur.

e. Chemical reaction

Because of the arc plasma and high gas temperature, chemical reactions should be considered. For example, a gas molecule may decompose or get ionised, and the gas constant and other characteristics may change.

f. Moving parts or boundaries

The GCB has moving parts (e.g. the nozzle), and these are important for gas-flow.

g. Obstruction and branch

The gas flows from a puffer chamber through a channel between the nozzle and the movable arcing contact, as shown in Fig. 1.1. After reaching the arcing space, the gas flows towards both the stationary arcing contact and the movable arcing contact. The stationary arcing contact is at the centre of the gas-flow channel, where it obstructs the gas-flow. Furthermore, the branches in the gas-flow channel and the existence of an obstruction make the calculation difficult.

Some researchers have developed hot-gas-flow simulations for GCBs. For example,

Okamoto et al. [26] developed a program to simulate hot gas-flow that uses the modified fluid-in-cell (FLIC) method, which is a type of finite differential method. The modified FLIC method features triangular cells that make it possible to easily trace complex configurations [27], while the FLIC originally has square cells. They developed a function to describe moving parts, and the stationary parts were moved virtually to simplify the program. The researchers also enabled the FLIC-based simulation to consider compressing the puffer chamber and arcs. In and around the arcs, SF_6 gas decomposes and its characteristic becomes very different from an ideal gas. Therefore, the researchers introduced the thermodynamic and transport characteristics of SF_6 gas at atmospheric pressure that was based on the literature [28]. Kim et al. [29] as used finite volume fluid in cell method based on Navies-Stokes equations.

Trépanier et al. [30]-[32] have adopted an adaptive cell algorithm that automatically generates cells that adapt to the motion of movable parts or to the gas-flow. The algorithm can calculate sharp and large fluctuations of the flow, such as shock waves, without requiring too many cells. Robin-Jouan et al. has used Trépanier's program to develop GCBs [33].

In addition to being specialised for the GCB phenomena described above, versatility and user friendliness are also important as in engineering tools. The software should therefore satisfy the following requirements:

a. allow rapid cell creation,

b. execute rapidly,

c. be compatible with conventional computers with reasonable costs and not require special systems such as supercomputers.

For example, to simulate gas-flow in a GCB chamber, Yan et al. [34] modified the versatile flow simulation software 'Phoenics' [35], which is available as a commercial computational fluid dynamics (CFD) program.

In other trend of hot gas-flow simulation, Kweon et al.[19][36] has been considered

contamination of PTFE into the arc and gas-flow, and Lindmayer [37] has performed three-dimensional simulation for low-voltage breakers.

1.6.2.2 Modified FLIC method

The modified FLIC method is used to study hot gas-flow in GCBs, and in this thesis, it is improved to allow the simulation of new types of GCBs. An outline of the modified FLIC method is presented in this section.

A. Fundamental equations

Continuity equations, momentum equations for the axial and radial directions, and energy-conservation equations are described as follows:

1) Continuity equations

$$\frac{\partial \rho}{\partial t}+\frac{\partial}{\partial z}\left(\rho v_{\mathrm{z}}\right)+\frac{1}{r}\frac{\partial}{\partial r}\left(r\rho v_{\mathrm{r}}\right)=0\,, \tag{1.2}$$

$$\frac{\partial \rho_{\mathrm{p}}}{\partial t}+\frac{\partial}{\partial z}\left(\rho_{\mathrm{p}} v_{\mathrm{z}}\right)+\frac{1}{r}\frac{\partial}{\partial r}\left(r\rho_{\mathrm{p}} v_{\mathrm{r}}\right)=0\,, \tag{1.3}$$

$$\frac{\partial \rho_{\mathrm{c}}}{\partial t}+\frac{\partial}{\partial z}\left(\rho_{\mathrm{c}} v_{\mathrm{z}}\right)+\frac{1}{r}\frac{\partial}{\partial r}\left(r\rho_{\mathrm{c}} v_{\mathrm{r}}\right)=0\,, \tag{1.4}$$

2) Momentum equation for axial direction

$$\frac{\partial}{\partial t}\left(\rho v_{\mathrm{z}}\right)+\frac{\partial}{\partial z}\left(\rho v_{\mathrm{z}} v_{\mathrm{z}}\right)+\frac{1}{r}\frac{\partial}{\partial r}\left(r\rho v_{\mathrm{z}} v_{\mathrm{r}}\right)=-\frac{\partial p}{\partial z}\,, \tag{1.5}$$

3) Momentum equation for radial direction

$$\frac{\partial}{\partial t}\left(\rho v_{\mathrm{r}}\right)+\frac{\partial}{\partial z}\left(\rho v_{\mathrm{r}} v_{\mathrm{z}}\right)+\frac{1}{r}\frac{\partial}{\partial r}\left(r\rho v_{\mathrm{r}} v_{\mathrm{r}}\right)=-\frac{\partial p}{\partial r}\,, \tag{1.6}$$

4) Energy-conservation equations

$$\frac{\partial}{\partial t}(\rho e_{\mathrm{n}})+\frac{\partial}{\partial z}(\rho e_{\mathrm{n}} v_{\mathrm{z}})+\frac{1}{r}\frac{\partial}{\partial r}(r\rho e_{\mathrm{n}} v_{\mathrm{r}}) = -\frac{\partial}{\partial z}(pv_{\mathrm{z}})-\frac{1}{r}\frac{\partial}{\partial r}(rpv_{\mathrm{r}})-\kappa\frac{\partial}{\partial z}\left(\frac{\partial T}{\partial z}\right)-\kappa\frac{1}{r}\frac{\partial}{\partial r}\left(r\frac{\partial T}{\partial r}\right) + e_{\mathrm{arc}}-e_{\mathrm{rad}}-\rho_{\mathrm{p}}e_{\mathrm{pab}}-\rho_{\mathrm{c}}e_{\mathrm{cab}}, \tag{1.7}$$

$$e_{\mathrm{n}}=\frac{p}{(\gamma-1)\rho}+\frac{1}{2}\left(v_{\mathrm{z}}{}^{2}+v_{\mathrm{r}}{}^{2}\right), \tag{1.8}$$

where e_{n} is the energy per unit mass, e_{pab} is the ablation energy of PTFE per unit mass and per unit time, e_{cab} is the ablation energy of copper per unit mass and per unit time, p is the pressure, e_{arc} is the input thermal energy in an arc column per unit volume, e_{rad} is thermal radiation from an arc, r is the radial coordinate, T is temperature, t is time, v_z is the axial velocity in the z direction, v_r is the radial velocity, z is the axial coordinate, γ is the specific heat, κ is thermal conductivity, and ρ, ρ_{p}, and ρ_{c} are the densities of the mixture of SF_6 gas, PTFE vapour, and copper vapour, only PTFE vapour, and only copper vapour, respectively.

Equation (1.2) represents the mass balance of the gas mixture containing SF_6, PTFE, and copper. Similarly, Eqs. (1.3) and (1.4) represent the mass balances of PTFE and copper, respectively.

B. Modelling the arcs

The quantity e_{arc} in Eq. (1.7) is given by Eq. (1.9) as the Joule heat:

$$e_{\mathrm{arc}}=\frac{i^{2}\ell\dfrac{\sigma}{S_{\mathrm{a}}}}{S_{\mathrm{a}}\ell}=\sigma\left(\frac{i}{S_{\mathrm{a}}}\right)^{2}, \tag{1.9}$$

where i is the arc current, ℓ is the arc length, S_{a} is the cross-sectional area of the arc column, and σ is the electrical conductivity as function of pressure and temperature of the cell.

Considering an arc as a grey body, the thermal radiation e_{rad} of the arc is given by

$$e_{\mathrm{rad}} = \varepsilon\ \sigma_{\mathrm{s}}\ (T_{\mathrm{arc}}{}^{4} - T_{\mathrm{amb}}{}^{4})\ S_{\mathrm{f}}\,, \tag{1.10}$$

where T_{arc} is the arc temperature, T_{amb} is the temperature of the surrounding area, S_{f} is the surface area of the contact, ε is radiation ratio, and σ_{s} is the Stephan-Boltzmann constant (=5.6687 × 10^{-8} W·m^{-2}·K^{-4}). The quantity T_{amb} is the temperature of the nozzle-wall surface because the arc burns within a nozzle.

The electrode and nozzle materials (copper and PTFE, respectively) are vaporised and sublimated by the arc, cooling the arc in the process. This cooling effect is also considered in our simulations. Moreover, arc energy is consumed by the dissociation of PTFE. Table 1.2 shows the magnitudes of ablation energies. The total amount of ablated materials is estimated from the experimental results [36].

1.6.3 Calculation of thermodynamic and transport properties of SF_6 gas

1.6.3.1 Trends in studies on thermodynamic and transport properties

Since SF_6 gas was adopted for use in GCBs or switchgears, the fundamental characteristics of the SF_6 gas have been studied. One study focused on the thermodynamic and transport properties at high temperatures, which corresponds to the gas that surrounds the arcs. Frost et al. [28] determined the gas constant, specific heat, thermal conductivity, and electrical conductivity of SF_6 gas up to 30000 K at 1.57 MPa (16 atm in the literature). These properties have been employed in hot-gas-flow simulations, as described in Section 1.5.2. Sakuta et al. [37] calculated these same properties of a mixture of PTFE, which is the primary material for the nozzle, and for a mixture of copper, which is the primary electrode material.

Table 1.2 Ablation energies of PTFE and copper

	Evaporation temperature (K)	Evaporation energy (J/kg)	Dissociation temperature (K)	Dissociation energy (J/kg)
PTFE	600	5.73×10^{4}	3400	1.19×10^{7}
Copper	1360	4.80×10^{6}	N/A	N/A

For conventional puffer-type GCBs, data up to 1.57 MPa suffice because the pressure in the chamber does not exceed this value. Furthermore, the error seems to be insignificant even if the pressure exceeds 1.57 MPa because the main process is mechanical compression rather than the hot-gas effect.

1.6.3.2 Method of calculating thermodynamic and transport properties

In this section, a method to calculate the thermodynamic and transport properties of pure SF_6 gas is explained briefly. Details can be found in the literatures [38][39].

Twenty-three kinds of particle were considered in the calculation, as follows.

molecules : SF_6, SF_5, SF_4, SF_3, SF_2, SF, SSF_2, FSSF, F_2, S_2

atoms : F, S

ions : F^-, F^+, S^+, F^{2+}, S^{2+}, S^-, S_2^+, F_2^+, SF^+, SF^-

electrons : e^-

The basic equations that relate the dissociation and ionisation reactions between these particles are solved by the Newton-Raphson method, which gives the thermal equilibrium compositions of high-temperature SF_6 gas. By using the results of the gas composition, the thermodynamic properties of high-temperature SF_6 gas that contains a mixture of related molecules, atoms, ions, and electrons are obtained.

1) Gas constant R

By using the mass density ρ, the gas constant R is defined as

$$R = \frac{p}{\rho T}, \tag{1.11}$$

where the mass density ρ can be calculated using

$$\rho = \sum_{i=1}^{N} m_i n_i, \tag{1.12}$$

where m_i is the mass of particle i, n_i is the number density of particle i, and N is the number of specimens considered in the calculations.

2) Enthalpy h

The enthalpy h is obtained using

$$h = \frac{1}{\rho}\sum_{i=1}^{N} h_i m_i n_i , \tag{1.13}$$

where h_i is the enthalpy of particle i and can be obtained using

$$h_i = \frac{1}{m_i}\left(\frac{5}{2}k_{\mathrm{B}}T + k_{\mathrm{B}}T^2\frac{\partial}{\partial T}\left(\ln Z_i\right) + \Delta_f H_i^0\right). \tag{1.14}$$

Here, k_B is the Boltzmann constant and Z_i is internal partition function of particle i. In Eq. (1.14), $\Delta_f H_i^0$ is the standard enthalpy of formation, which is the reaction heat produced by the composition elements at a standard state of 0 K and 0.1 MPa.

3) Specific heat γ

To obtain the specific heat γ, the isopiestic specific heat C_{p} is required:

$$C_{\mathrm{p}} = \left.\frac{\partial h}{\partial T}\right|_{p=const} . \tag{1.15}$$

The following relationship relates the isopiestic specific heat C_{p} to the isovolumic specific heat C_{v}, R and the specific heat γ, which enables us to obtain γ as

$$\gamma = \frac{C_{\mathrm{p}}}{C_{\mathrm{v}}} = \frac{C_{\mathrm{p}}}{C_{\mathrm{p}} - R} . \tag{1.16}$$

The transport properties are calculated using the formulas given by Yos, which are based on the first Chapman-Enskog approximation [40].

4) Electrical conductivity σ

The electrical conductivity σ is calculated using Eqs. (1.17) and (1.18):

$$\sigma = \frac{e^2}{k_B T} \frac{n_e}{\sum_{\substack{j=1 \\ j \neq e}}^{N} n_j \Delta_{ij}^{(1)}}, \tag{1.17}$$

$$\Delta_{ij}^{(1)} = \frac{8}{3} \left(\frac{2 m_i m_j}{\pi k_B T (m_i + m_j)} \right)^{\frac{1}{2}} \pi \overline{\Omega_{ij}^{(1,1)}}, \tag{1.18}$$

where $\pi \overline{\Omega_{ij}^{(1,1)}}$ is the momentum-transfer collision integral.

5) Thermal conductivity κ

The thermal conductivity κ is calculated using the following equations:

$$\kappa = \kappa_{tr} + \kappa_{int} + \kappa_{re}, \tag{1.19}$$

$$\kappa_{tr} = \frac{15}{4} k_B \sum_{i=1}^{N} \frac{n_i}{\sum_{j=1}^{N} \alpha_{ij} n_i \Delta_{ij}^{(2)}}, \tag{1.20}$$

$$\alpha_{ij} = 1 + \frac{\left(1 - \frac{m_i}{m_j}\right)\left(0.45 - 2.54 \frac{m_i}{m_j}\right)}{\left(1 + \frac{m_i}{m_j}\right)^2}, \tag{1.21}$$

$$\Delta_{ij}^{(2)} = \frac{16}{5} \left(\frac{2 m_i m_j}{\pi k_B T (m_i + m_j)} \right)^{\frac{1}{2}} \pi \overline{\Omega_{ij}^{(2,2)}}, \tag{1.22}$$

$$\kappa_{int} = k_B \sum_{i=1}^{N} \frac{\left(\frac{C_{pi} M_i}{R_{un}} - \frac{5}{2} \right) n_i}{\sum_{j=1}^{N} n_j \Delta_{ij}^{(1)}}, \tag{1.23}$$

$$\kappa_{\mathrm{re}} = k_{\mathrm{B}} \sum_{\ell=1}^{N_r} \frac{\left(\dfrac{\Delta H_\ell}{RT} \right)^2}{\displaystyle\sum_{i=1}^{N} \frac{\beta_{\ell i}}{n_i} \left\{ \sum_{j=1}^{N} (\beta_{\ell i} n_j - \beta_{\ell j} n_i) \Delta_{ij}^{(1)} \right\}}, \tag{1.24}$$

where $\pi\overline{\Omega_{ij}^{(2,2)}}$ is the viscosity collision integral, M_i is the molecular mass of particle i, R_{un} is the universal gas constant (=8.31 J·mol^{-1}·K^{-1}), N_r is the number of chemical reactions, and $\beta_{\ell i}$ is the stoichiometric coefficient for the ℓth chemical reaction of particle i. The quantity ΔH_ℓ is the reaction heat per mol calculated using

$$\Delta H_\ell = \sum_{i=1}^{N} \beta_{\ell i} h_i M_i . \tag{1.25}$$

1.7 Purpose and composition of the thesis

For this study, four types of chambers were studied and developed. One is the Hybrid-puffer$^{\mathrm{TM}}$-type chamber for 300-kV 63-kA GCBs, for which the development process is summarised in Chapter 2. The advanced Hybrid-puffer$^{\mathrm{TM}}$-type chamber for 245-kV 50-kA GCBs, which requires a low operating-energy, was developed after completion of the former Hybrid-puffer$^{\mathrm{TM}}$-type chamber series, and the basic investigations and improvements resulting from gas-flow simulations are described in Chapters 3 and 4. Because of the demands for further low operating-energy and low-cost GCBs, the development of the tandem-puffer-type chamber for 245-kV GCBs has begun, and further details of the analysis of hot gas-flow was required, as is discussed in Chapter 5. In addition to developing the tandem-puffer-type chamber, a basic study has begun on self-blast-type chambers. One of the ideas to improve the performance of these chambers is to make the arc move, which may produce a significant pressure increase in the thermal chambers and may cool the arc itself by moving in the gas-flow. Chapter 6 investigates basic phenomena in long-gap rotary-arcs with

the aim of adapting these to high-voltage GCBs.

The contents of each chapter are summarised below.

In Chapter 2, the development of a new 300-kV 63-kA GCB is described. Research to adapt the Hybrid-puffer^{TM}-type interruption chamber to 300-kV GCBs was performed for the first time. To improve the interruption ability, an inner-nozzle was also introduced. The high-pressure gas compressed in the puffer chamber blasts the arcing area and flows out in two directions: towards a stationary arcing contact and towards a movable arcing contact. In the puffer-type GCB, the puffer cylinder moves together with the movable arcing contact so that the exit of the blasting gas from the puffer chamber is always located at the front of the movable arcing contact. Therefore, the length of the arc to be cooled by the gas flowing towards the movable arcing contact is short, whereas the length of the arc to be cooled by the gas flowing towards the stationary arcing contact is long. To increase the length of the arc at the movable arcing contact, the inner-nozzle was proposed to be installed near the puffer chamber gas-flow exit. For no-load operations, results of pressure measurements at the chamber show that adapting the inner-nozzle may reduce the pressure fluctuations, which is expected to improve small capacitive-current interruption performance. The behaviour of the hot gas in the GCB tank was also investigated by measurements and calculations. As a result, interruption tests for the new 300-kV 63-kA GCB were successfully completed.

In Chapter 3, the process of choosing the type of interruption chamber for a new 245-kV 50-kA GCB via simulations is described. The GCB to be developed adopts a hydraulic operating mechanism that requires 1.5 kJ, which is a third of the conventional energy requirements. Two types of chambers were compared for the new GCB. One is called the 1vol-1pis (one volume, one piston) type and the second is the 2vol-2pis (two volumes, two pistons) type. The principle of the 1vol-1pis-type is the same as for the Hybrid-puffer^{TM}-type, but the cross-sectional area of the puffer piston was reduced. The 2vol-2pis-type has two chambers, which are a thermal-puffer chamber that raises the gas pressure by taking the hot

gas from arcs and a mechanical-puffer chamber that raises the gas pressure by mechanically compressing the gas. For both types of chambers, a one-dimensional simulation simultaneously dealing with the pressure rise in the puffer chambers and the operational characteristics was performed. The results of the simulations indicate that both chambers should have sufficient interruption capacities when used with an operating energy of 1.5 kJ, so the 1vol-1pis-type chamber called the advanced Hybrid-puffer^{TM}-type chamber were selected for development.

In Chapter 4, improvements in the two-dimensional hot-gas-flow simulation program are described, which were undertaken to develop the advanced Hybrid-puffer^{TM}-type chamber. It is found that conventional simulation program (the modified FLIC) used in Chapter 2 gives puffer chamber pressures that exceed the values found experimentally when it is used to simulate the advanced Hybrid-puffer^{TM}-type chamber. To clear up the problem, the thermodynamic and transport properties of SF_6 gas are obtained for higher pressures and temperatures, and these are introduced to the FLIC model. With this approach, the simulation yields the proper pressure values for the puffer chamber. Furthermore, we find that the proper pressure in the puffer chamber may be obtained by making movable parts move rather than making stationary parts move virtually, as in the conventional method.

In Chapter 5, the modified FLIC method is modified to simulate tandem-puffer-type chambers, which has a thermal- and mechanical-puffer in series. For developing these chambers, we find that the hot-gas-flow simulation program developed in Chapter 4 gives the pressure values in the puffer chambers that are consistently lower than the experimental data. To resolve this problem, we introduce the thermodynamic and transport properties of SF_6 gas mixed with PTFE. Furthermore, we also consider changing the arc diameter. These improvements are confirmed to be important factors for obtaining good agreement with experimental data.

In Chapter 6, behaviour of the rotary-arcs is experimentally investigated. The rotary-arcs

are ignited within the PTFE sleeve to observe the interaction between these arcs and PTFE. Measurements of the arc voltage, photographs of the arc shape, and the measurement of the dielectric break-down voltage of the hot gas near the chamber are performed for various arc-chamber geometries. In particular, we concentrated on observing the extensional arc voltage before the current zero time. The extensional arc voltage is one of the factors that indicate the interruption ability. The results show that the extensional arc voltage may affect the arc rotation. The arc rotation results in a longer arc, and the extensional arc voltage increases with arc voltage. The dielectric strength near the rotary-arcs was measured and it is found that the rotation of the arc results in a decrease in the dielectric strength. Both the extensional voltage and the dielectric strength are related to the magnetic field, arc current, and PTFE sleeve diameter, which might constrain the arc length.

Finally, the thesis is summarised in Chapter 7.

References

[1] IEC International Standard 62271-100

[2] G. J. Cliteur, Y. Hayashi, E. Haginomori and K. Suzuki: "Calculation of the uniform breakdown field strength of SF_6", *IEEE Trans. on Dielect. Elect. Insul.*, Vol.5, No.6, pp.843-849, 1998

[3] Y. Hayashi, M. Ishikawa, K. Suzuki, and H. Ikeda: "Investigation of hot-gas flow in SF_6 gas circuit breakers", *Proceedings of 6th Annual Conference of the Power & Energy society IEEJ*, p.269, 1995

[4] E. Schade: "Recovery of switching arcs", *Proceedings of the 17th International Conference on Phenomena in Ionized Gases*, p.277, 1985

[5] H. Nishiyama, K. Hamada, T. Uchii, and Y. Tanaka: "Transient response simulation of downstream thermofluid field in a gas circuit breaker at current interruption", *Proceedings of 15th International Conference on Gas Discharges and their Applications*, Vol.I, pp.5-8, September 2004

[6] G. Find and J. A. Rich: "Recovery speed of axial flow gas blast interrupter, Dependence on pressure and di/dt for air and SF_6", *IEEE Trans. on Power Apparatus Society*, vol. 93, No.5, pp. 1675-1684, Jan. 1974.

[7] H. Nishikawa, A. Kobayashi, T. Okazaki, and S. Yanabu: "Arc extinction performance of SF_6 gas blast interrupter", *IEEE Trans. on Power Apparatus Society*, Vol. 95, No.6, pp. 1834-1844, Jan. 1976

[8] B. W. Swanson, R. M. Roadstnd, T. E. Brounce: "Arc cooling and short line fault interruption", *IEEE Trans. on Power Apparatus Society*, Vol. 90, No.3, pp. 1094-1102, Jan. 1971

[9] H. W. Liepmann and A. Roshko: ‘’Elements of gasdynamics’’, John Wiley & sons, Inc., 1956 (Translated into Japanese by K. Tamada, 1960)

[10] K. Suzuki, H. Toda, A. Aoyagi, H. Ikeda, A, Kobayashi, I. Ohshima, and S. Yanabu: “Developing of 550 kV 1-break GCB (Part I). -Investigation of interrupting chamber performance-”, *IEEE Trans. on Power Delivery*, Vol. 8, No. 3, pp.1184-1191, July 1993

[11] F. Endo, M. Sato, M. Tsukushi, Y. Yoshioka, K. Saito, and K. Hirasawa: “Analytical prediction of transient breakdown characteristics of SF_6 gas circuit breakers”, *IEEE Trans. on Power Delivery*, Vol. 4, No.3, pp. 1731-1737, July. 1989

[12] S. Yanabu, H. Mizoguchi, H. Ikeda, K. Suzuki, and M. Toyoda: " Development of Novel Hybrid Puffer Interrupting Chamber for SF_6 Gas Circuit Breaker Utilizing Self-pressure-rise Phenomena by Arc ", *IEEE Trans. on Power Delivery,* Vol.4, No.1, 1989.

[13] Y. Kittaka: “Outline of XAE7-type 72/84 kV GIS for general consumers”, *Electrical Review*, pp. 32- 35, March 2004.

[14] M. Barrault, A. Girard, and O. Filleau: “The auto-expansion circuit-breaking principlent”, *CIGRE* SC-13-302, 1990

[15] K. A. Young and J. W. Spencer: “Optical diagnostics for studing a rotating arc in SF_6 gas”, *Proceedings of 14th International Conference on Gas Discharges and their Applications*, Vol.II, pp.353-356, September 2002

[16] J. B. Piotrowski and A. D. Wolny: “Longitudinal Magnetic Field Effect on Arc Voltage of Electric Arcs Confined in Organic Enclosures”, *Proceedings of 13th International Conference on Gas Discharge and their Applications*, Vol.I, pp.190-193, September 2000.

[17] M. G. Ennis: “Investigation of Fundamental Processes Affecting the Behaviour of Electric Arcs in Electromagnetic Interrupters”, Thesis for PhD. at the University of Liverpool, April 1996

[18] K. Y. Kweon, J. D. Yan, W. P. Song, and M. T.C. Fang: "Swirling flow and its influence on high current DC arcs", *Proceedings of 14th International Conference on Gas Discharges and their Applications*, Vol.I, pp.67-70, September 2002

[19] K. Y. Kweon, J. D. Yan, K. Y. Park, W. P. Song, and M. T. C. Fang: "A computational investigation into the high current arcing process of a 25.8 kV permanent magnet-assisted auto expansion interrupter", *Proceedings. of 15th International Conference on Gas Discharges and Their Applications*, pp. 37-40, Sep. 2004

[20] J. C. Lee, Y. G. Kim, S. W. Lee, and Y. J. Kim: "An investigation on flow characteristics of a thermal expansion circuit breaker near the current zero period", *Proceedings of 15th International Conference on Gas Discharges and their Applications*, Vol.I, pp.57-60, September 2004

[21] H. Mizoguchi and T. Iwamoto: "Calculation of blasted gas mass flow in puffer type gas circuit breaker", *Proceedings of Conference of IEEJ*, Vol. 11 No.740, 1971, (In Japanese)

[22] Y. Yoshioka, M. Chikushi, K. Natsui, and K. Hiarsawa: "Gas pressure at a puffer chamber of puffer type gas circuit breaker in current interruption and its calculation method", *IEEJ Transactions*, Vol. 98-B, No.12, pp.17-24, December 1978 (In Japanese)

[23] S. Yanabu, H. Mizoguchi, T. Iwamoto, Y. Ozaki, and Y. Murayama: "Mass flow analysis and opening characteristics in interruption of puffer type gas circuit breaker ", *IEEJ Transactions*, Vol. 99-B, No.6, pp.379-386, June 1979 (In Japanese)

[24] W. Hofbauer and J. Stechbarth: "Strategic tools-application for the development of a 300kV/50kA GIS self-blast circuit breaker", *CIGRE*, SC13-110, August 1994

[25] N. Osawa and Y. Yoshioka: "Investigation of the optimum design of thermal puffer type gas circuit breaker with secondary chamber", *Proceedings of 15th International Conference on Gas Discharges and their Applications*, Vol.I, pp.13-16, September 2004

[26] M. Okamoto, M. Ishikawa, K. Suzuki, and H. Ikeda: "Computer simulation of phenomena associated with hot gas in puffer-type gas circuit breaker ", *IEEE Trans. on Power Delivery,* Vol.6, No.2, April 1991.

[27] T. Adachi, H. Tsujimura, and M. Imaizumi: "A numerical method of unsteady flow analysis in duct with junction," *Transactions of the Japan Society of Mechanical Engineers*, Vol. 43, No. 366, pp. 596 – 604, February 1977 (In Japanese)

[28] L. S. Frost and R. W. Liebermann: "Composition and transport properties of SF_6 and their use in a simplified enthalpy flow arc model," *Proc. IEEE*, Vol. 59, pp. 474-485, April 1971

[29] H. K. Kim, B. Y. Lee, K. D. Song, K. Y. Park, J. Y. Lee, and H. K. Jung: "Numerical analysis of hot gas flow in SF6 GCB using the method of partial characteristics and FVFLIC method", *Proceedings of 14th International Conference on Gas Discharges and their Applications*, Vol.I, pp.75-78, September 2002

[30] J. Y. Trépanier, M. Reggio, H. Zhang, and R. Camarero: "A finite-volume method for the Euler equations on arbitrary Lagrangian-Eulerian grids," *Computers Fluids*, Vol. 20, No. 4, pp. 399-409, 1991

[31] M. Reggio, J. Y. Trépanier, D. Dufoumet, and V. Gindre: "Computation of the gas flow and electrical fields in SF_6 circuit-breakers", *Proceedings. of 10th International Conference on Gas Discharges and Their Applications*, Sep. 1992

[32] J. Y. Trépanier, M. Reggio, M. Paraschivoiu, and R. Camarero: "Unsteady Euler solutions for arbitrarily moving bodies and boundaries," *AAIA Journal*, Vol. 31, No. 10, pp. 1869-1876, Oct. 1993

[33] Ph Robin-Jouan and N. Kairouain: "Numerical and experimental analysis of the propagation of hot plasma in high voltage circuit-breakers", *Proceedings. of 14th International Conference on Gas Discharges and Their Applications*, pp.103-106, September 2002

[34] J. D. Yan, and M. T. C. Fang: "Visualization of arcing process in an auto-expansion circuit-breaker," *IEEE Trans. on Plasma Science,* Vol.27, No.1, pp. 40-41, Feb. 1999.

[35] For example, http://www.phoenics.co.jp/

[36] T. Mori, K. Iwamoto, T. Nakamoto, and K. Suzuki: "Development of gas flow simulation method considering ablation for GCB chambers," *The Papers of Technical Meeting on Switching & Protecting Eng*., *IEEJ*, SP-99-86, pp.61-66, 1999 (In Japanese)

[37] M. Lindmayer: "Complete simulation of moving arcs in low-voltage switchgear", *Proceedings. of 14th International Conference on Gas Discharges and Their Applications*, Vol.II, pp.318-324, September 2002

[38] T. Sakuta, S. Terachi, T. Takashima, and M. Ishikawa: "Transport properties of high temperature SF_6 gas contaminated with Cu and PTFE vapour at high pressure condition", *IEEJ Transactions*, Vol. 113-B, No.4, pp.342-350, April 1993 (In Japanese)

[39] Y. Tanaka, K. C. Paul, and T. Sakuta: "Thermodynamic and Transport Properties of N_2/O_2 Mixtures at Different Admixture Ratios", *Trans. IEEJ*, Vol. 120-B, pp. 24-30, 2000.

[40] K. C. Paul, T. Sakuta, and T. Takashima: "Transport and thermodynamic properties of SF_6 gas contaminated by PTFE reinforced with Al_2O_3 ad BN particles", *IEEE Trans. on Plasma Sci.*, Vol. 25, pp. 786-798, 1997.

[41] J. M. Yos: "Transport Properties of Nitrogen, Hydrogen, Oxygen, and Air to 30,000K", *Research and Advanced Development Division AVCO Corporation*, Massachusetts, 1967, Amendments to AVCO RAD-TM-63-7

Chapter 2 Development of Hybrid-Puffer^{TM}-type 300-kV 63-kA GCB

2.1 Introduction

In Japan during 1980s and 1990s, as a countermeasure to the increase and the concentration of demand of electric energy in large cities, trunk electric power lines were expanded and its nominal voltage was elevated from 154- to 275- and 550-kV. Furthermore, as an ultra-high voltage (UHV) system, a trial facility of 1000-kV power system was constructed and tested. The expansion of the electric power system may cause the increase in the fault current or short circuit capacity. Gas circuit breakers (GCBs) were therefore demanded to have higher voltage and larger interrupting capacity, and 550-kV 63-kA 1-break GCB [1] and 1000-kV 50-kA 2-breaks GCB [2] had been developed by 1995.

As to the 275-kV system, the system had been constructed so that the short circuit current was less than 50 kA and the GCB had been designed to have the standard interruption current of 50 kA. However, the short circuit current was going to exceed 50 kA due to the system expansion. Therefore, a GCB with the interruption current of 63 kA had needed to be developed rapidly. It was considered necessary to use the larger tank size and stronger operating mechanism for the interruption of 63 kA because the arc energy would increase. However, substations constructed underground, where a space was limited and expensive, should be as small as possible. The reduction of size was also important for substations in mountainous area for protecting the nature. Adding to that, in view of a speedy upgrading from 50 kA to 63 kA and reducing the costs, it was important to make compatibility between 50- and 63-kA GCBs by size reduction of an interruption chamber. Moreover, 3-phase-1-tank

type GCB, which was much effective for reducing a substation size [2], also needed to be developed with an interruption current of 63 kA.

In this chapter, problems and new technologies for development of a large capacity and compact size 300-kV 63-kA puffer-type GCB will be discussed.

2.2 Difficulties for developing large capacity and compact size GCBs

2.2.1 Problems for BTF interruption

2.2.1.1 Raising the ability of cooling the arc

An increase of interruption current of the breaker-terminal fault (BTF) from 50 kA to 63 kA results in an increase of arc energy generated between arcing contacts. The ability of cooling an arc in the 63-kA GCB should be raised from that in the 50-kA GCB to improve dielectric recovery characteristics and to achieve a successful large current interruption.

2.2.1.2 More efficient hot gas exhaust

An increase of an interruption current from 50 kA to 63 kA also results in an increase of generated hot gas. In a conventional 50-kA GCB, the hot gas was urged to be exhausted by ventilation holes in an exhausting cylinder around a stationary arcing contact to the space from a phase to a tank or between phases [3]. But in the case of a 63-kA GCB, such a construction may reduce the dielectric strength after the current interruption in that space. For this problem, the hot gas must be exhausted more efficiently from interruption chamber.

2.2.2 Problems for SLF interruption

Due to an increase of an interruption current from 50 kA to 63 kA, the rate of rise of the recovery voltage (rrrv) and the rate of decrease of current at the current zero point become larger by 26 %, which makes the short-line fault (SLF) interruption difficult. As explained in Chapter 1, installing capacitance in GCB is one of countermeasure reducing rrrv, but no

capacitance is permitted parallel to the contacts for the new 300-kV GCB. Therefore, to cope with this severe situation, higher puffer chamber pressure is needed.

2.2.3 Problems for small capacitive current interruption

As a result of attempting to interrupt larger currents, increasing the puffer chamber pressure may lead to pressure fluctuations caused by super-sonic gas-flow between contacts. It is known that such fluctuations could worsen the small capacitive current interruption performance. Increasing the contact opening speed may improve dielectric strength after the small capacitive current interruption by departing contacts each other quickly. However, it should be avoided because it requires a large operating mechanism, which makes the GCB larger and expensive. To solve these problems, the gas pressure fluctuation between arcing contacts must be controlled at a low level.

2.3 Gas-flow control between arcing contacts

2.3.1 Control of mass-flow contributing to arc cooling

The schematic structure of a conventional interruption chamber is shown in Fig. 2.1. The gas compressed in a puffer chamber blasts the arcing area through the path between the movable arcing contact and the nozzle. The gas-flow is separated at the stagnation point into two directions, one towards the stationary arcing contact and the other towards the movable arcing contact. These gas-flows cool arcs. Efficient arc cooling is important for interrupting large currents [4]. But if the balance of these gas-flows is not proper, some part of the gas-flow is not used in the cooling process properly. Controlling the balance of these gas-flows properly must improve the performance of large current interruption.

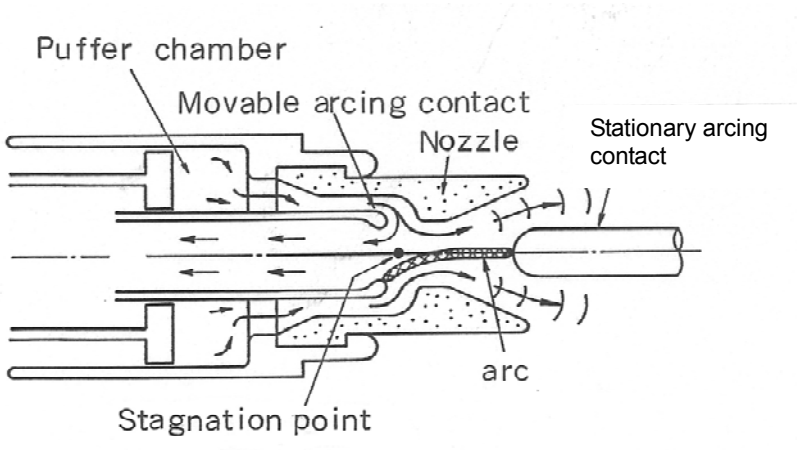

Figure 2.1 Schematic structure of a conventional interruption chamber

For this reason, the gas pressures in two directions were measured, and then, the mass-flow rate at each gas-flow was calculated from the measured pressure.

2.3.1.1 Measurements of the mass-flow rate

Figure 2.2 shows a model chamber for the gas pressure measurement. The model chamber is same size with a 300-kV model GCB for interruption tests and operation mechanism is also the same. It is installed in a gas tank in which SF_6 gas of 0.5 MPa is filled. To know the mass-flow, semi-conductor-type pressure transducers were set in a puffer chamber P, on the surface of nozzle N1, N2, N3, N4, on the inside surface of the movable arcing contact M, and on the tip of stationary contact F shown in Fig. 2.2. Gas compressed in a puffer chamber flows out to area between the stationary arcing contact and movable arcing contacts. Part of the gas-flows towards the stationary arcing contact, the rest flows towards the movable arcing contacts, and a stagnation point appears at the boundary of them. The mass-flow rate in each direction from the stagnation point can be obtained by using pressure values P_{P}, P_{N1}, P_{M}, as follows:

$$Q_{\mathrm{S}} = \sqrt{\gamma RT} \cdot M_{\mathrm{N1}} \cdot S_{\mathrm{N1}} \cdot \rho_{\mathrm{N1}}, \tag{2.1}$$

$$Q_{\mathrm{M}} = \sqrt{\gamma RT} \cdot M_{\mathrm{M}} \cdot S_{\mathrm{M}} \cdot \rho_{\mathrm{M}}, \tag{2.2}$$

$$\rho_{\mathrm{N1}} = \rho_{\mathrm{P}} (P_{\mathrm{N1}} / P_{\mathrm{P}})^{1/\gamma}, \tag{2.3}$$

$$\rho_{\mathrm{M}} = \rho_{\mathrm{P}} (P_{\mathrm{M}} / P_{\mathrm{P}})^{1/\gamma}, \tag{2.4}$$

$$M_{\mathrm{N1}} = \sqrt{\frac{2}{\gamma - 1}\left[(P_{\mathrm{N1}} / P_{\mathrm{P}})^{(1-\gamma)/\gamma} - 1\right]}, \tag{2.5}$$

$$M_{\mathrm{M}} = \sqrt{\frac{2}{\gamma - 1}\left[(P_{\mathrm{M}} / P_{\mathrm{P}})^{(1-\gamma)/\gamma} - 1\right]}\ , \tag{2.6}$$

where,

Q_{S} : mass-flow rate in stationary arcing contact direction,

Q_{M} : mass-flow rate in movable arcing contact direction,

γ : ratio of specific heats, ρ_{N1} :gas mass density at N1,

R : gas constant, ρ_{M} : gas mass density at M,

T : temperature, ρ_{P} : gas mass density at P

M_{N1} : mach number at N1,

M_{M} : mach number at M,

S_{N1} : cross section of gas passageway at N1,

S_{M} : cross section of gas passageway at M,

the equations of adiabatic flow state are used,.

the gas in the puffer chamber is regarded as a perfect gas.

The Q_{S} and Q_{M} are obtained from measured pressures in no-load operation of the model GCB. An example of the ratio between the two mass-flow rates, $Q_{\mathrm{S}} / Q_{\mathrm{M}}$, is shown in Fig. 2.3 with dashed line denoted by “without inner-nozzle”. The ratio is almost equal to 1 after the contact travels 40 % of the full travel length. This means that the mass-flow rate in a movable arcing contact direction is comparably equal to the one in a stationary arcing contact direction. On the other hand, the ratio of the arc length from the stagnation point to the stationary arcing contact to the one to the movable arcing contact is 10:1 in fully opened position. This means that the arc length of the stationary arcing contact side is ten times longer. Thus the gas-flow towards the stationary arcing contact must cool much longer arcs

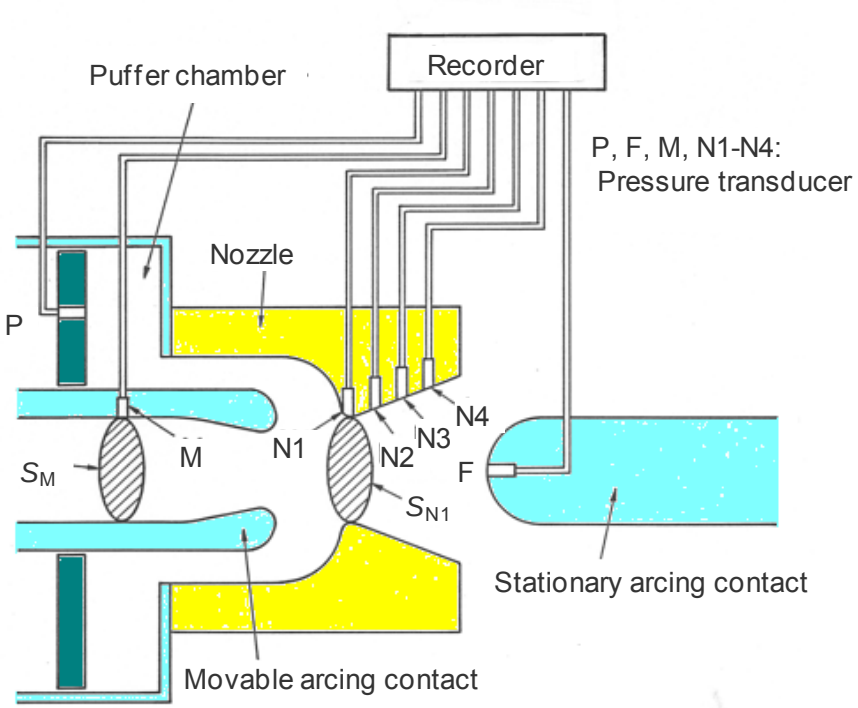

Figure 2.2 Apparatus for gas pressure measurement

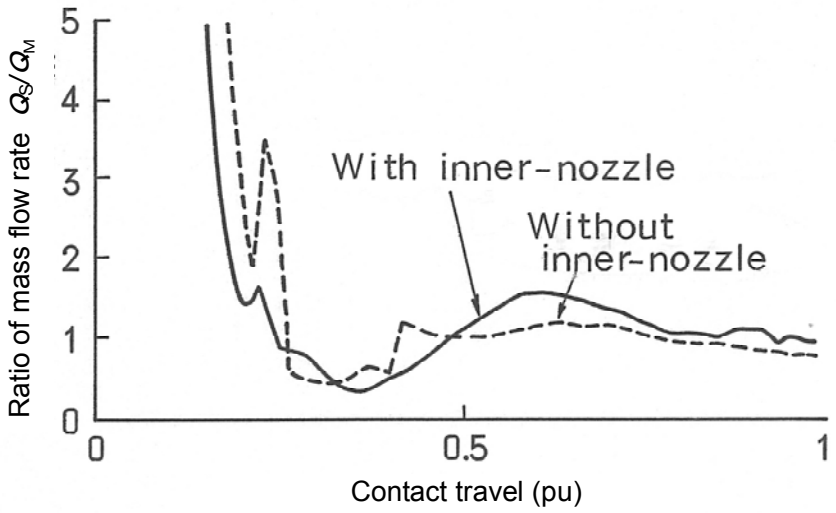

Figure 2.3 Ratio of mass-flow rate

than towards movable arcing contact, which is considered to be unbalanced.

Therefore, to balance cooling for each arc length, the stagnation point was moved to the stationary arcing contact by adopting an additional nozzle on the movable arcing contact side, which was called an inner-nozzle in this thesis. The conceptual figure of the inner-nozzle is shown in Fig. 2.4. The ratio of mass-flow with the inner-nozzle is still about 1, as shown in Fig. 2.3.

In the sense of balancing arc cooling duty, it is desirable that the stagnation point is located at the centre between arcing contacts. A thick or long inner-nozzle should be installed to shift the stagnation point farer, and the nozzle throat is designed much shifted towards the stationary contact direction to attach the inner-nozzle. But the minimum arcing time is achieved only after the nozzle throat passes the tip of the stationary arcing contact when the mass-flow is increased. Therefore, making nozzle throat towards the stationary arcing contact means that the minimum arcing time becomes longer and that there are possibilities to fail to interrupt current within 2-cycles which is required abilities to this GCB. With taking these conditions into consideration, the length of the inner-nozzle was designed properly, and the stagnation point was moved towards a stationary arcing contact at proper distance. Cross-sectional area of gas-flow channel between the inner-nozzle and the nozzle was kept same with that without inner-nozzle.

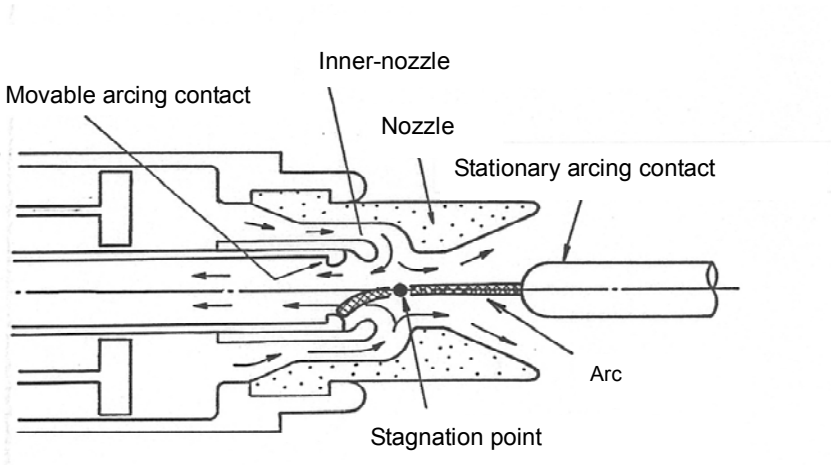

Figure 2.4 Schematic figure of interruption chamber with inner-nozzle

2.3.1.2 Improvement of hot gas exhaust performance by inner-nozzle

The hot-gas-flow simulations were carried out for interruption chambers with and without the inner-nozzle by the modified fluid-in-cell (FLIC) method [5]. The example of the cells used in the simulation is shown in Fig. 2.5. Arc energies are input in shaded cells between the stationary contact and the movable one in Fig. 2.5.

Figure 2.6 shows the results of the density profiles at current zero when interrupting a current of 50 kA (arcing time 20 ms). In the chamber with the inner-nozzle (Fig. 2.6(a)), a density between the stationary arcing contact and the stagnation point is over 25 kg/m^3, while an area under 10 kg/m^3 exists around the stationary arcing contact in the chamber without inner-nozzle (Fig. 2.6(b)). On the other hand, area where the density is under 10 kg/m^3 is widely spread downstream of the movable arcing contacts in the chamber with inner-nozzle, while less area exists in the chamber without inner-nozzle. These are the results of increasing the arc energy exhaust towards in the movable arcing contact direction and decreasing the arc energy exhaust in the stationary arcing contact direction, because the arc energy exhaust increases the temperature and decreases the gas density.

The distribution of the density at the front of the tip of the stationary arcing contact at current zero is shown in Fig. 2.7. When the current of 63 kA was interrupted by a GCB without the inner-nozzle, the gas density decreased compared to the 50-kA interruption. On the other hand, at the interruption of 63 kA by the chamber adopting the inner-nozzle, the density was higher than that of 50-kA interruption without an inner-nozzle. The density was increased around the tip of the stationary arcing contact by using an inner-nozzle, which meant that dielectric interruption ability such as T100s became better.

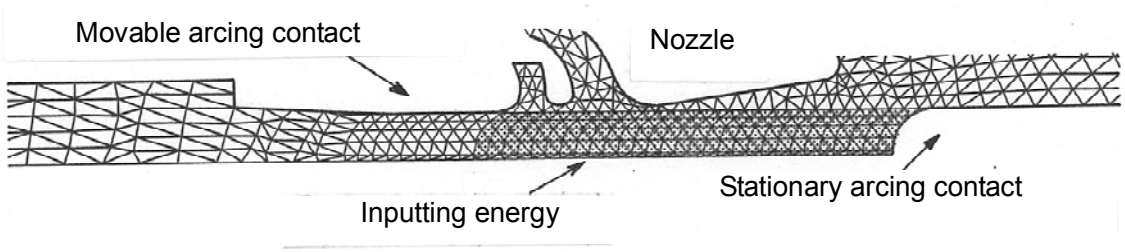

Figure 2.5 Cells for hot-gas-flow simulation

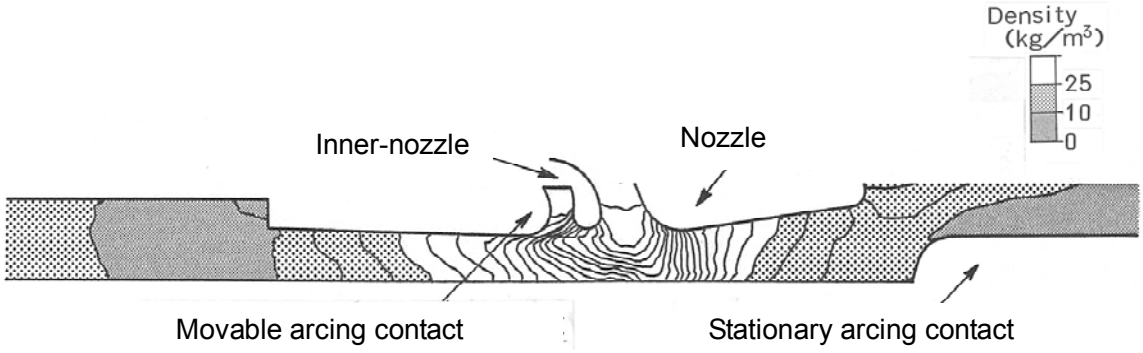

(a) With inner-nozzle

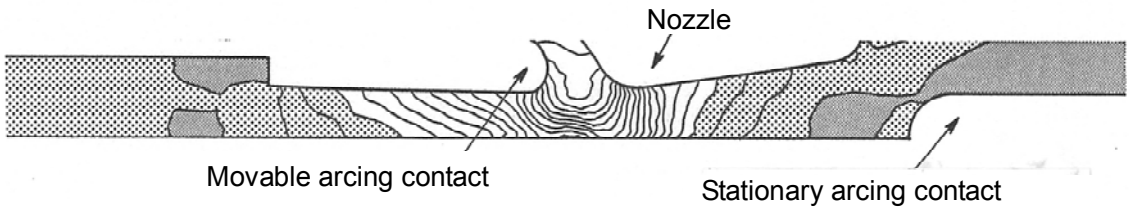

(b) Without inner-nozzle

Figure 2.6 Results of hot-gas-flow simulation between arcing contacts
(At current zero)
: Interrupting current 50kA, arcing time 20ms

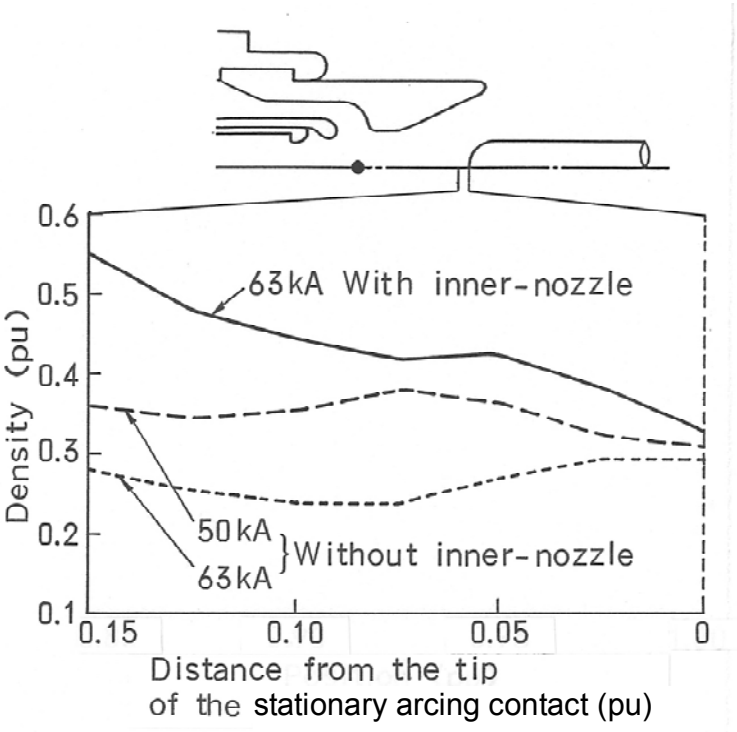

Figure 2.7 Distribution of density
(At current zero)

2.3.2 Increase of puffer chamber pressure by adopting inner-nozzle

In the development of a chamber for the 63-kA GCB, the Hybrid-puffer^{TM}-type chamber was employed to increase puffer chamber pressure [6]. In this scheme, the arc energy located between the movable arcing contact and the nozzle throat is led into puffer chamber as explained in Chapter 1. By adopting the inner-nozzle with this scheme, the arc energy becomes more efficiently utilised. In the case of having a long arc length, the puffer chamber pressure with the inner-nozzle becomes higher than that without inner-nozzle. In the hot gas simulation shown in Section 2.3.1 (Fig. 2.6), the gas pressure rise in the puffer chamber with the inner-nozzle was 1.22 times higher than that without inner-nozzle.

2.3.3 Influence of inner-nozzle to small capacitive current interruption performance

As described above, the inner-nozzle was expected to improve the large current interruption performance. In this section, the investigations related to small capacitive current interruption with the inner-nozzle chamber are shown.

2.3.3.1 Measurements of gas-flow fluctuation in space between arcing contacts

To investigate the small current interruption performance, the gas pressure fluctuations were measured with two kinds of interruption chamber without current interruption. The measurement points were located at P in the puffer chamber, the stationary arcing contact F, and the nozzle surface N1-N4 as shown in Fig. 2.2. From now on, in this chapter, the chamber adopting an inner-nozzle is called as A-chamber, and that without an inner-nozzle is called as B-chamber.

The measured fluctuation at the stationary arcing contact F, P_F, is shown in Fig. 2.8 as a

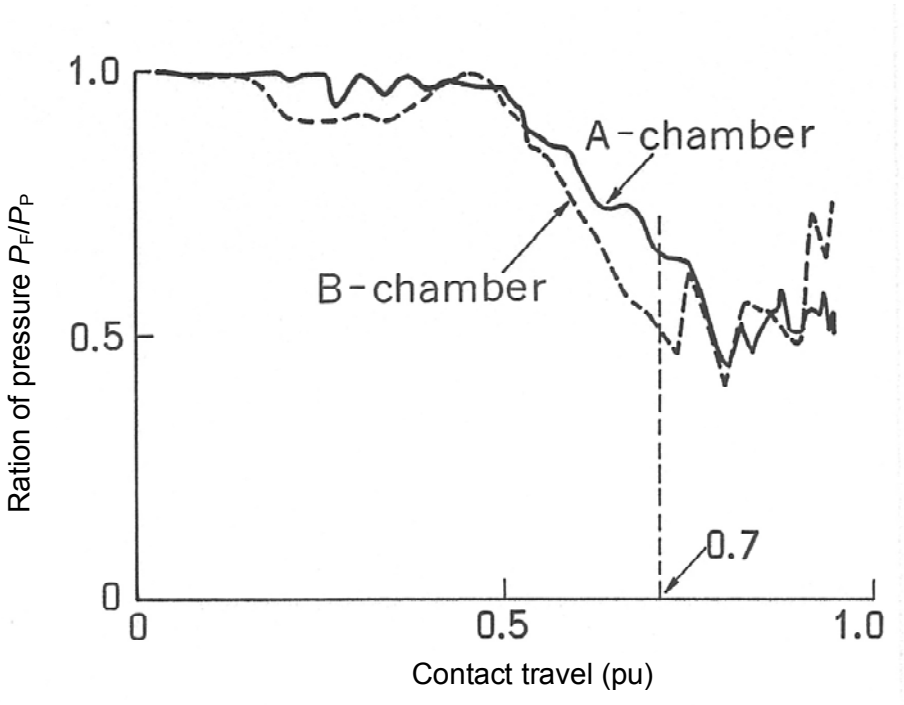

Figure 2.8 Pressure at the tip of the stationary arcing contact against pressure in a puffer chamber

ratio against the pressure P_P in the puffer chamber at P. The axis of abscissa represents the contact travel. Between contact travel 0.55 p.u. and 0.75 p.u., the ratio of the A-chamber is higher than that of the B-chamber, especially around 0.7 p.u.

Figure 2.9 shows the ratios of pressure at nozzle surface points N1-N4 against pressure at puffer chamber P for contact travel 0.7 p.u.. In SF_6 gas-flow, provided that the ratio of the upstream pressure against the downstream pressure is less than 0.57, the downstream flow would become supersonic. The downstream gas-flow from nozzle throat is accelerated and the pressure in that area becomes lower than that at the nozzle throat in supersonic condition. In Fig. 2.9, pressure values at all measurement points in the B-chamber are in the super-sonic condition. In this case, the pressure might drop lower in downstream of the nozzle throat, which causes a negative effect on the dielectric recovery characteristic. On the other hand all values in A-chamber show that super-sonic condition does not occur. In that case, the pressure may not drop low in downstream, and it is estimated that the dielectric recovery characteristic is better.

2.3.3.2 Dielectric recovery characteristic

The breakdown voltage during the contact opening depends on the electric field strength

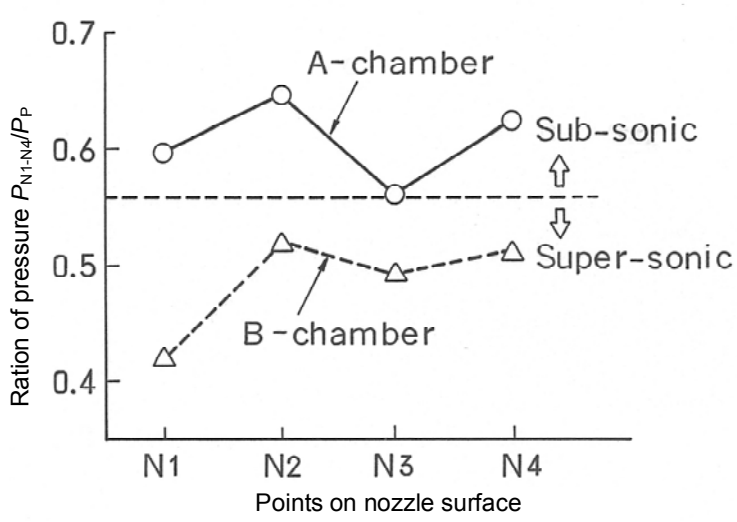

.Figure 2.9 Pressure ratio on a nozzle surface against pressure in a puffer chamber

E and the gas density ρ in the space between arcing contacts [7]. In previous work, it has been measured that E/ρ was the highest at the tip of arcing contact [1]. But due to the limitation of number of measurement points, it was difficult to know whether the maximums existed locally between the measurement points or not. Therefore, E/ρ value was calculated from E and ρ in the chamber with an inner-nozzle. The results are shown in Fig. 2.10. Since contacts are separating, the local maximum may appear in the space between the nozzle throat and the stationary arcing contact. But the E/ρ at the tip of the stationary arcing contact is always much higher than the local maximum. Consequently, using E or ρ of the tip of the stationary arcing contact is reasonable in evaluating small capacitive current interruption ability. By using this method, it is estimated that the small capacitive current interruption ability of A-chamber is enough for the voltage factor k=1.4.

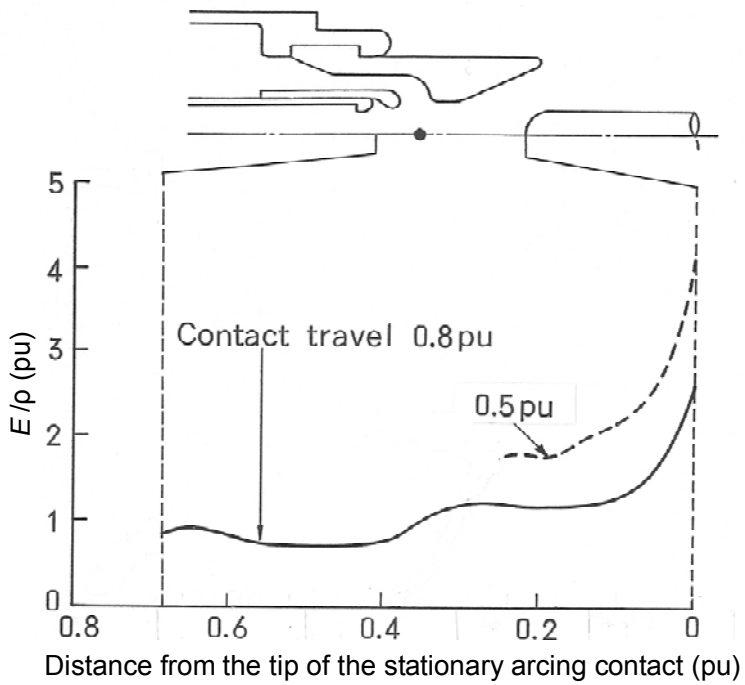

Figure 2.10 Distribution of E/ρ
(Chamber A)

2.4 Investigation of diffusion of downstream hot gas

To keep the dielectric strength after interrupting current of 63 kA between phases or a phase to a dead tank of which size was same as a conventional 50-kA GCB, hot gas diffusion was investigated and the influence of the configuration on the interruption ability has been considered.

The diffusion of a hot gas was measured by using the apparatus shown in Fig. 2.11. The small gap electrodes, without disturbing the gas-flow, were placed in an exhaust cylinder. In this method, a high frequency voltage shown in Fig. 2.12 was applied to gaps [3] [8]. When the hot gas reaches the gaps, the break down voltage suddenly changes. The times when the hog gas arrives at the gaps are illustrated in Fig. 2.13. At the position far from the axis, the appearance of the hot gas is delayed for 2–6 ms compared to that near axis. This means that hot gas travelled rather straightforward in the exhaust cylinder and diffused gradually in a radial direction after interrupting a current of 50 kA.

The density profile obtained by the modified FLIC is shown in Fig. 2.14. This figure shows the equal-density contours at the current interruption of 63 kA and an arcing time of

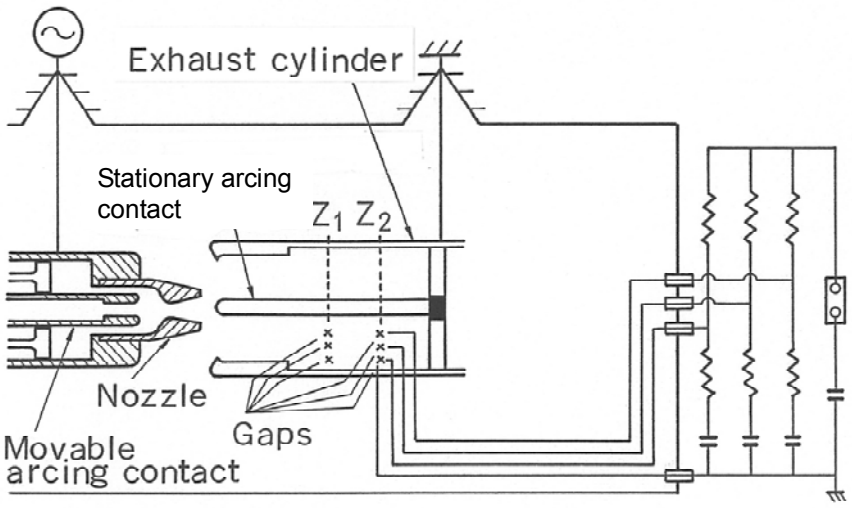

Figure 2.11 Apparatus for measurement of hot gas diffusion

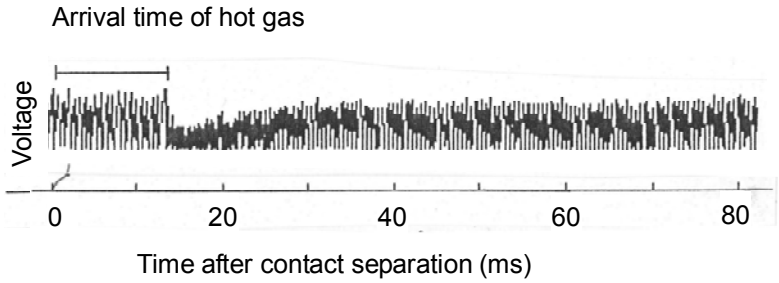

Figure 2.12 Oscillogram of voltage between small gaps

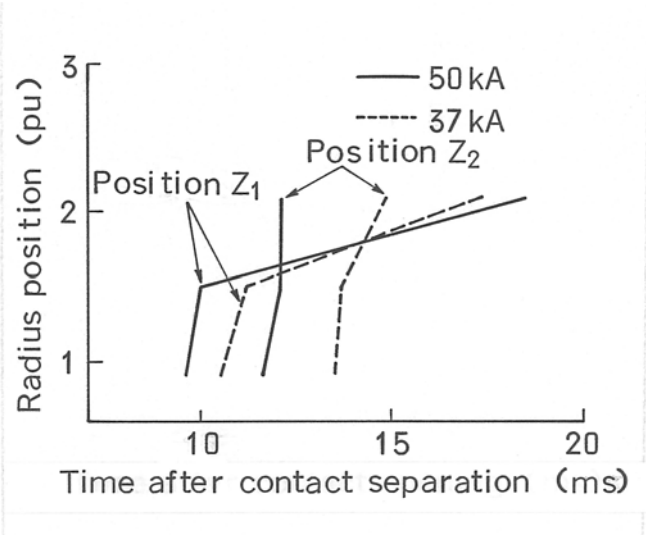

Figure 2.13 Hot gas arrival time

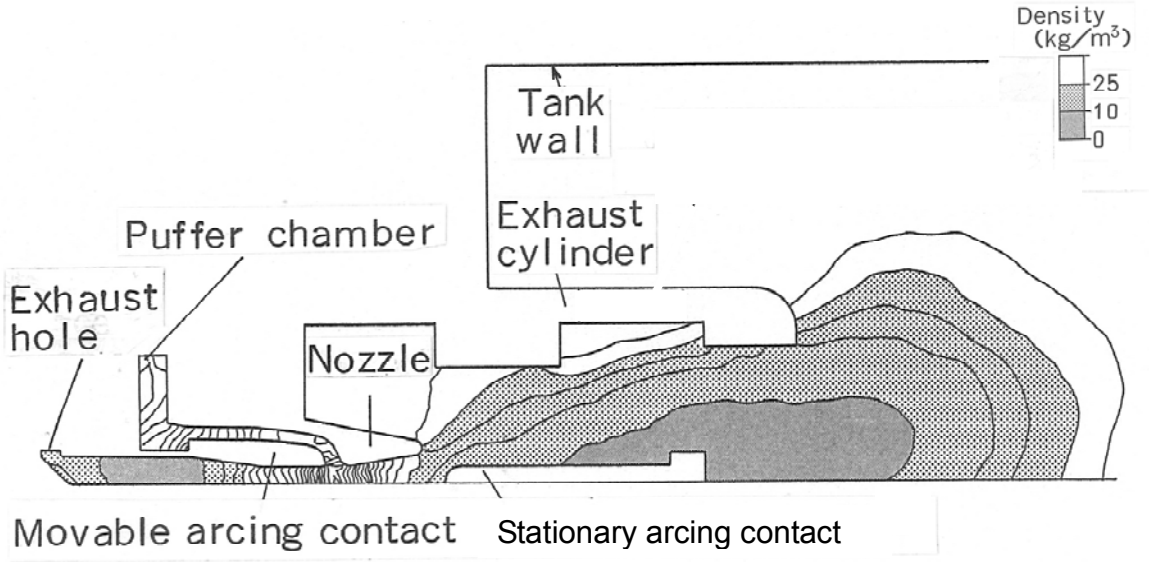

Figure 2.14 Result of hot-gas-flow simulation in exhaust cylinder

20 ms. The hot gas flowed smoothly downstream, without stagnating in the exhaust cylinder.

Judging from the results of measurements and simulations, the interruption performance would be secured in the tank of which size is same as a conventional 50 kA-GCB by adopting proper designs of the exhaust cylinder.

2.5 Interruption tests

Three major interruption tests were carried out for advanced GCB with above-mentions improvements.

2.5.1 BTF interruption test

Figure 2.15 shows an example of oscillograms of a T100s interruption test. Both T100s and T100a were cleared. As far as the 3-phase-1-tank-type GCB is concerned, it was confirmed that the first, the second and the third phase were all successfully interrupted.

2.5.2 SLF interruption test

The measured pressure rises in the puffer chamber at L90 interruption are shown in Fig. 2.16. The pressure rise in the model GCB with an inner-nozzle was 1.24 times higher than that without an inner-nozzle. This shows that the scheme for the pressure rise successfully contributed to improvement of the SLF interruption performance. The 50-Hz 63-kA GCB could achieve L90 interruption without extra capacitors.

2.5.3 Capacitive current interruption test

As a test result, it was verified that the current up to a test voltage factor of 1.4 in a single-phase test could be interrupted without restrikes.

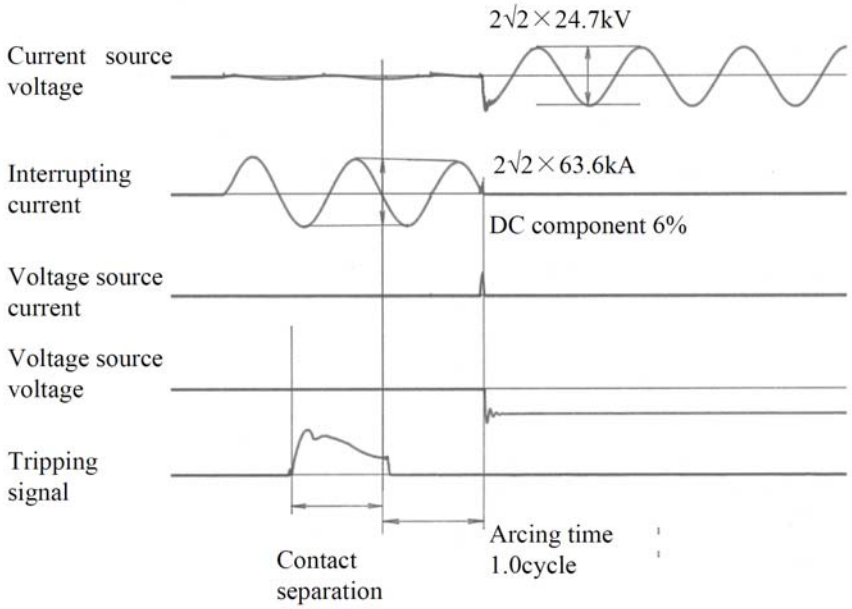

(a) Current, voltage and tripping signal

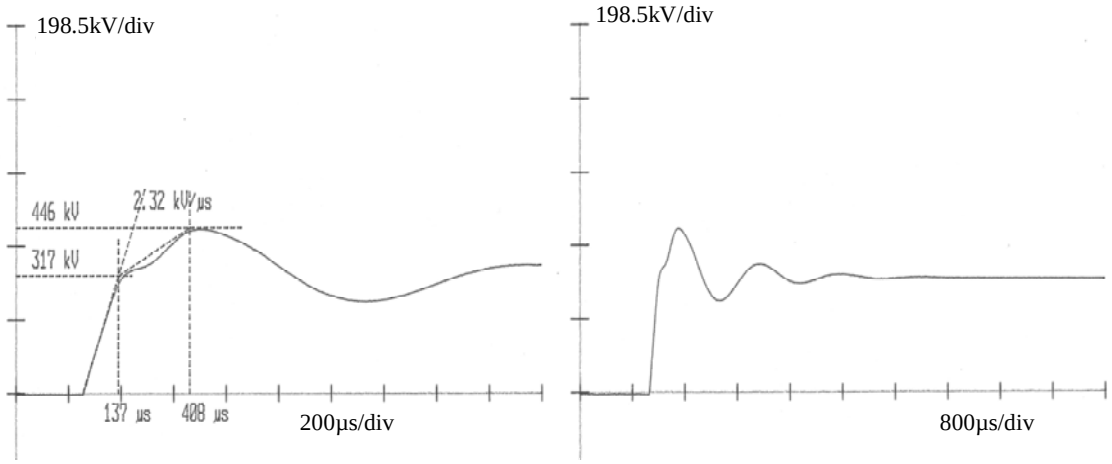

(b) TRV

Figure 2.15 Oscillograms at T100s with 300-kV 63-kA GCB

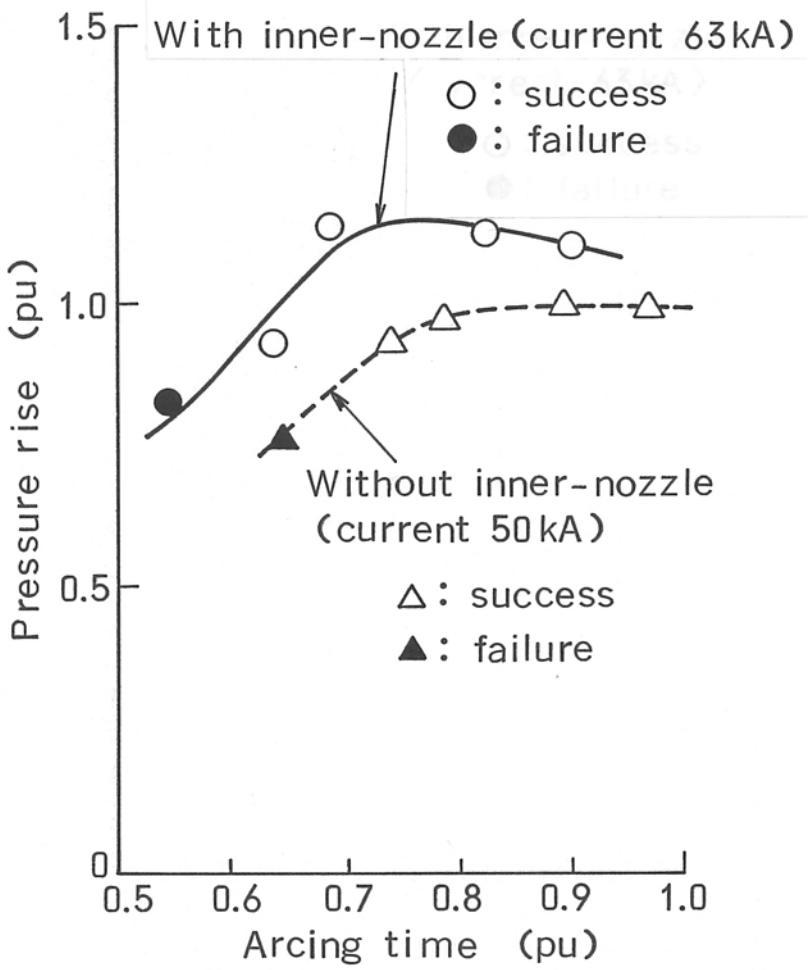

Fig. 2.16 Pressure rise at L90 interruption

2.6 Discussion

2.6.1 Effects of inner-nozzle on SLF interruption performance

The shape factor K, a constant value for each interruption chamber which does not include the effect of pressure rise in the puffer chamber, is defined as Eq. (1.1):

$$K \cdot {P_{\min}}^{\alpha} = \frac{\mathrm{d}u}{\mathrm{d}t} \cdot \left(\frac{\mathrm{d}i}{\mathrm{d}t} \right)^{\beta}, \tag{1.1}$$

where, $P_{\min}$ is minimum pressure rise of a successful interruption, α and β are 1.6 and 2.4, respectively. Representing subtitle B for 300-kV 50-kA interrupter without inner-nozzle and subtitle A for 300-kV 63-kA interrupter with inner-nozzle, the Eq. (1.1) is represented as Eqs. (2.7) and (2.8),

$$K_{\mathrm{B}} \cdot {P_{\mathrm{B}\min}}^{\alpha} = \left(\frac{\mathrm{d}u}{\mathrm{d}t}\right)_{\mathrm{B}} \cdot \left(\frac{\mathrm{d}i}{\mathrm{d}t}\right)_{\mathrm{B}}^{\beta}, \tag{2.7}$$

$$K_{\mathrm{A}} \cdot {P_{\mathrm{A}\min}}^{\alpha} = \left(\frac{\mathrm{d}u}{\mathrm{d}t}\right)_{\mathrm{A}} \cdot \left(\frac{\mathrm{d}i}{\mathrm{d}t}\right)_{\mathrm{A}}^{\beta}. \tag{2.8}$$

Dividing both sides of the Eq. (2.8) by the Eq. (2.7), Eq. (2.9) is obtained,

$$\frac{K_{\mathrm{A}}}{K_{\mathrm{B}}} = \frac{\left(\frac{\mathrm{d}u}{\mathrm{d}t}\right)_{\mathrm{A}}}{\left(\frac{\mathrm{d}u}{\mathrm{d}t}\right)_{\mathrm{B}}} \cdot \frac{\left[\left(\frac{\mathrm{d}i}{\mathrm{d}t}\right)_{\mathrm{A}} \Big/ \left(\frac{\mathrm{d}i}{\mathrm{d}t}\right)_{\mathrm{B}}\right]^{\beta}}{(P_{\mathrm{A}\min} / P_{\mathrm{B}\min})^{\alpha}}. \tag{2.9}$$

Both of $\left(\frac{\mathrm{d}u}{\mathrm{d}t}\right)_{\mathrm{A}} \Big/ \left(\frac{\mathrm{d}u}{\mathrm{d}t}\right)_{\mathrm{B}}$ and $\left(\frac{\mathrm{d}i}{\mathrm{d}t}\right)_{\mathrm{A}} \Big/ \left(\frac{\mathrm{d}i}{\mathrm{d}t}\right)_{\mathrm{B}}$ are 1.26 which is equal to 63 kA / 50 kA as defined by IEC [9]. From the SLF interruption test in the Section 2.5.2, the $P_{\mathrm{A}\min} / P_{\mathrm{B}\min}$ is 1.24. The $K_{\mathrm{A}} / K_{\mathrm{B}}$ is calculated as 1.56, which means that the shape factor *K* of the new 63-kA GCB with the inner-nozzle is 1.56 times higher than that for the 50-kA GCB without the inner-nozzle. This result suggests that the inner-nozzle contributes to the thermal interruption by not only the pressure rise of a puffer chamber but also other unknown effects.

2.6.2 Effects of size reduction

As a result of investigations explained in this chapter, it was confirmed that the same size of a tank and the same hydraulic operating mechanism as those of 50-kA GCB could be applied to single-phase 63-kA GCB and 3-phase-1-tank-type. This means that when the short

circuit current increases above 50 kA in the system by some reasons, the only thing to do is exchange of the interruption chamber in the site, which is advantageous to the utilities.

2.7 Conclusions

This chapter discussed technologies for developing new 300-kV 63-kA GCB keeping its size compact.

(a) Employing an inner-nozzle was effective to develop GCB of large-capacity and compact size, due to the mass-flow controlling that contributed to the arc cooling.

(b) Combined use of the Hybrid-puffer^{TM} and an inner-nozzle was effective, because of the efficient pressure rise in a puffer chamber.

(c) The inner-nozzle also affected the small current interruption performance favourably.

(d) The 63-kA current interruption was achieved successfully in the same size of tank of 50-kA GCB without any grounding faults.

As a result of above studies, it was confirmed that the 63-kA GCB was achievable with changing interruption units using enclosing-tanks and operating-mechanism of the conventional 50-kA GCB.

Knowledge found in this chapter were introduced to development of other new GCBs, including 300-kV 50-kA [10], 168- kV GCB [11], 420-kV GCB [12], as well as 300-kV 63-kA GCB itself.

References

[1] K. Suzuki, H. Toda, A. Aoyagi, H. Ikeda, A. Kobayashi, I. Oshima, and S. Yanabu: " Development of 550kV 1-break GCB (PART I) - Investigation of interrupting chamber performance - ", *IEEE Power Engineering Society for presentation at the IEEE/PES Summer Meeting,* 92 SM 577-7 PWRD, 1992.

[2] K. Tanaka, K. Kudo, N. Miyake, K. Suzuki, and H. Sato: “Full pole interrupting test for 1000 kV gas circuit breaker”, *1995 National Convention Record I.E.E. Japan* , No. 1465, 1995 (In Japanese).

[3] K. Suzuki, H. Ikeda, H. Mizoguchi, Y. Ozaki, and S. Yanabu: “ Investigation of interruption performance of newly developed 300kV 3-phase-in-one-tank-type GCB and its application to a reduced size GIS ", *IEEE Trans. on Power Delivery,* Vol.4, No.1, 1989.

[4] H. Ikeda, M. Ishikawa, and S. Yanabu: "Analyses of axial energy distribution in decaying arc of SF_6 gas circuit breaker ", *IEEE Trans. on Plasma Science,* Vol.14, No.4, 1986.

[5] M. Okamoto, M. Ishikawa, K. Suzuki, and H. Ikeda: "Computer simulation of phenomena associated with hot gas in puffer-type gas circuit breaker ", *IEEE Trans. on Power Delivery,* Vol.6, No.2, April 1991.

[6] S. Yanabu, H. Mizoguchi, H. Ikeda, K. Suzuki, and M. Toyoda: "Development of novel Hybrid Puffer interrupting chamber for SF_6 gas circuit breaker utilizing self-pressure-rise phenomena by arc ", *IEEE Trans. on Power Delivery,* Vol.4, No.1, 1989.

[7] J. Y. Trepanier, M. Reggio, Y. Lauze, and R. Jeanjean: “Analysis of the dielectric strength of an SF_6 circuit breaker “, *IEEE Power Engineering Society for presentation at the IEEE/PES 1990 Summer Meeting*, SM 411-9 PWRD, 1990.

[8] S. Sugiyama, H. Iwai, A. Matsumoto, K. Tsuchikawa, and K. Iwata: "Measurement of

dielectric strength in SF_6 gas flow", *Switchgear and Protects Society of Japan*, SPD-88-16, June, 1988 (In Japanese).

[9] IEC International Standard 62271-100

[10] K. Matsushita, H. Ohashi, and K. Inoue: “Development of new 300 kV-50 kA GCB”, *1994 National Convention Record I.E.E. Japan*, No.1491, 1994 (In Japanese).

[11] T. Mineyama, S. Nishizumi, M. Toyoda, A. Kobayashi, and T. Yokota: “Development of compact 168/204kV GCB”, *1996 National Convention Record I.E.E. Japan*, No.1510, 1996 (In Japanese).

[12] M. Toyoda, H. Mizoguchi, S. Higashi, Y. Ozawa, and A. Kobayashi: “Development of single break 420 kV GCB”, *Proceedings of IEEE Power Engineering Society Winter Meeting 2000*, Vol. 3, No. 23-27, pp. 2118-2113, Jan. 2000.

Chapter 3 Investigation of Two Types of Interruption Chamber with Low Operating Energy for 245-kV GCB

3.1 Introduction

After completion of 550-kV 63-kA 1-break gas circuit breaker (GCB) and 300-kV 63-kA GCB, demands from power industry markets had shifted to compact size and low cost GCBs, rather than high voltage and large capacity ones. From the viewpoint of manufacturing GCBs, downsizing and simplifying operating mechanism are very effective to cost reductions. Therefore, research and development activities were targeted on the chamber with low operating energy, even though a structure of the chamber becomes more complex.

In the middle of 1990's with background above, it was decided that a target of a new 245-kV GCB with a hydraulic operating mechanism of which energy was 1.5 kJ. This operating energy was 1/3 of a conventional type GCB. Numerical investigations for two types of chambers have been carried out to develop the new GCB in this chapter. One of the chambers was the one volume and one piston type interruption chamber (1vol-1pis) of which configuration was basically same with the Hybrid –puffer^{TM}-type. To reduce repulsive force on the puffer piston, it was considered that the diameter of the piston of the 1vol-1pos was tried to be small. But it was apprehended that making the puffer piston small resulted in the lack of pressure rise and the failure under short-line fault (SLF) interruption condition. To compensate the decrease of the pressure in the puffer chamber, two volumes and two pistons type interruption chamber (2vol-2pis) was proposed and was compared with the 1vol-1pis for getting better solution.

It have been confirmed that the 2vol-2pis could generate sufficiently high pressure. It was also found that 1vol-1pis could generate a sufficiently high pressure comparable to the 2vol-

2pis if dimensions of a residual volume which was a volume in the puffer cylinder at the open position were designed properly. Due to its simple structure and smaller space, it was concluded that 1vol-1pis had advantages for the targets from the viewpoints of performance and simplicity.

3.2 Configuration of the interruption chambers and their performance

3.2.1 2vol-2pis-type interruption chamber

Figure 3.1 shows the configuration and operation of the 2vol-2pis. Two puffer chambers are connected in series, and each chamber has a piston to compress gas inside. The first volume Vol_1 in Fig. 3.1 is connected to the area where arcs ignite, and hot gas flows into Vol_1 and raise the gas pressure in large current interruption. The second volume Vol_2 is connected to Vol_1 through a relief valve, and gas is compress in Vol_2 and is supplied to Vol_1 when the pressure in Vol_2 is higher than that in Vol_1. The Vol_2 has a relief valve to relief gas to prevent unnecessarily high pressure in Vol_2.

The interruption chamber is operated as follows.

(i) In initial period of opening shown in Fig. 3.1(b), a valve (Val_{12}), which is installed between a thermal expansion volume (Vol_1) and a compression volume (Vol_2), is opened by the opening acceleration. Gas in the Vol_2 is compressed and its pressure gradually rises, then the gas is supplied from Vol_2 to Vol_1, and it increases the gas density of Vol_1.

(ii) As shown in Fig. 3.1(c), pressure of Vol_1 is raised by the inflow of hot gas of which density is low from a high current arc. It is also raised by a small piston which compresses Vol_1. During this period, $Val1_2$ is closed, because the pressure of Vol_1 is higher than that of Vol_2.

(iii) From the intermediate period to interruption stage shown in Fig. 3.1(c) and (d), gas is exhausted from grooves in the wall of Vol_2. This prevents an excessive pressure rise in

Vol_2. At the end of the interruption stage, the grooves are closed.

(iv) By the open position shown in Fig. 3.1(e), gas in Vol_2 is compressed and sent to Vol_1 of residual volume amount A_1. This makes recovery of the density in Vol_1 quick, and prepares for auto re-closing and opening operations.

In the 2vol-2pis, a small piston provides compression for Vol_1 and the pressure in Vol_2 is kept lower. This reduces resistance to the opening operation.

3.2.2 1vol-1pis-type interruption chamber

In the 2vol-2pis of Fig. 3.1, the pressure rises in Vol_1 consists of thermal one caused by the arc heat and a compressive one caused by small piston of cross-sectional area S_{p1}. The pressure-raised gas is stored in a residual volume amount A which is a relatively large volume amount at the end of the opening operation. Such a pressure rise effect might be obtained even in the 1vol-1pis. Figure 3.2 shows 1vol-1pis chamber, which is obtained by removing Vol_2 from the interruption chamber in Fig. 3.1. The basic structure of a puffer cylinder is same as the Hybrid-Puffer^{TM}-type one, as follows.

(a) It has a piston to compresses Vol. Diameter of the piston is the same or smaller than that of cylinder.

(b) It has the appropriate amount of residual volume amount A in Vol at the end of the opening operation.

The operation in high current interruption is as follows.

(i) As shown in Fig. 3.2 (b), the pressure in Vol is raised by the thermal effect of the arc and the compressive effect of a piston.

(ii) The high pressure is kept from short arcing time to long arcing time, because of the appropriate A in Vol.

The 2vol-2pis in Fig. 3.1 consumes energy in Vol_2, because of the gas compression in Vol_2, which does not contribute to interruption directly. On the other hand, the 1vol-1pis in Fig. 3.2

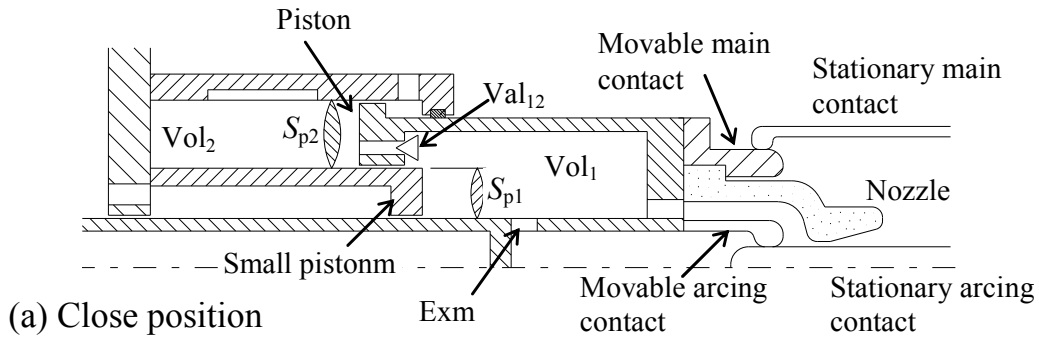

(a) Close position

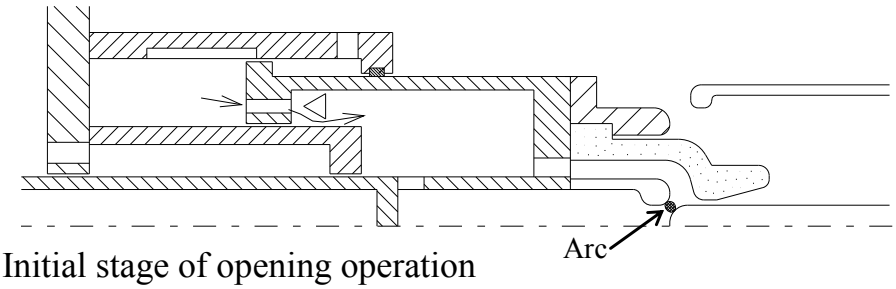

(b) Initial stage of opening operation

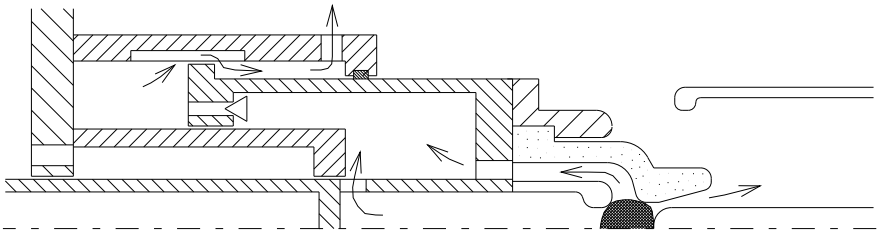

(c) Thermal expansion stage

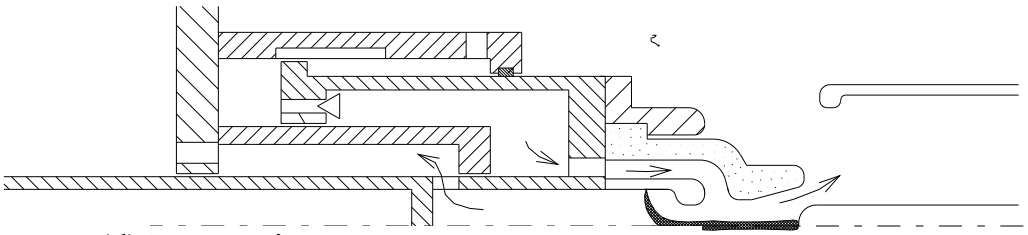

(d) Interruption stage

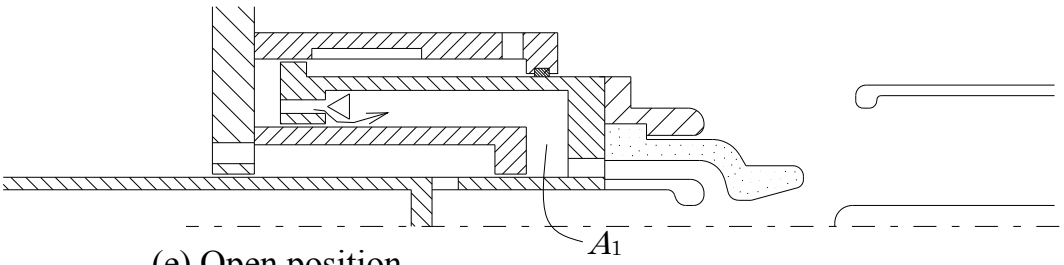

(e) Open position

Figure 3.1 2vol-2pis interruption chamber

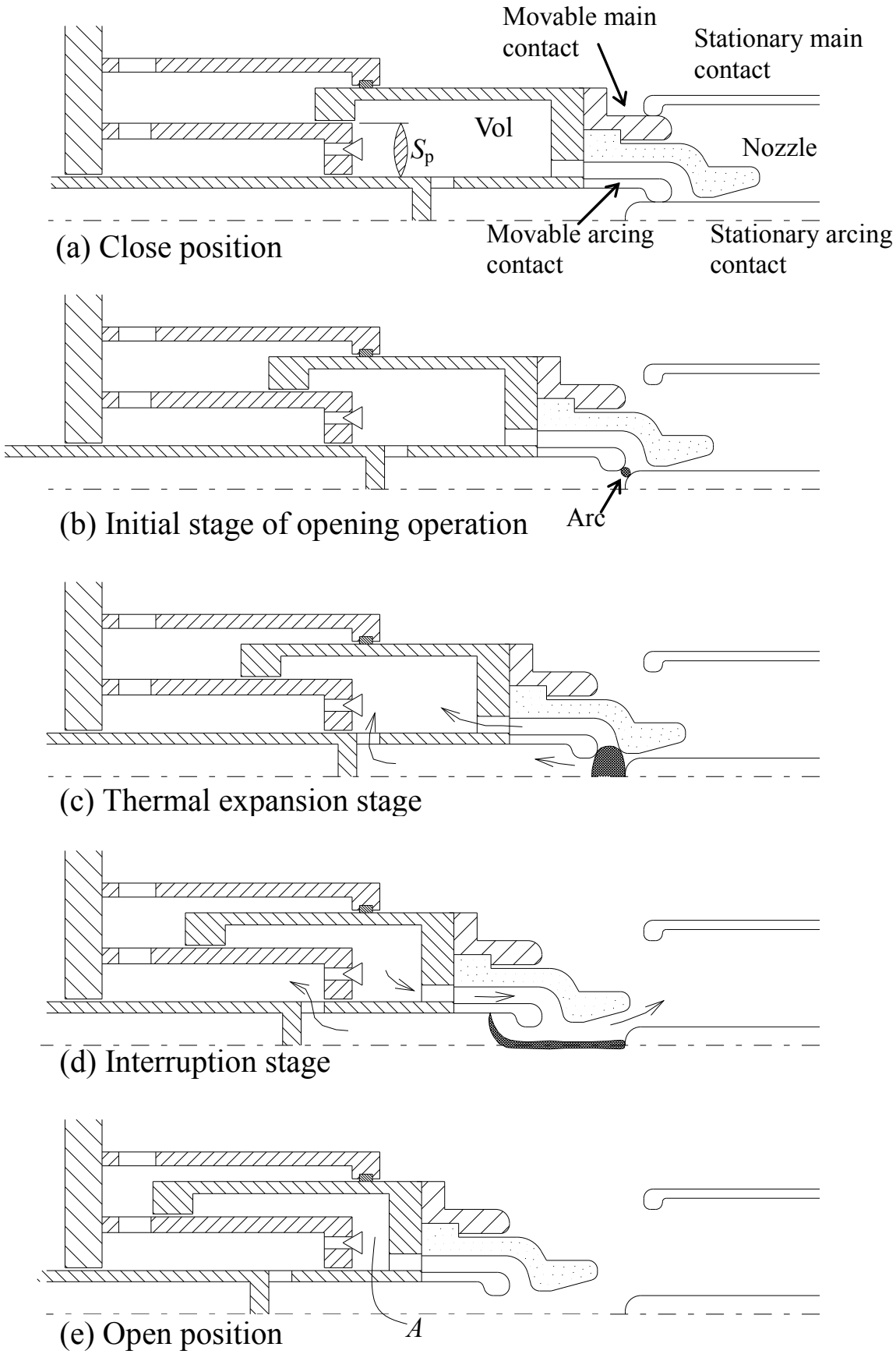

Figure 3.2 1vol-1pis interruption chamber

can use all of the energy in Vol, which contributes to interruption, though repulsive force on the piston can be large due to high pressure in the Vol.

3.3 Simulation method

3.3.1 Basic equations for simulations of pressure rise and opening travel

The basic equations for the case of 2vol-2pis (Fig. 3.1) was established first, then calculation for 1vol-1pis (Fig. 3.2) was carried out by changing input data.

In Fig. 3.1, gas density ρ_1 at Vol_1 in opening is expressed as Eq. (3.1) [1],

$$\rho_1(t+\Delta t) = \frac{\rho_1(t)\ell_1(t)S_{p1} - (q(t) - q_{21}(t))\Delta t}{S_{p1}(\ell_1(t) - \Delta x(t))} \quad , \tag{3.1}$$

where,

S_{p1} : cross-sectional area of piston for Vol_1,

ℓ_1 : equivalent length of Vol_1 for S_{p1},

q : outflow gas quantity from a nozzle per unit time,

q_{21} : inflow gas quantity from Vol_2 into Vol_1,

t, Δt : time and small time step, respectively,

$\Delta x(t)$: travel distance between time t and $t+\Delta t$.

The ℓ_1 in the Eq. (3.1) is equivalently obtained from Eq. (3.2),

$$\ell_1(t) = \frac{A_1 + S_{p1} \cdot \ell_L(t)}{S_{p1}} \quad , \tag{3.2}$$

where, $\ell_L(t)$ is actual length of area in front of S_{p1} in Vol_1 at time *t*.

$\Delta x(t)$ in the Eq. (3.1) is obtained from Eqs. (3.3) and (3.4),

$$\Delta x(t) = v(t) \cdot \Delta t \quad , \tag{3.3}$$

$$\frac{v(t+\Delta t)-v(t)}{\Delta t}=\frac{\sum F}{m}\cong\frac{F_{\mathrm{D}}-F_{\mathrm{R}}-F_{\mathrm{F}}}{m}, \tag{3.4}$$

where,

$v(t)$: velocity of movable parts at time t,

F_{D} : operating force,

F_{R} : repulsive force by increasing p_1 and p_2,

F_{F} : friction force,

m : mass of movable parts.

Then travel X is obtained by Eq. (3.5),

$$X=\sum\Delta x(t). \tag{3.5}$$

Considering the change of enthalpy h_1 per unit weight of the gas (it is called enthalpy in this chapter) caused by the inflow of hot gas from arc and cold gas from Vol_2, pressure in Vol1 (p_1) is obtained by Eq. (3.6) [1],

$$p_1\cong p_{10}\left(\frac{\rho_1}{\rho_{10}}\right)^{\gamma_c}\cdot\frac{h_1}{h_{10}}, \tag{3.6}$$

where,

γ_c : specific heat ratio of the gas,

p_{10}, ρ_{10} : initial values of the gas pressure (filling pressure) and the density in Vol_1,

h_{10} : initial value of the enthalpy in Vol_1.

Gas density ρ_2 and pressure p_2 in Vol_2 are expressed by similar equations,

$$\rho_2(t+\Delta t)=\frac{\rho_2(t)\ell_2(t)S_{\mathrm{p2}}-(q_{21}(t)+q_{2\mathrm{f}}(t))\Delta t}{S_{\mathrm{p2}}(\ell_2(t)-\Delta x(t))}, \tag{3.7}$$

$$p_2\cong p_{20}\left(\frac{\rho_2}{\rho_{20}}\right)^{\gamma_c}\cdot\frac{h_2}{h_{20}}, \tag{3.8}$$

where,

S_{p2} : cross-sectional area of piston for Vol_2,

ℓ_2 : length of Vol_2 for S_{p2},

p_{20}, ρ_{20} : initial values of the gas pressure (filling pressure) and the density in Vol_2,

h_2, h_{20} : enthalpy in Vol_2 and it's initial value,

q_{2f} : outflow quantity from Vol_2 to space in a gas tank on filling pressure (= p_{10}, p_{20}).

3.3.2 Arc modelling and gas quantity calculations

A variable q in the Eq. (3.1) is the sum of the hot gas-flow quantity by the arc and cold gas-flow quantity around the arc. A macro-model of an arc in a nozzle is required to obtain value of q.

Figure 3.3 presents an arc model for the calculation, where definitions of symbols used in the model are listed. As with Hermann's paper [2], it is assumed that there are three layers in the flow. The first layer (i) is the arc core, in which current flows with a parabolic temperature distribution. The second layer (ii) is surrounding the first layer with an exponential temperature distribution, and the third layer (iii) is the outer area containing cold gas. Boundary temperature between (i) and (ii), T_1, is set to 4000 K. The boundary

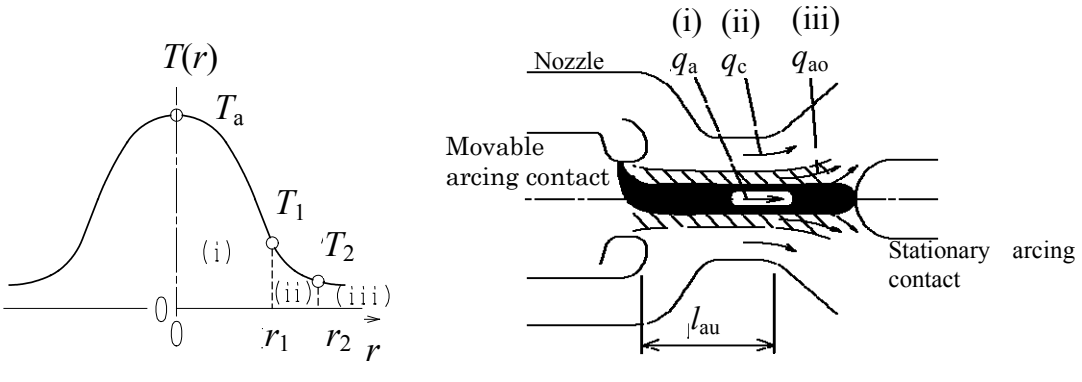

Figure 3.3 Modelling of arc

temperature between (ii) and (iii), T_2, is set to 1000 K. The temperature of arc core centre, T_a, is estimated as 20000-25000 K in general [3][4]. In this thesis, it is set to 20000 K. The average temperature T_{ave} in arc core area with parabolic distribution of Eq. (3.9) is obtained by Eq. (3.10),

$$T = T_a - (T_a - T_1)\frac{r^2}{r_1^2}, \tag{3.9}$$

$$T_{ave} = \frac{\int_0^{r_1} T(r)\cdot 2\pi r \cdot dr}{\pi r_1^2} = \frac{T_a + T_1}{2} = 12000\,\mathrm{K}. \tag{3.10}$$

Conversely, for layer (ii), when the temperature distribution is simplified and is approximated to be linear, the average temperature is obtained as 2000 K in the case of r_1=0 and 2500 K in the case of $r_1 >> r_2 - r_1$. Then 2300 K is used as average temperature in the area (ii). Using symbols q_a, q_{ao}, and q_c, for each gas-flow mass of (i), (ii), and (iii), q in (3.1) is represented as Eq. (3.11),

$$q = q_a + q_{ao} + q_c. \tag{3.11}$$

It is assumed that thermal energy is supplied from (i) to (ii) by thermal conduction, and it balances with thermal flow mass q_{ao} at the nozzle throat. Thermal mass Q_{rT_1} per unit time from (i) to (ii) by thermal conduction represented by Eq. (3.12) [2],

$$Q_{rT_1} = \kappa_1 \left(\frac{dT}{dr}\right)_{T_1} \cdot 2\pi r_1 \ell_{au}, \tag{3.12}$$

where,

κ_1 : thermal conductivity at T_1,

ℓ_{au} : arc length at upstream from nozzle throat.

The dT/dr in the Eq. (3.12) is obtained by differentiating the Eq. (3.10) as Eq. (3.13), and dT/dr at T_1 as Eq. (3.14) [2],

$$\frac{\mathrm{d}T}{\mathrm{d}r} = -2(T_{\mathrm{a}} - T_{1})\frac{r}{{r_1}^2}, \tag{3.13}$$

$$\left(\frac{\mathrm{d}T}{\mathrm{d}r}\right)_{T_1} = -32000\frac{1}{r_1}. \tag{3.14}$$

Here, Q_{rT_1} is approximately 50000 W/m using thermal conductivity in Frost's paper [5]. Conversely, arc power per unit length is 6000 kW/m, even in the case of current 1 kA with arc voltage 6000 V/m for the conventional value of a GCB. This means that the thermal flow in layer (ii) is much less than that in layer (i). From Frost's paper, each thermal mass ($h\rho_1 a$) per unit of cross-sectional area per unit pressure at a sonic flow in layer (i) of 12000 K and layer (ii) of 2300 K are 1.651×10^7 and 1.157×10^7(J/(s·m^2)), which are similar values. Therefore, it can be considered that the cross sectional area of (ii) is also negligible compare to (i).

From these results, q_{ao}=0 is assumed, which means all of the arc energy remains in the arc column area (i).

Here, q_{a} and q_{c} in the Eq. (3.11) become as follows:

$$q_{\mathrm{a}} = p_{\mathrm{t}}\ \rho_{\mathrm{a1}}\ S_{\mathrm{a}}\ a_{\mathrm{a}}\ M_{\mathrm{a}}, \tag{3.15}$$

$$q_{\mathrm{c}} = p_{\mathrm{t}}\ \rho_{\mathrm{c1}}(S_{\mathrm{N}} - S_{\mathrm{a}})\ a_{\mathrm{c}}\ M_{\mathrm{c}}, \tag{3.16}$$

where,

p_{t} : pressure at nozzle throat,

ρ_{a1}, ρ_{c1} : density per unit pressure at nozzle throat in (i) and (iii),

S_{a}, S_{N} : cross-sectional area of arc and nozzle throat,

a_{a}, a_{c} : sonic speed in (i) and (iii),

M_{a}, M_{c} : mach number in (i) and (iii).

The values ρ_{a1} and a_{a} are set at the average temperature in (i). The value p_{t} is obtained under sub-sonic or sonic condition on upstream pressure p_1 and downstream pressure p_{10} [1].

The value M_a and M_c are obtained by Eq. (3.17) [1] and by setting γ_a to a value at temperature in Vol1, respectively,

$$M_a = \sqrt{\frac{2}{\gamma_a + 1}\left[\left(\frac{p_t}{p_1}\right)^{\frac{1-\gamma_a}{\gamma_a}} - 1\right]}. \tag{3.17}$$

An equation of energy balance is Eq. (3.18) [1],

$$i_a V_{au} = h_a q_a \ , \tag{3.18}$$

where,

$V_{au} = E_{a1} \ell_{au}$ or $V_{au} = E_{a2} \ell_{au}$,

and,

i_a : interrupting current,

V_{au} : arc voltage at upstream to nozzle throat,

E_{a1} : arc voltage per unit length before nozzle open,

E_{a2} : arc voltage per unit length after nozzle open,

h_a : average enthalpy in (i).

By substituting a right side of the Eq. (3.15) into q_a of the Eq. (3.18), S_a can be obtained as Eq. (3.19),

$$S_a = \frac{i_a V_{au}}{h_a p_t \rho_{a1} a_a M_a}. \tag{3.19}$$

Gas-flow mass through a channel between Vol_1 and Vol_2, q_{21} , is obtained by Eqs. (3.16) and (3.17). In calculating q_{21}, cross sectional area of the channel, and pressure and density at the channel are used instead of "$S_N - S_a$", p_t and ρ_{c1}, respectively. Additionally, γ_a is set to the value at the temperature in Vol_2. In this event upstream and downstream pressures are p_2 and p_1 respectively. And q_{2f} is obtained by similar procedure using the cross sectional area of grooves, p_2 and p_{20} (or p_{10}), where p_2 is set as upstream pressure, and

p_{20} is set as downstream pressure. Quantities q_{21} and q_{2f} can be obtained without considering the arc effect.

As other composition, even in the case that Vol_2 has some relief valves [6] to exhaust an excessive gas pressure, q_{2f} can be calculated by same procedure.

3.3.3 Modelling expansion and contraction of hot gas during nozzle clogging

When a current increases, the hot gas expands upstream during arc clogging. It is assumed that current does not flow in this hot gas part, and temperature of the hot gas is T_1 (4000 K) in Fig. 3.3. The value of the generated hot gas volume is determined by the temperature T_1 and the arc energy that is not exhausted from a nozzle throat. When the hot gas reaches a puffer cylinder, it causes an enthalpy increase [1]. In the process of the current decreasing, the diameter of the arc becomes smaller than that of the nozzle throat. Then there are a hot gas-flow surrounding arc and a cold gas-flow outside the hot gas-flow, which is the same situation as shown in Fig. 3.3. In this case, the mass-flow q is represented as Eq. (3.20) by changing q_{ao} into q_h in the Eq. (3.11),

$$q = q_a + q_h + q_c . \tag{3.20}$$

The hot gas-flow mass q_h is calculated from various values including the cross-sectional area and the density corresponding to T_1.

3.3.4 Simulation conditions

3.3.4.1 Parameters

Table 3.1 shows parameters for simulation mentioned above.

3.3.4.2 Interruption duties

The object of development was a GCB of 252/245-kV 50-kA 50-Hz /40-kA 60-Hz for gas insulated switchgears (GIS). GCBs are required to satisfy many kinds of interrupting

Table 3.1 Values of calculation parameters

p_{10}, p_{20}	0.65	γ_c	1.09
ρ_{10}, ρ_{20}	40.0	γ_a	1.64
ρ_{c1}	6.15	h_{c1}, h_{10}, h_{20}	1.91×10^5
ρ_{a1}	0.01883[9]	h_{a1}	3.251×10^7[9]
a_c	134	S_N	5.31×10^{-4}
a_a	2592 [9]	E_{a1}	3500
		E_{a2}	6000

Units : p: MPa-a, ρ : kg/m^3, a: m/s, h: J/kg, S: m^2, E:V/m

performance. In particular, SLF90% (L90) and breaker-terminal fault (BTF) with 100% asymmetric current (T100a) interruptions are related to the pressure rise characteristics in a puffer cylinder and the travel characteristics during opening operations. Therefore, the next two items were considered as required conditions for the structure of the interruption chamber to interrupt a large current.

(a) To interrupt L90 for 40-kA 60-Hz successfully, a sufficiently high pressure rise must be obtained at current zero. This is selected because di/dt for 40-kA 60-Hz has almost same value and pressure rise is lower due to less arc energy taken into the puffer chamber compared to L90 interruption for 50-kA 50-Hz.

(b) To interrupt 50-kA 50-Hz T100a successfully, the pressure rise at current zero is sufficiently high and travel characteristics are sufficiently. This is selected because this current generates the largest arc energy and leads to the highest-pressure rise.

3.3.4.3 Operating conditions

Simulation was carried out for a hydraulic mechanism whose pressure in an accumulator was set to the lock out condition (19 MPa-a, corresponding to 1.5 kJ of energy).

In this calculation, operating energy that actually works to a hydraulic piston is influenced by the loads which are diameter of the puffer piston and interruption current, etc. Higher opening speed due to lighter load causes higher hydraulic pressure drops in piping part, then the operating energy is calculated smaller than that on heavier load. Opening characteristics

for typical interruption (L90, T100a) and no load open were calculated in two interruption chambers.

3.4 Simulation results

3.4.1 2vol-2pis-type interruption chamber

Figure 3.4 shows an example of calculated travel and pressure characteristics of a 2vol-2pis for an interrupting current of 36 kA with DC component 8 %, corresponding to current of

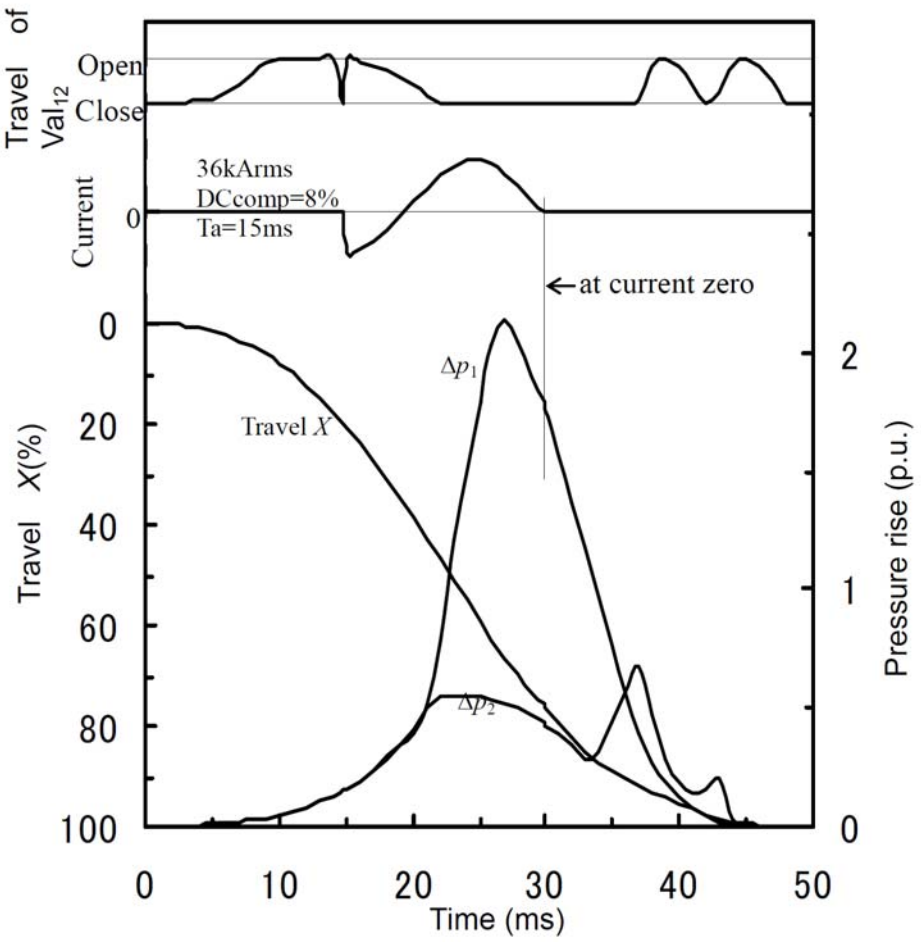

Figure 3.4 Simulation example of opening characteristics in 2vol-2pis chamber (I=36kA, DC component 8 %, T_a=15 ms)

90 % of rated current 40 kA. In this calculation, S_{p1} was set to a same value S_p=1.0 p.u. (0.00672 m^2) in a 1vol-1pis simulation, which will be shown later. In figures after Fig. 3.4, 1.0 p.u. of Δp was corresponding to 0.65 MPa-a, which was the filling SF_6 gas pressure. Pressure rise Δp_1 in Vol_1 became large effectively. Conversely, pressure rise Δp_2 in Vol_2 remained at a low value and became large value again at the end of travel. The Val_{12} opened during the initial period of travel due to acceleration of the opening operation and closed during the intermediate period in which pressure in the Vol_1 became high. Then the Val_{12} opened at the end of the period in which pressure in the Vol_1 decreased. These show that the interruption chamber can work as described in section 3.2.1. In this case, the operating energy calculated in Fig. 3.4 was 1610 J.

With a value of 1.0 p.u. for S_{p1}, simulations were carried out while changing arcing time for several values for S_{p2}. The mass of the movable part and the conditions of the hydraulic driving mechanism were fixed in the simulations. Figure 3.5 shows pressure rises in Vol_1 at current zero with parameter S_{p2}. As stated before, the case of S_{p2}=0 corresponds to 1vol-1pis in Fig. 3.2. In Fig. 3.5, nozzle opening time is represented as a circle on each curve. The nozzle opening time means the time in which a nozzle throat passes a tip of a stationary arcing contact and the nozzle throat opens efficiently. It is considered that L90 can be interrupted only after the nozzle opening time even with sufficient pressure rise. The figure shows that pressure rise Δp_1 does not change much corresponding to S_{p2} for short arcing time interruptions.

Corresponding to an increase in S_{p2}, a Δp_1 tended to decrease for middle arcing time and to increase for long arcing time. The opening speed of this interruption chamber decreased with an increase in S_{p2}, because of repulsive force on the piston. For short arcing time interruptions, the differences of Δp_1 among various S_{p2} were small, because the influence of a decrease in opening speed was small. For intermediate arcing time interruptions, Δp_1 became lower in the case of large S_{p2}, because the influence of a decrease in opening speed

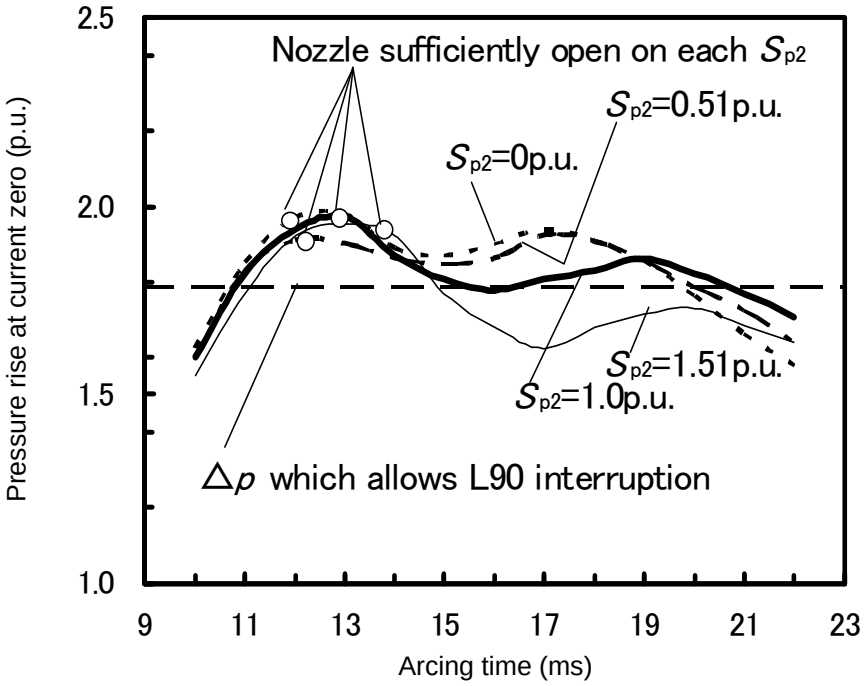

Figure 3.5 Pressure rise at current zero to be interrupted in Vol_1 of 2vol-2pis chamber with parameter S_{p2} and constant value of 1.0 p.u. for S_{p1} (I=36kA)

became strong. For long arcing time above 19 ms, Δp_1 was maintained at a relatively high value, because the inflow from Vol_2 into Vol_1 affected maintaining the density in Vol_1. Being able to obtain a high pressure rise for a long arcing time interruption with a proper value of S_{p2} is a feature of 2vol-2pis. However, the pressure rise from nozzle opening to arcing time of 19 ms is highest in the case of S_{p2}=0. This is because there is no repulsive force on S_{p2} and the increase in opening speed affects pressure.

The pressure rise required to interrupt 40-kA 60-Hz L90 successfully is represented by dashed line in Fig. 3.5. It is also required that a nozzle should be opened sufficiently to interrupt such a large current. The nozzle opening time for each S_{p2} is also represented in Fig. 3.5. Duration of maintaining required pressure from the nozzle opening time is T_{iw} (time interruption window). For 60-Hz current, it is desirable that T_{iw} is larger than 8.3 ms. In Fig. 3.5, if S_{p2} is equal to S_{p1} (=1.0 p.u.) or smaller, T_{iw} is almost 8.3 ms that is a half

cycle. However, there are not enough space to install Val12 if S_{p2} is smaller than S_{p1}. A practical dimension is region of $S_{p2} > S_{p1}$, say $S_{p2}=1.5\ S_{p1}$, but this cannot obtain sufficient T_{iw}. Besides, the opening speed will decrease because of repulsive force on S_{p2}, even with no-load operation for $S_{p2}=1.5\,S_{p1}$.

Figure 3.6 shows the results of simulations under conditions of $S_{p2}=S_{p1}$ (=1.0 p.u.) with a parameter of the residual volume amount, A_1, in Vol1 at the end of the opening. In this figure, A_1 is represented by an equivalent length, L_{R1}, as Eq. (3.21),

$$L_{R1}=A_1/S_{p1}. \tag{3.21}$$

The value of 1.0 p.u. which means 10 mm is set for L_{R1} as smallest value to prevent the puffer cylinder colliding with the piston. Figure 3.6 shows that, in the case of a smaller L_{R1}, pressure rises for short arcing time interruptions become higher, but they become lower for longer arcing time interruptions. For a small Vol_1, the compression effect is strong for a shorter arcing time. However, the density in the small Vol_1 decreases for a longer arcing time

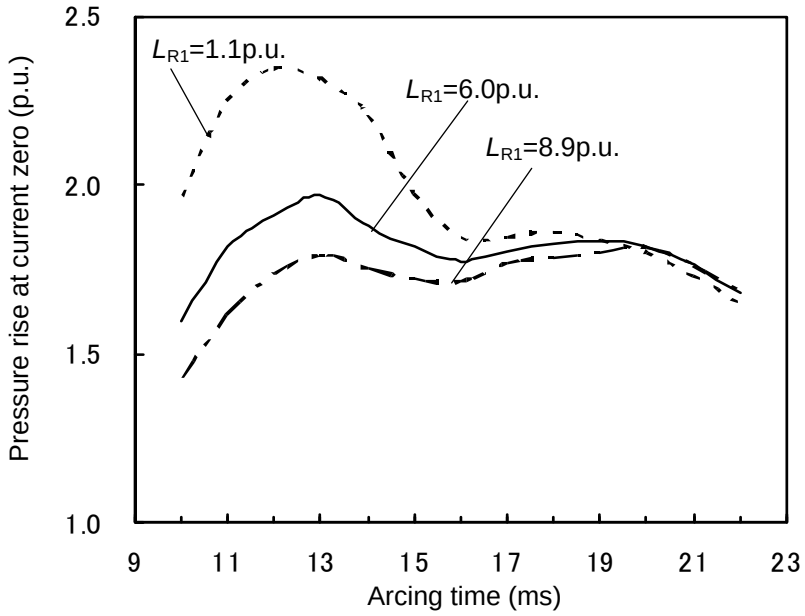

Figure 3.6 Pressure rise at current zero to be interrupted in Vol_1 of 2vol-2pis chamber with parameter L_{R1} for S_{p2}=S_{p1}=1.0 p.u. (I=36kA)

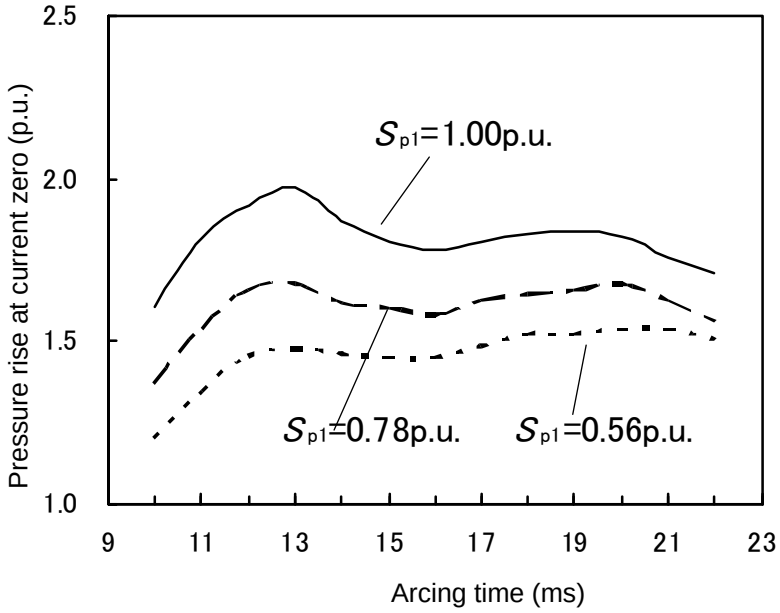

Figure 3.7 Pressure rise at current zero to be interrupted in Vol_1 of 2vol-2pis chamber with parameter S_{p1} for constant value of outer diameter of the chamber (I=36kA)

because the values of outflow mass during early periods becomes large and the opening speed becomes low due to larger repulsive force caused by a higher pressure.

Figure 3.7 shows that pressure in Vol_1 rises with parameter S_{p1}. In these simulations, the outer diameter was fixed, and $S_{p2} = S_{p1}$ in the case of S_{p1}=1.0 p.u.. This means that a smaller S_{p1} leads to a larger S_{p2} and a larger Vol_2. The figure shows that a larger S_{p1} increases pressure in Vol_1. This appears to be an effect of compression of Vol_1 caused by S_{p1}. This also means that this type of interruption chamber can obtain higher pressure than a conventional 2vol-1pis, which does not compress Vol_1.

3.4.2 1vol-1pis-type interruption chamber

In the case of 1vol-1pis, a higher pressure may be obtained when the cross-sectional area of the piston S_p is large enough compared to that of a nozzle throat, then it might interrupt 40-kA 60-Hz L90 easily. However, such a large S_p may cause high pressure and large

repulsive force on the piston in the case of 50-kA T100a interruption, and a large reverse of travel may occur. If the reverse of travel is too large and affects on interruption ability badly, the 1vol-1pis cannot be adapted and the 2vol-2pis should be selected. Therefore, S_p should be an appropriate value, which brings about a sufficient T_{iw} and does not cause a large reverse. To obtain such an appropriate S_p, simulations of opening operations were repeated and found one proper value as S_p =1.0 p.u. which means 0.00672 m^2.

Figure 3.8 shows calculated travel characteristics when interrupting 40-kA L90 with the same values A and hydraulic operating pressure in Fig. 3.4. In Fig. 3.8, pressure rise is much higher than that for no-load operation, which is the same as Fig. 3.4. Measured results are also shown in Fig. 3.8. Calculated results show a good agreement with them. This proves

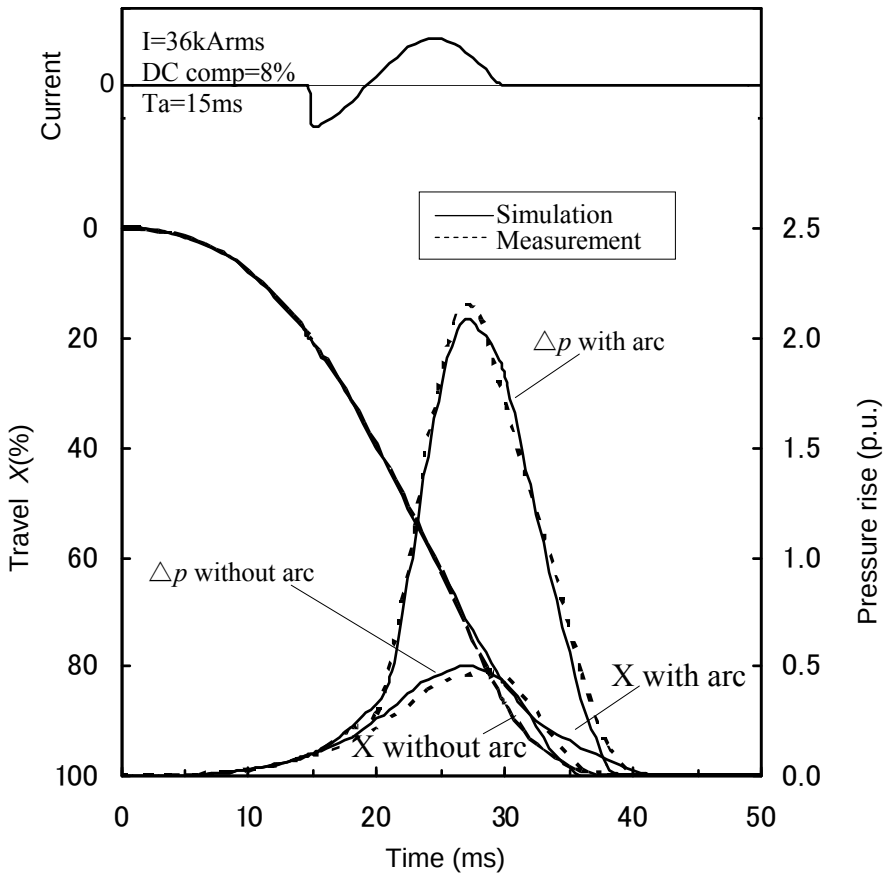

Figure 3.8 Comparison between simulation and measurements of opening characteristics in 1vol-1pis chamber (I=36kA, DC component 8 %, T_a=15 ms)

that the simulation methods are appropriate. In Fig. 3.8, operating energies calculated on no load open and L90 interruption are 1440 J and 1530 J respectively.

Figure 3.9 shows the results of simulations with the parameter of A, which is the residual volume amount (A) in the volume of puffer cylinder (Vol) at the end of the opening operation. As the same in Fig. 3.6, A is represented by equivalent length L_R, which is obtained by dividing A by S_p. Figure 3.9 shows that, in case A (or L_R) is 1.1 p.u., the pressure rise for a short arcing time interruption becomes higher, but it becomes lower for a longer arcing time interruption. When A is too small as 1.1 p.u., compression and heating effects are strong for a shorter arcing time. However, for a longer arcing time, the density in Vol becomes lower. This is because much gas in Vol flows out by high pressure in the Vol in the early periods of operation, and opening speed decreases due to repulsive force. When A is too large, the pressure rise decreases during any arcing time interruption due to a reduction of compression effect. For intermediate A (L_R=6.0 p.u.), the pressure rise has high and flat characteristics for

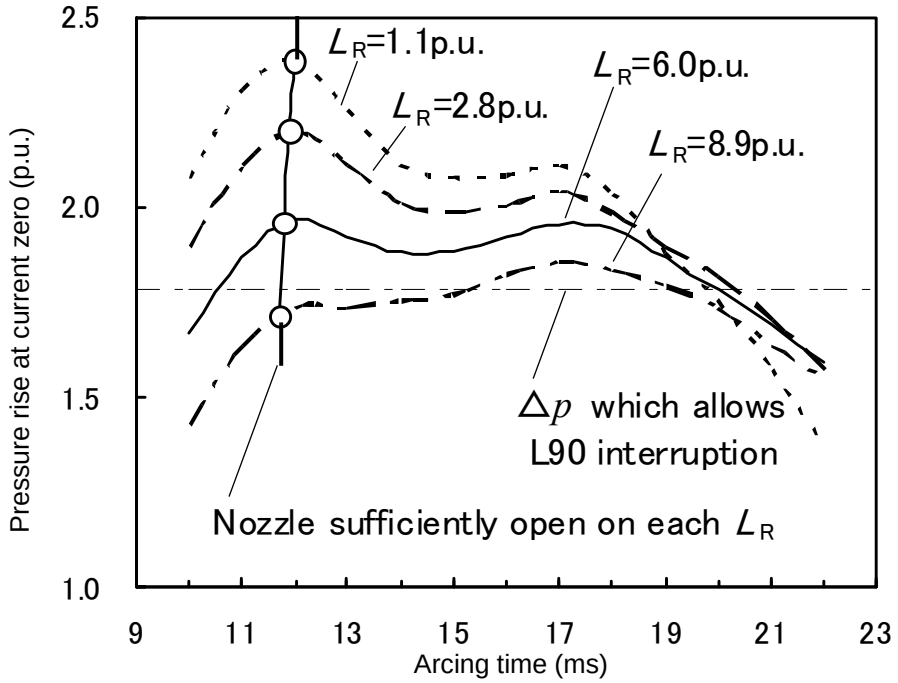

Figure 3.9 Pressure rise at current zero to be interrupted in 1vol-1pis chamber chamber
(I=36kA)

a wide range of arcing time interruptions.

Pressure rise characteristics at current zero against arcing time as shown in Fig. 3.9 were obtained for several S_p. Then Fig. 3.10 which showed the relations between L_R and T_{iw} with parameter S_p was obtained. In the case of $S_p < 0.9$ p.u., T_{iw} required was not achieved for any L_R. In the case of $S_p > 1.0$ p.u., the required value for T_{iw}, 8.3 ms, could be achieved. For example, T_{iw} could be larger than 8.3 ms for the appropriate intermediate value of L_R in case of S_p =1.0 p.u.

Figure 3.11 shows gas density in the puffer cylinder at current zero of 40-kA L90 for S_{p1} =1.0 p.u. The density in Vol1 of 2vol-2pis with values $S_{p2} = S_{p1}$ =1.0 p.u. is also shown in this figure. The density of 2vol-2pis is higher than that of 1vol-1pis in the regions of 12-13 ms and above 20 ms arcing time interruptions. This is because of the effects of the inflow from Vol_2 into Vol_1. Conversely, the density of 1vol-1pis is higher during the intermediate arcing time interruption. This is because of the effects of an increase of opening speed caused by a reduction of repulsive force on the piston. However, the difference is not significant.

3.5 Comparison of interruption chambers

As stated above, 2vol-2pis has the merit of keeping pressure rise high for a longer arcing time. However, comparing pressure during 8.3 ms from nozzle opening time, the pressure of 1vol-1pis was higher than that of 2vol-2pis, while there was not so much difference for gas density. Therefore, from the viewpoint of practical size and calculated consumption operating energy by same hydraulic mechanism (2vol-2pis in Fig. 3.4 : 1610 J, 1vol-1pis in Fig. 3.8 : 1530 J), 1vol-1pis was superior in terms of L90 interruption performance.

Moreover, a no-load opening speed of 1vol-1pis was a little faster than that of 2vol-2pis one, which gave advantages for capacitive current interruption. Therefore, it was concluded that 1vol-1pis was suitable for the target of the new GCB.

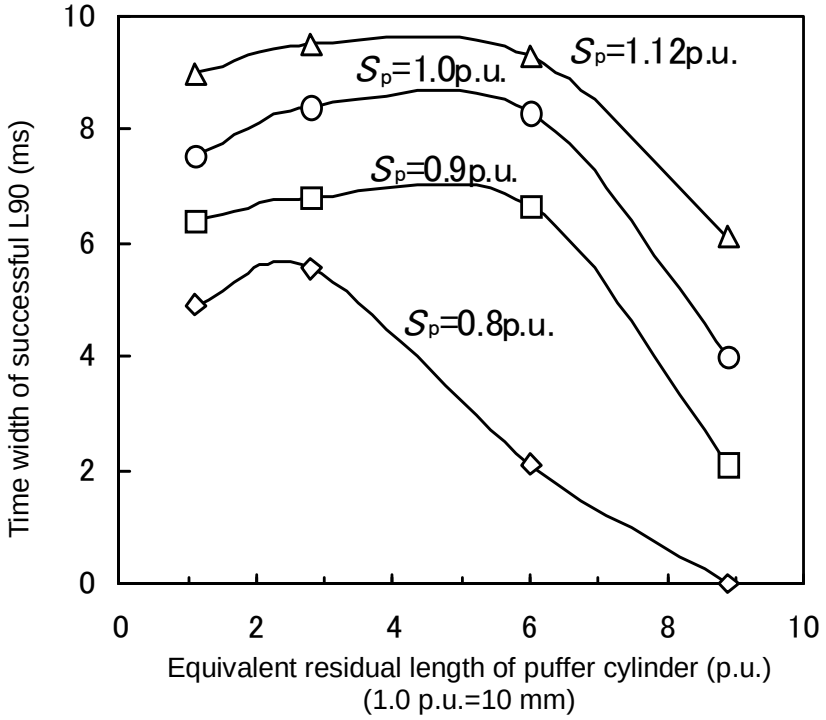

Figure 3.10 Time width of L90 successful interruption vs. L_R in 1vol-1pis chamber (I=36kA)

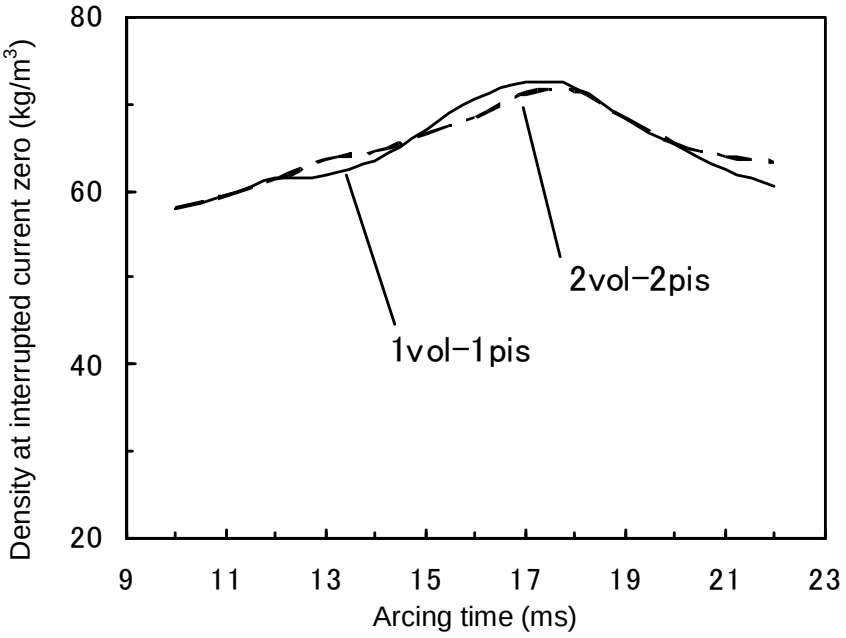

Figure 3.11 Density in puffer cylinder at current zero to be interrupted

3.6 Determining of dimensions of 1vol-1pis-type interruption chamber

From opening operation characteristics, as shown in previous chapters, the under limit of S_p and the rough value of L_R were determined. Adding simulations of 50 kA-T100a interruption, appropriate dimensions for the interruption chamber were selected.

When the interruption chamber interrupted 50-kA T100a at the longest arcing time ($T_{a\,max}$), the travel reached almost its end position and slowed down. Moreover, gas mass in a puffer cylinder was small at that time. Therefore, pressure in the puffer cylinder at current zero decreased remarkably. To obtain a required interruption performance, a higher pressure was desirable, even under such conditions.

Figure 3.12 shows pressure rise at current zero against L_R with a parameter of S_p. Larger S_p and L_R, that is larger residual volume amount, resulted in a higher-pressure rise. The area where sufficient interruption window (8.3 ms mentioned in Fig. 3.10) was obtained is shown

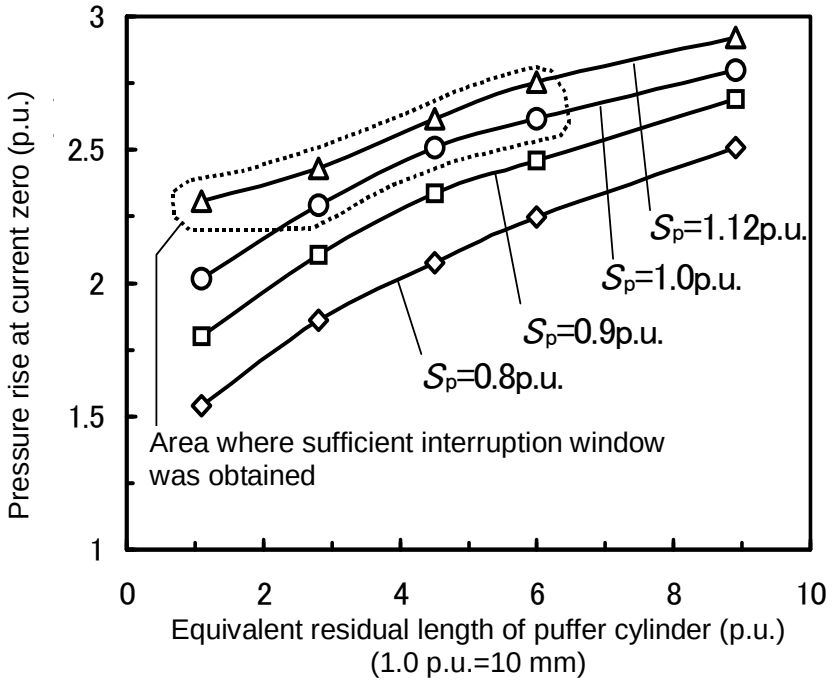

Figure 3.12 Pressure rise at current zero to be interrupted in 1vol-1pis chamber (*I*=50kA-asym, DCcomp.=50%, *T*a=23ms)

in Fig. 3.12. As mentioned before, if L_R was appropriate and S_p was equal to or greater than 1.0 p.u., 40-kA 60-Hz L90 could be interrupted successfully. Conversely, under these conditions, a 14 % travel reverse from 66 % position of all travel appeared due to repulsive force in the case of S_p =1.12 p.u., L_R=4.5 p.u., T_a =16 ms. It was considered that S_p =1.12 p.u. was not preferable due to this characteristic. In the case of S_p =1.0 p.u. L_R=6.0 p.u., no reverse travel occurred at any arcing time. A higher pressure at current zero was preferable even in the case of a T100a interruption.

Therefore, the dimensions of S_p =1.0 p.u. and L_R=6.0 p.u. were selected, which could obtain a high pressure for interrupting a 50 kA-T100a and could interrupt 40-kA 60-Hz L90 successfully. In the case of S_p =1.0 p.u. and L_R=6.0, operating energy calculated in the longest arcing time (23 ms) was 1560 J which was only 2 % higher than that of 40-kA L90 interruption.

3.7 Conclusions

On the purpose of developing 245-kV 50-kA 50-Hz / 40-kA 60-Hz GCB with operating mechanism of 1.5 kJ, two types of interruption chamber of GCBs were compared from viewpoints of opening characteristics. One was two volumes-two pistons-type interruption chamber (2vol-2pis) and the other was one volume-one piston-type interruption chamber (1vol-1pis). To carry out the investigation, one-dimensional simulation of puffer pressure and travel characteristics was extended to these type GCBs.

(a) It was confirmed that an efficient pressure rise for L90 interruption, which had advantages in reducing operating energy, was obtained with both of them.

(b) It was also confirmed that both of them did not indicate unusual travel characteristics by repulsive force on puffer piston even in interrupting 50 kA.

(c) As the results, 1vol-1pis was selected for a further investigation as a new product, because its structure is simpler than that of 2vol-2pis.

The 1vol-1pis chambers are much smaller than the Hybrid-puffer^{TM}-type developed in the Chapter 2, but basic structure is similar. Therefore, it is named as "advanced Hybrid-puffer^{TM}-type chambers". The advanced Hybrid-puffer^{TM}-type chamber features small diameter of puffer piston and small volume of puffer chamber. The puffer pressure can rise easily by hot gas, because of the small volume of the puffer chamber. At the same time, although high pressure is generated in the puffer chamber, repulsive force is not so large, because the diameter of the piston is small.

References

[1] S.Yanabu, H.Mizoguchi, and M.Toyoda: "Development of novel hybrid interrupting chamber for gas circuit breaker utilizing self-pressure-rise phenomena by arc", *IEEE Trans. on PWRD*, Vol.4, No.1, 1989, pp355-361

[2] W.Hermann and K.Ragaller: "Theoretical description of the current interruption in HV gas blast breaker", *IEEE Trans. on PAS*, Vol.PAS-96, No.5, 1977, PP1564-1551

[3] W.Herts, H.Motschmann, and H.Wittel: "Investigation of the properties of SF_6 as an arc quenching medium", *Proc. of the IEEE*, Vol.59, No. 4, 1971, pp485-492

[4] M.Murano, H.Nishikawa, A.Kobayashi, and T.Iwamoto: "Heavy current clogging phenomena in SF_6 gas arc", *IEEE PES*, C74, 185-5, 1974

[5] L.S.Frost and R.W.Liebermann: "Composition and transport properties of SF_6 and their use in a simplified enthalpy flow arc model", *Proc. IEEE*, Vol.59, 1971, pp464-485

[6] W.Hofbauer and J.Stechbarth: "Strategic tools-application for the development of a 300kV/50kA GIS self-blast circuit breaker", *CIGRE*, SC13-110, August 1994

Chapter 4 Improvement of Gas-flow Simulation for Advanced Hybrid-puffer^{TM}-type GCB

4.1 Introduction

The advanced Hybrid-puffer^{TM}-type chamber was concluded to be suitable for the new 245-kV gas circuit breaker (GCB) in Chapter 3. To design the configurations of the chambers including nozzles or exhaust cylinders, hot-gas-flow simulation is one of important engineering tools [1][2]. Therefore, hot-gas-flow simulation was tried to adapt to the advanced Hybrid-puffer^{TM}-type chamber.

However, it was found that simulations by the conventional method which had been developed for Hybrid-puffer^{TM}-type GCBs had not given proper values for the advanced Hybrid-puffer^{TM}. To improve the simulation, gas properties and modelling of contacts moving were investigated in this chapter.

In many gas-flow simulations, the some properties of SF_6 gas have been taken into account. In particular, gas properties such as gas constant and thermal conductivity do not indicate linear characteristics against temperature and pressure under high temperature conditions. Such characteristics were calculated by some researchers [3]-[5] providing gas transport characteristics up to 30000 K and 1.57 MPa (16 atm in the literatures). These data have been referred to by many researchers because of their availability [6]-[8]. However, the gas pressure in some GCBs sometimes becomes higher than 1.57 MPa, especially in the arc region and its surrounding area. This area is the most important region for gas simulations of GCBs, and thus, data up to 1.57 MPa is sometimes not enough to cover real gas pressure. Gas transport characteristics under high temperatures and high pressures up to 10 MP were calculated before gas-flow simulation in this chapter.

In many simulations of puffer-type GCBs, stationary arcing contacts are moved [1][2][6]-[8], and alternative methods have been applied [9]. These methods can simplify the simulations and make them practical, because figures of movable parts of GCBs are generally complex. However, there may be some errors with stationary parts moving under some simulation conditions. In this chapter, two different methods, movable parts moving method and stationary parts moving method, were evaluated, and it is discussed that which parts should be moved in gas-flow simulations.

4.2 Thermodynamic and transport properties of SF_6 gas

Historically, the thermodynamic and transport properties of SF_6 gas at a gas pressure below 1.57 MPa were referred to in the literature [4], but the pressure in the advanced Hybrid-puffer^{TM}-type circuit breakers could reach 5 MPa. The advanced Hybrid-puffer^{TM}-type circuit breakers feature hot gas, and simulations require more precise and detailed considerations of the thermal properties of the gas. Therefore, the thermodynamic and transport properties of SF_6 gas for regions of up to 10 MPa and 30000 K were obtained and adopted for the simulation in this chapter. Outline of calculation methods has been shown in Section 1.6.3.2.

Basic equations relating dissociation and ionise reaction between these particles were solved by the Newton-Raphson method. Figure 4.1 shows an example of the equilibrium composition of SF_6 gas at a pressure of 2 MPa and a temperature up to 30000 K.

By using derived gas compositions which consisted of the related molecules, atoms, ions, and electrons, the thermodynamic, and transport properties in high temperature SF_6 gas were obtained for high pressures up to 10 MPa.

Figures 4.2 to 4.6 show the calculation results for gas constant R, enthalpy h, specific heat ratio γ, electrical conductivity σ, and thermal conductivity κ, respectively. Each figure contains the lines for pressures 0.5, 1.0, 2.0, 5.0, and 10.0 MPa. Some lines at 1 MPa were

compared with the ones by Chervy et al. [5] in Table 4.1. The values derived in this section approximately agree with Chervy et al., which confirm the validity of the calculations.

4.3 Treatment of moving part in gas-flow simulation for GCBs

The modified fluid-in-cell (FLIC) method which had been developed for GCBs [1] is used in this thesis. Figure 4.7 shows an example of cells used for the simulation by the modified FLIC. The hot-gas-flow simulation was carried out for large area in a dead-tank -type GCB including tank walls. The chamber simulated was the advanced Hybrid-puffer^{TM}-type [10][11]. As explained in Chapter 3, basic configuration of this type of chamber is same as that of the Hybrid-puffer^{TM}-type shown in Fig. 1.4.

In reality, a movable part including a puffer cylinder, movable arcing contacts, a movable main contact, and nozzles, moves with the operating rod, and compresses gas in the puffer

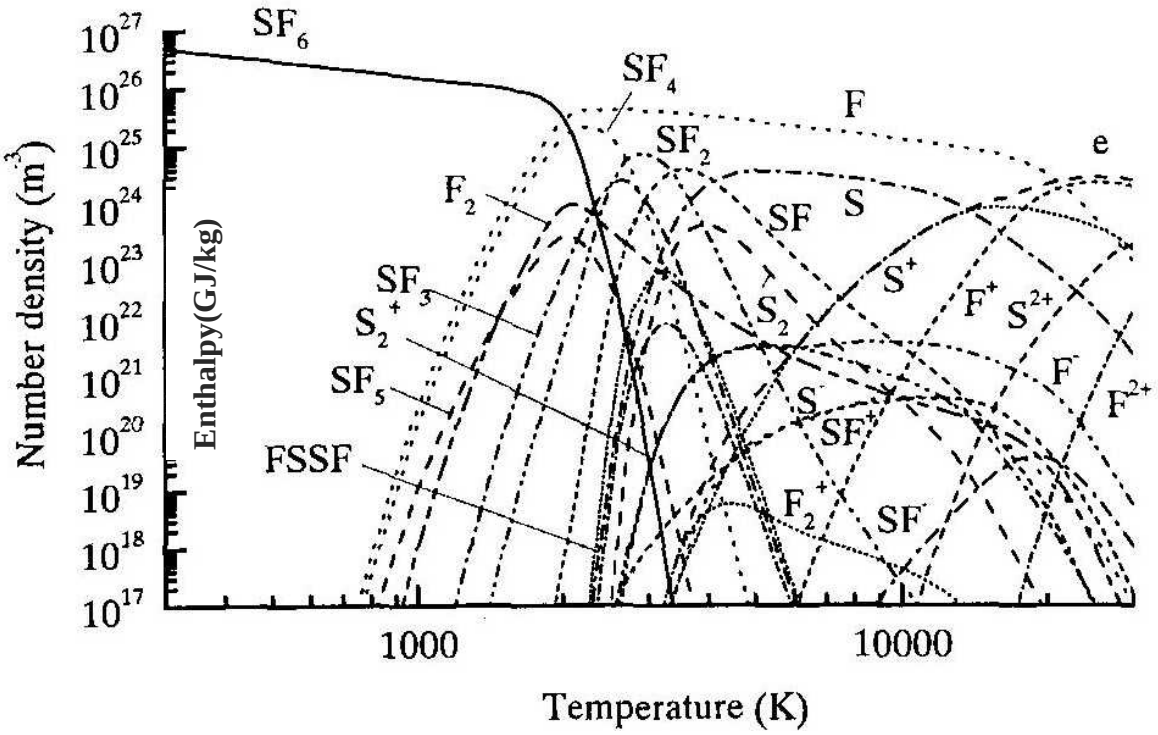

Figure 4.1 Equilibrium composition of SF_6 plasma at a pressure of 2 MPa

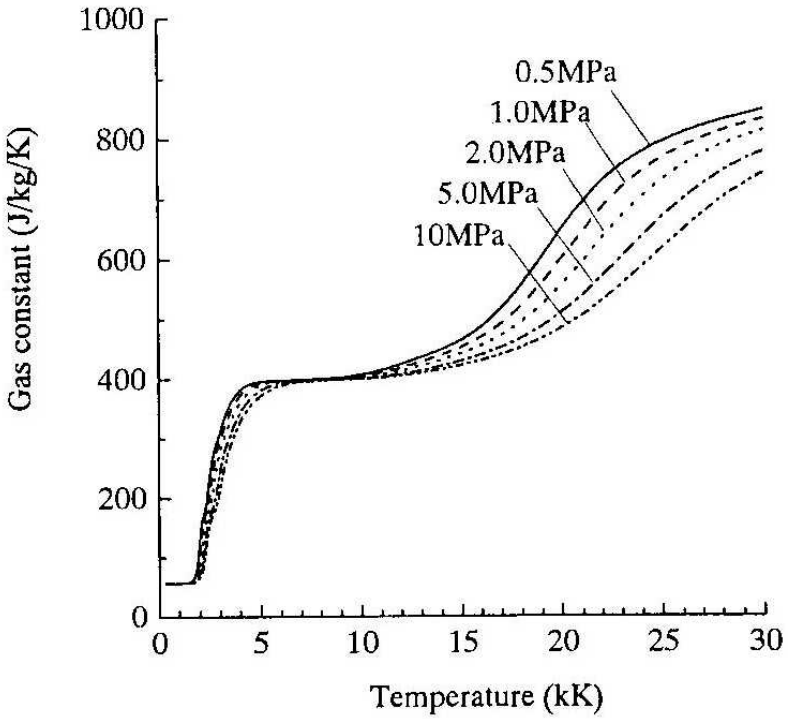

Figure 4.2 Gas constants *R*

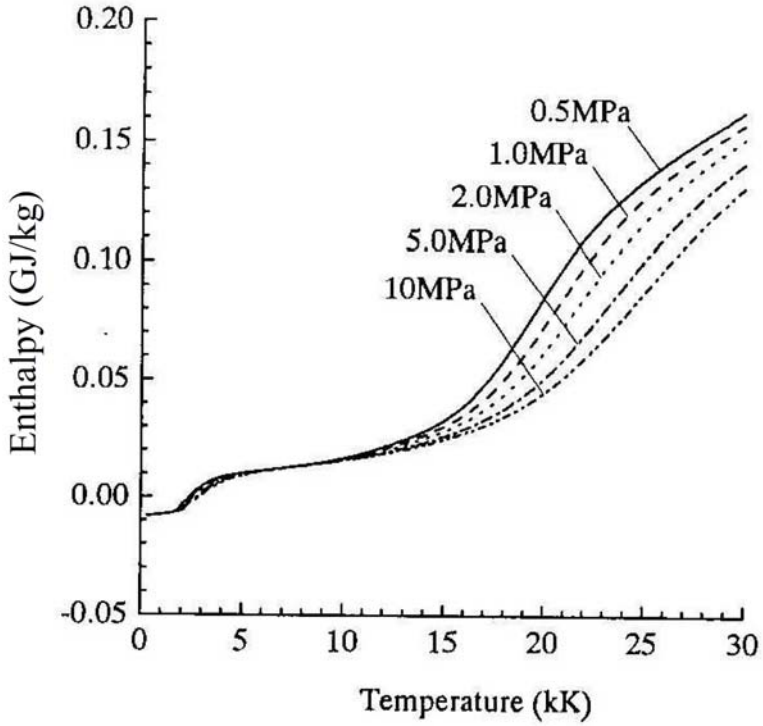

Figure 4.3 Enthalpy *h*

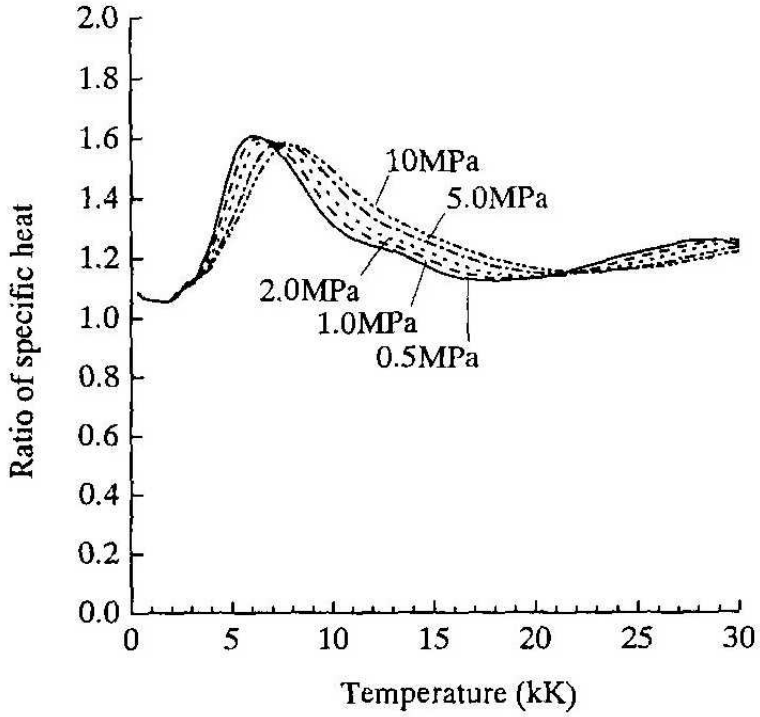

Figure 4.4 Specific heat ratio γ

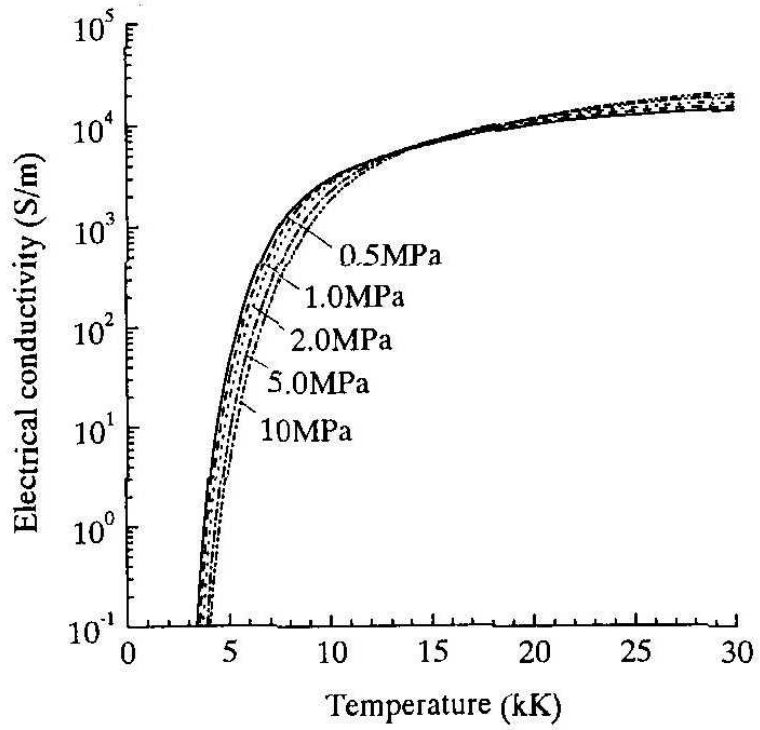

Figure 4.5 Electrical conductivity σ

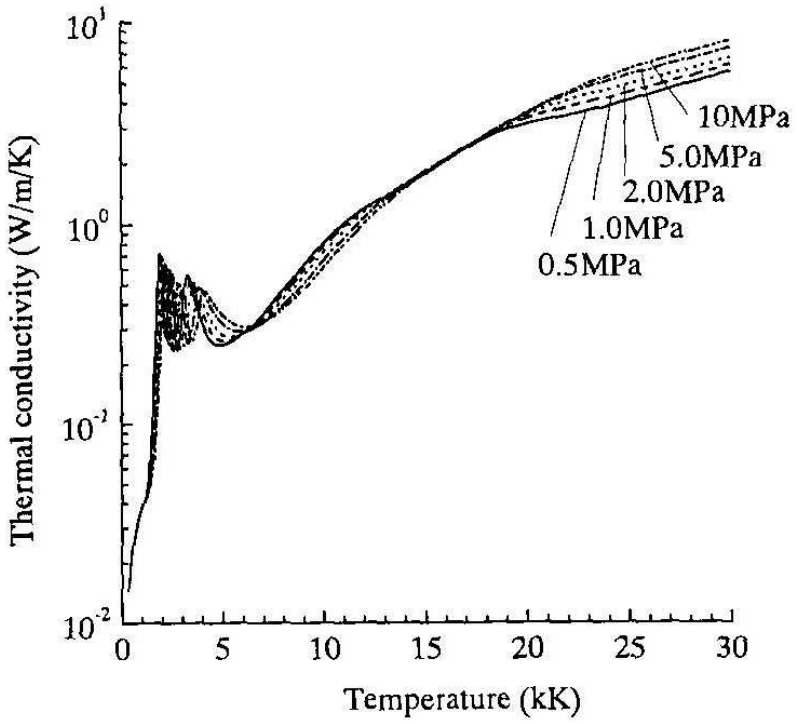

Figure 4.6 Thermal conductivity κ

Table 4.1 Comparison of results at 1.0 MPa with the results by Chervy et al.[5]

	Mass density (kg/m^3)		Enthalpy (MJ/kg)		Electrical conductivity (S/m)		Thermal conductivity (W/m/K)	
Temperature (K)	Result	Chervy et al.	Result	Chervy et al.	Result	Chervy et al.	Result	Chervy et al.
1000	17.799	17.6	-7.4951	-7.94	1.0267×10^{-37}	-	0.037316	0.0479
3000	1.1419	1.16	3.5540	2.78	0.0063340	0.00655	0.24367	0.440
10000	0.25031	0.247	16.162	15.8	2858.3	3420	0.76627	0.970
30000	0.040572	0.04	157.29	158	15517	21400	6.0760	8.73

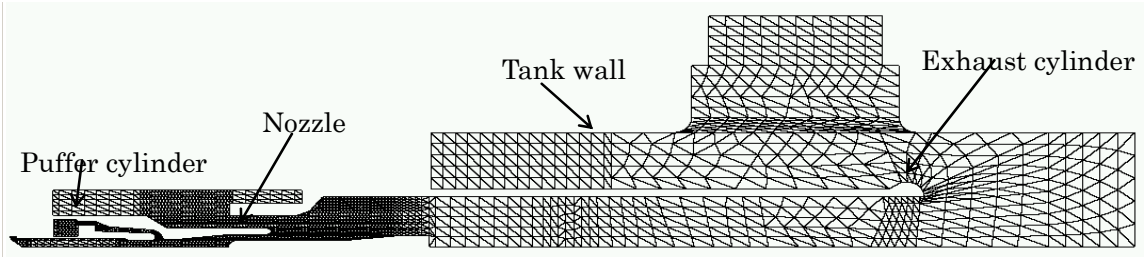

Figure 4.7 Cells for simulation (example for MMM)

cylinder, which creates a gas-flow during a current interruption. In the conventional method, a stationary contact and a puffer piston were moved because their configurations were simple and easy to move (SMM: Stationary parts Moving Method). Some researchers have achieved continuous moving by adopting high quality and complicated algorithms [12]. Attempting to develop engineering tools which require only reasonable time durations for the simulations, some cell data for different positions between close and open positions were used in the modified FLIC. As the simulation progress, data are transferred from the previous position to the next position.

Figure 4.8 shows movements of configurations and transfer of data in SMM. New cells were created at the front of a stationary contact, and cells in front of a puffer piston were deleted.

On the other hand, Fig. 4.9 shows a method in which an operational rod, a movable arcing contact, a movable main contact, and a nozzle move in the same way as real GCBs (MMM: Movable parts Moving Method). A block surrounded by thick lines including the movable parts moves to the left in the figure. The thick lines in the figure represent a state after one step of moving. In the puffer chamber, one row of cells in shaded area is deleted during the movement, and the corresponding mass is distributed to puffer chamber. On the right side of the block, cells in four shaded areas are generated to compensate blanks after the block move, and physical values are copied into the new cells from neighbours.

4.4 Simulation results

4.4.1 Pressure in puffer chamber

Pressures in the thermal-puffer were experimentally observed to compare and discuss results. It is true that agreements of simulation results with measured values of the puffer pressure do not guarantee the accuracy or the reliability of the program. However, pressure is

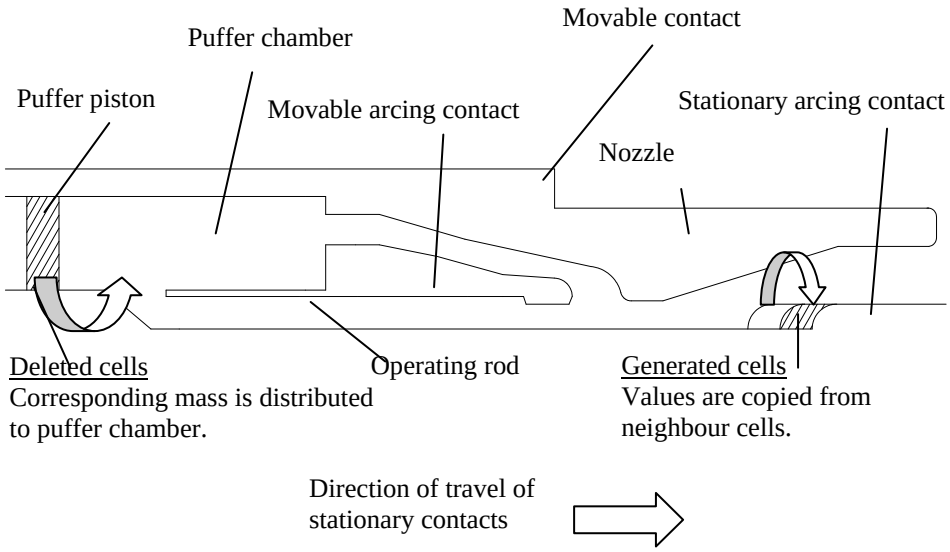

Figure 4.8 Data transport in SMM

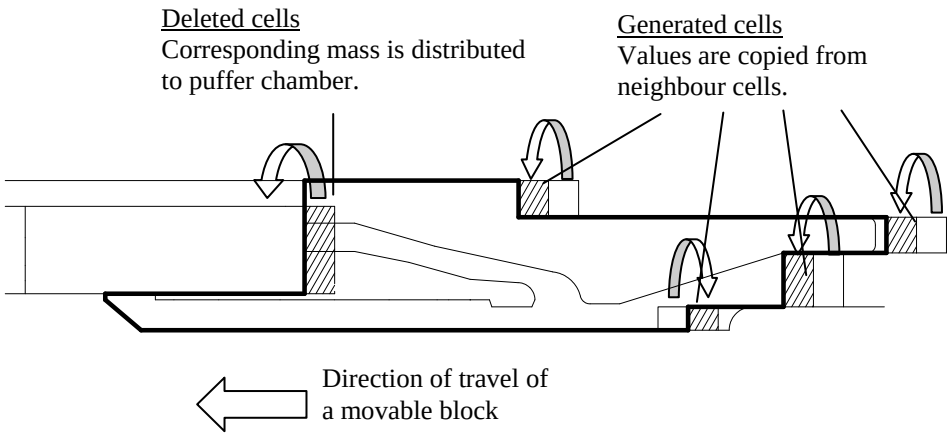

Figure 4.9 Data transport in MMM

one of the relevant factors when evaluating performance and is easy to measure. Therefore, comparing pressure values is an important and useful step when evaluating accuracies of gas-flow simulation programs for GCBs.

Figure 4.10 shows simulation results of pressure at a puffer chamber with measured ones. The measured values were obtained using a pressure sensor, which was installed at the centre

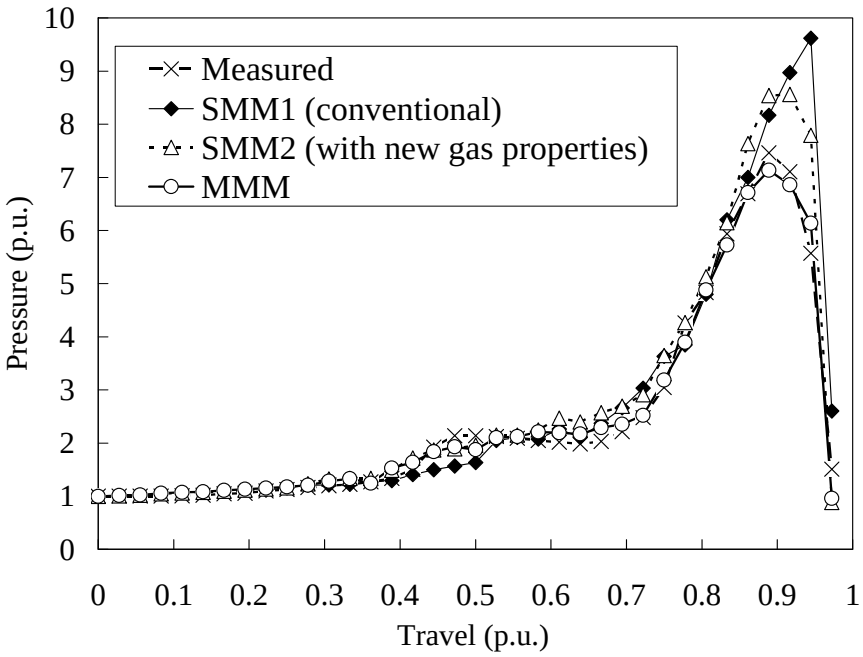

Figure 4.10 Pressure in puffer chamber
(Current: 50 kA, Arcing time : 20 ms)

of the puffer piston in the radius direction. The measured values were expected to include errors within 10% caused by EMC noise in the high power test environment with current of several kA, and specific errors of sensors or measurement instruments up to 1%. Figure 4.10 also includes a simulation result by a conventional simulation method 'SMM1', which had used SMM and SF_6 gas properties only up to 1.57 MPa. SMM2, SMM with the new gas properties, resulted in better values, which is not too high pressure around 0.9 p.u. of travel. However, SMM2 indicated higher values than the measured values. MMM with the new gas properties successfully agreed with the measured values.

Figures 4.11 (a) and (b) show pressure distributions in the puffer chamber at a travel of 0.9 p.u. for SMM2 with new gas properties and MMM, respectively. The distribution for SMM2 has partially high pressure while MMM had a uniform distribution.

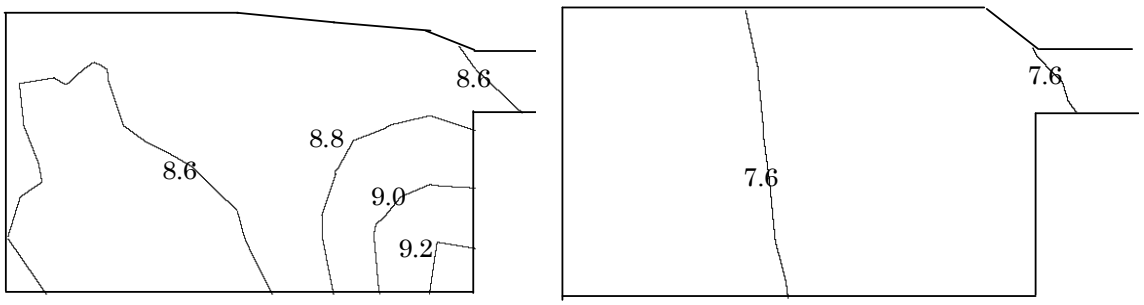

(a) SMM2 (b) MMM

Figure 4.11 Pressure distribution in puffer chamber
-Values on contours represent pressure in per unit.
(Current: 50 kA, Arcing time : 20 ms)

4.4.2 Gas-flow in exhaust cylinder

Another important purpose of the gas-flow simulation in GCBs is to investigate dielectric characteristics between chambers and enclosing tanks. The modified FLIC has simulated a hot-gas-flow exhausting from the chamber towards the tank wall [1][2]. The dielectric strengths after current zero are required to be known by the simulations mainly. Transient recovery voltages (TRVs), which are higher than operating voltage in the system, are applied to GCBs within several hundreds microseconds after current zero, then the operating voltage continuously follows. To evaluate dielectric strength, gas density and temperature are significant parameters along with electric field strength [13]-[15]. Figure 4.12 compares gas densities at the end of an exhaust cylinder, which is a critical point for dielectric performance [13][14] in a GCB, obtained by SMM2 and MMM. In these simulations, a high current arc of 50-Hz was ignited at 0 ms on the time axis and extinguished at 20 ms.

Densities by both SMM2 and MMM rose from a basic level up to at least 13 % by 19 ms. Then, the density of SMM2 with new gas properties started to drop at 19 ms and decreased to 75 % of a basic level. On the other hand, the density of MMM started to drop 1 ms later than SMM2 with new gas properties and decreased to 56 %.

4.4.3 Pressure in puffer chamber

The effect of considering detailed SF_6 gas properties can be stated for a reduction of pressure around 0.9 p.u. of stroke as shown in Fig. 4.10. The effect cannot be simply explained because the simulation treats non-linear data with iterations to obtain physical constants at each cell. However, it can be found that the pressure in the puffer chamber decreased because pressures at the arc area decreased due to a lower gas constant by using proper gas properties at higher pressures.

Second, differences between SMM2 and MMM should be discussed. Adding to large differences around stroke 0.9 p.u., as stated above, the different situation could be observed with a shorter stroke. Figures 4.13 (a) and (b) are density distributions in the puffer area of SMM2 and MMM, respectively. In Fig. 4.13 (a) of SMM2, the density around the hole in the puffer was locally low. This was because the hole stayed at the same place in the puffer. On the other hand, the density in Fig. 4.13 (b) of MMM was relatively uniform. This was

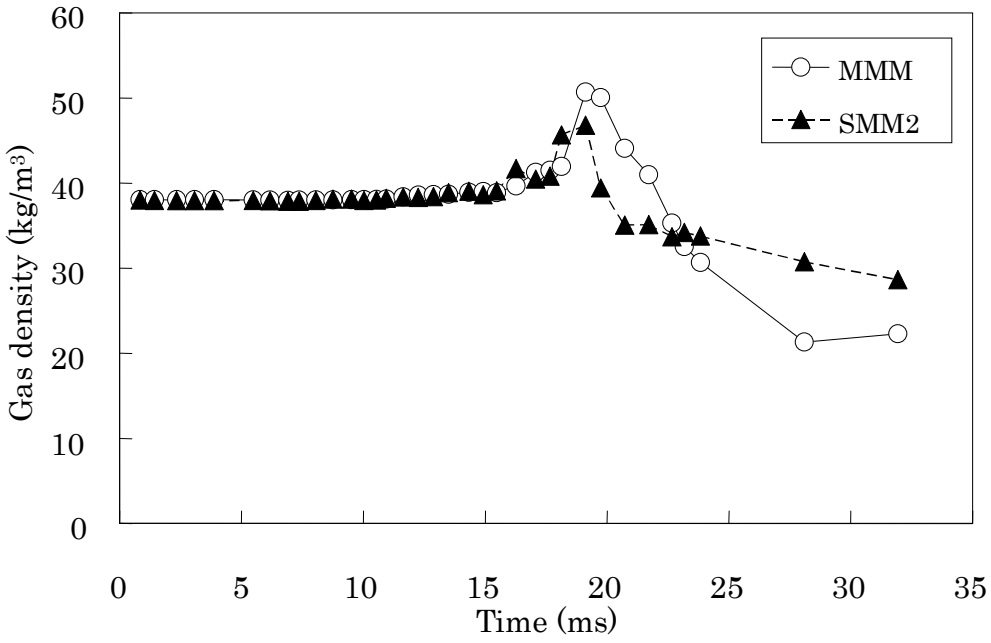

Figure 4.12 Gas density variation at end of exhaust cylinder
(Current: 50 kA, Arcing time : 20 ms)

because the hole moved towards the left side on the figure along the puffer, which prevented the hot gas from blowing out in the same place of the puffer cylinder. These differences on results would suggest that MMM of which movement is closer to one of real GCB would be better method to simulate the advanced Hybrid-puffer^{TM}-type chambers precisely.

4.4.4 Gas-flow in exhaust cylinder

The reason why densities rose around 17 ms in Fig. 4.12 was that hot gas flowing in the exhaust cylinder pushed and compressed the cold gas forwards. This phenomenon had also measured experimentally in GCBs [16], which suggested that the simulations in this section

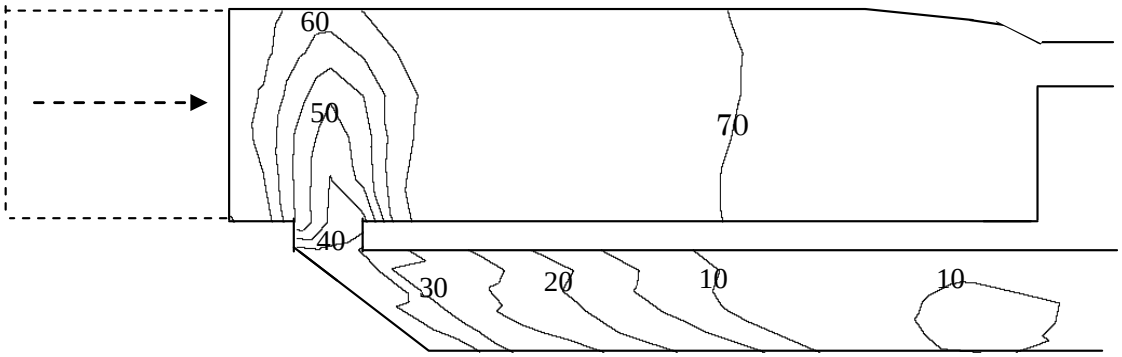

(a) SMM2

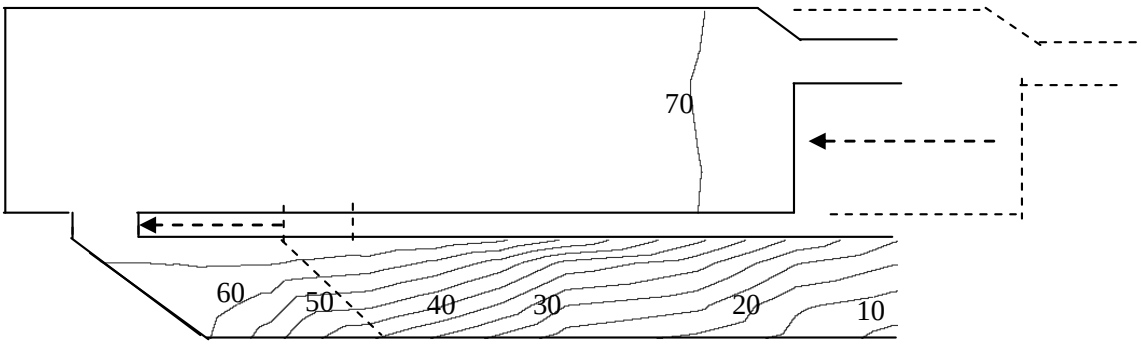

(b) MMM

Figure 4.13 Gas density distribution in puffer chamber
- Values on contours represent gas density (kg/m^3).
(Current: 50 kA, Arcing time : 20 ms)

gave the proper trends.

Differences of a delay in the density drop and density level after the drop between SMM2 and MMM could be explained by the following fact. As shown in Fig. 4.10, the pressure in the puffer chamber calculated by SMM2 was higher than that by MMM, which might create a strong gas-flow towards the exhaust cylinder. Therefore hot gas in SMM2 reached top of the exhaust cylinder faster than that in MMM, as shown in Fig. 4.12. Moreover, the hot gas travelling in the exhaust cylinder moved with forming one large area, which was mixed with cool gas forward and backward. When the gas was generated at a higher pressure, as seen in SMM2, the hot gas could mix with the cool gas very well. Therefore, the SMM2 resulted in a higher density at the top of the exhaust cylinder than MMM after 25 ms in Fig. 4.12.

The differences stated in this section also suggest that MMM of which movement is closer to one of real GCB is a better solution than SMM2 to simulate dielectric strength against dead-tanks in the advanced Hybrid-puffer^{TM}-type chambers.

4.5 Development of GCB

By adopting the simulation described in this chapter and the other investigations including one in Chapter 3, a new GCB for 245/252-kV GIS had been developed with appropriate configurations. This GCB was performed for all of the required tests successfully. Moreover, 145-kV GCB [17] had been developed with similar procedures.

4.6 Conclusions

This chapter presents the improvement on hot-gas-flow simulation method for the advanced Hybrid-puffer^{TM}-type GCB chamber as follows.

(a) Considering the thermodynamic and transport properties of SF_6 gas for high temperature and high pressure: Gas constant, enthalpy, ratio of specific heat, electrical conductivity,

and thermal conductivity have been obtained for SF_6 gas of temperature 300–30000 K and pressure up to 10 MPa. The simulation results by the modified FLIC taking into account these values gave lower puffer pressures which were closer to measured values.

(b) Simulating movement of movable parts: Movable parts in a GCB were moved in the new method simulation Movable parts Moving Method (MMM). In a comparison of MMM and Stationary parts Moving Method with new gas properties (SMM2), MMM resulted in a lower pressure in the puffer chamber, which agreed with the experimentally measured value much better than in SMM2. This difference on puffer pressure also resulted in later and lower drops of density at the top of exhaust cylinder in MMM, which had to be much closer to real phenomena. The differences on the puffer pressure arose from differences on movement of a hole on an operating rod. The hole stayed at same place of the puffer chamber in SMM2, while the hole moved along the puffer chamber in MMM. Therefore, for precise simulation, the MMM should be employed when the hole on the operating rod moves in the puffer chamber, as the same in the advanced Hybrid-puffer^{TM}-type chambers.

(c) The simulation methods described in this chapter were adapted to develop new GCBs of 145-kV and 245-kV.

References

[1] M. Okamoto, M. Ishikawa, K. Suzuki, and H. Ikeda: “Computer simulation of phenomena associated with hot gas in puffer-type gas circuit breaker,” *IEEE Trans. on Power Delivery*, Vol. 6, pp. 833-839, April 1991

[2] T. Mori, H. Ohashi, H. Mizoguchi, and K. Suzuki: “Investigation of technology of developing large capacity and compact size GCB,” *IEEE Trans. Power Delivery*, Vol. 12, pp. 747-753, Feb. 1997.

[3] L. S. Frost and R. W. Liebermann: “Composition and transport properties of SF_6 and their use in a simplified enthalpy flow arc model,” *Proc. IEEE*, vol. 59, pp. 474-485, April 1971

[4] A. Gleizes, M. Razafinimanana, and S. Vacquié: “Equilibrium composition thermodynamic properties and transport coefficients of SF_6-N_2 mixtures,” *Internal Report 40277-85-1*, CNRS, EDF arc Electrique, Feb. 1985

[5] B. Chervy, A. Gleizes, and M. Razafinimanana: “Thermodynamic properties and transport coefficients in SF_6-Cu mixtures at temperatures of 300-30000 K and pressures of 0.1-1MPa,” *J. Phys. D, Appl. Phys*., Vol. 27, pp. 1193-1206, 1994.

[6] J. Y. Trépanier, M. Reggio, H. Zhang, and R. Camarero: “A finite-volume method for the Euler equations on arbitrary Lagrangian-Eulerian grids,” *Computers Fluids*, Vol. 20, No. 4, pp. 399-409, 1991

[7] P. Chévrier, M. Barrault, C. Fiéver, J. Maftoul, and J. Millon Frémillon: “Industrial applications of high-, medium- and low-voltage arc modelling,” *J. Phys. D, Appl. Phys.*, Vol. 30, pp. 1346-1355, 1997.

[8] M. Claessens, K. Möller, and H. G. Thiel: “A computational fluid dynamics simulation of high- and low-current arcs in self-blast circuit breakers,” *J. Phys. D, Appl. Phys.*, Vol. 30, pp. 1899-1907, 1997.

[9] S. Kwan, M. S. Christodoulou, W. Hall, and M. T. C. Fang: “The theoretical modelling of puffer circuit breakers,” *Proceedings of the 11th International Conference on Gas Discharges and Their Applications*, Vol. 1, pp. 374-377, Sep. 1995

[10] S. Yanabu, H. Mizoguchi, and M. Toyoda: “Development of novel hybrid interrupting chamber for gas circuit breaker utilizing self-pressure-rise phenomena by arc,” *IEEE Trans. Power Delivery*, Vol. 4, pp. 355-361, Jan. 1989.

[11] T. Mori, H. Mizoguchi, N. Kato, and M. Toyoda: “Investigation of two types of interrupting chamber with low drive energy and development of 245-kV GCB,” *IEEE Trans. Power Delivery*, Vol. 10, pp. 158-167, Jan. 2004.

[12] S. D. Eby and J. Y. Trépanier: “Computation of the radiative transfer in SF_6 circuit-breaker arcs using the P-1 model of radiation,” *Proceedings of the 12th International Conference on Gas Discharges and Their Applications*, Vol. 2, pp. 570-573, Sep. 1997

[13] T. Uchii, S. Nishiwaki, and S. Boggs: “Effects of hot SF_6 on post-arc circuit breaker design,” *IEEE Trans. Power Delivery*, Vol. 10, pp. 124-130, Jan. 2004.

[14] T. Uchii, T. Nakamoto, S. Nishiwaki, M. Toyoda, and S. A. Boggs: “Optimization of dead tank gas circuit breaker design based on quantification of hot gas flow and dielectric properties,” *IEEE Trans. Power Delivery*, Vol. 10, pp. 181-184, Jan. 2004.

[15] G. J. Cliteur, Y. Hayashi, E. Haginomori, and K. Suzuki: “Calculation of the uniform breakdown field strength of SF_6 gas,” *IEEE Trans. Dielect. Elect. Insul.*, Vol. 5, pp. 843-849, Dec. 1998.

[16] Y. Hayashi, G. J. Cliteur, M. Ishikawa, and K. Suzuki: “Diffusion process of hot gas flow during the short circuit current interruption of SF_6 gas circuit breaker,” *Proceedings of the 11th International Conference on Gas Discharges and Their Applications*, Vol. 1, pp. 390-393, Sep. 1995.

[17] M. Toyoda, H. Mizoguchi, T. Uchii, T. Yokota, T. Ueda, and S. Ohyama: “Review of GCB and its improved interrupting chamber,” *Beijin International Conference On Power Transmission & Distribution Technology 2001*, pp. 2001-2011, 2001.

Chapter 5 Gas-flow Simulation in Tandem-puffer-type GCB Chambers

5.1 Introduction

Even after release the advanced Hybrid-puffer^{TM}-type chamber, demands for low cost GCB have been strong. Additionally, spring operating mechanisms are preferred rather than hydraulic ones due to their easiness of maintenance. Output force of the spring operating mechanism gradually drops in GCB's operation, while the hydraulic operating mechanism almost keeps its force. Puffer-type interruption chambers including the Hybrid-puffer^{TM}-type and the advanced Hybrid-puffer^{TM}-type mechanically compress the gas in the puffer chamber, which can generate large repulsive force on the puffer piston in the end period of opening operation.

In order to be able to apply spring operating mechanisms, further reduction on the operating energy was expected. In such a trend, a new type of chamber called a tandem-puffer-type chamber, which does not use mechanical compression to blast gas in high current interruptions, started to be developed [1]. This type of chamber greatly features hot gas to build puffer pressure. Therefore, hot-gas-flow simulation program is a very important tool for developing this type of GCBs. However, it was found that gas-flow simulations, in which the high temperature properties of pure SF_6 gas were used as described in Chapter 4, could not provide proper pressure values in the puffer chamber of the tandem-puffer-type.

This chapter describes investigations on obtaining a reasonable puffer pressure in gas-flow simulations of a tandem-puffer-type chamber. The simulation methods have been developed using the modified fluid-in-cell (FLIC) [2]-[4]. The properties of pure SF_6 gas in regions up to 10 MPa and 30000 K have been already adopted in Chapter 4. However, the

thermodynamic and transport properties of SF_6-Polytetrafluoroethylene (PTFE) mixed gas have not been reported for high-pressure and high-temperature regions. Expecting a key-point in simulating tandem-puffer-type chambers, the properties up to 10 MPa and 30000 K were obtained and were adopted in hot-gas-flow simulations in this chapter. Moreover, arcs were modelled as grids of resistors to simulate changes of arc diameters which strongly related with gas-flow mass at nozzle throat.

5.2 Tandem-puffer-type GCB chamber

Tandem-puffer-type chambers have been adopted to operate by small operating energy of the spring mechanism. Figure 5.1 shows schematic figure of a tandem-puffer-type chamber in which a thermal-puffer chamber is connected in series to a mechanical-puffer one through a relief valve. Its basic ideas have been proposed in 1960s [5], and some manufacturers in Europe have released such type of GCB from 1980s. Although developments of 300-kV 50-kA GCB were reported on the paper in 1997 [6], there have been no information for further high voltage GCBs such as 420-kV or 550-kV since then, besides some manufactures have been trying to develop them [7].

In the case of a large current interruption, as shown in Fig. 5.1(a), this type of chambers generates high pressures by taking hot gas into a thermal-puffer chamber from high current arcs, and the high-pressure gas blows into the arcing area at around current zero. The gas in the mechanical-puffer is diffused through the exhaust valve into the outside, which prevents the large repulsive force on the puffer piston. In this sense, the mechanical-puffer does not contribute to large current interruptions.

When a small current is interrupted, the gas pressure in the thermal-puffer chamber does not increase enough because of small arc energy. However, the mechanical piston compresses the gas in the mechanical-puffer chamber and then blast the gas through the relief valve and

thermal chamber into the arcing area as shown in Fig. 5.1(b). This gas-flow results in the successful small current interruption.

This chapter focuses on the large current interruption. Since the mechanical-puffer does not contributes in the large current interruption as described above, gas pressure behaviour only in the thermal-puffer chamber without mechanical pistons was discussed in following sections.

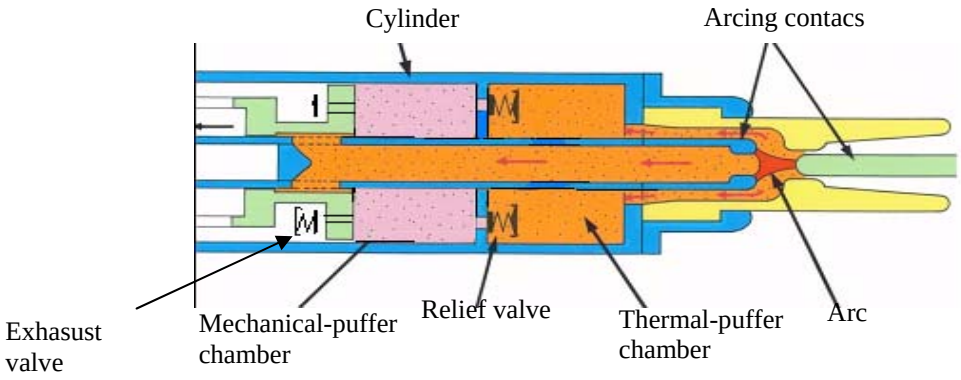

(a) Large current interruption

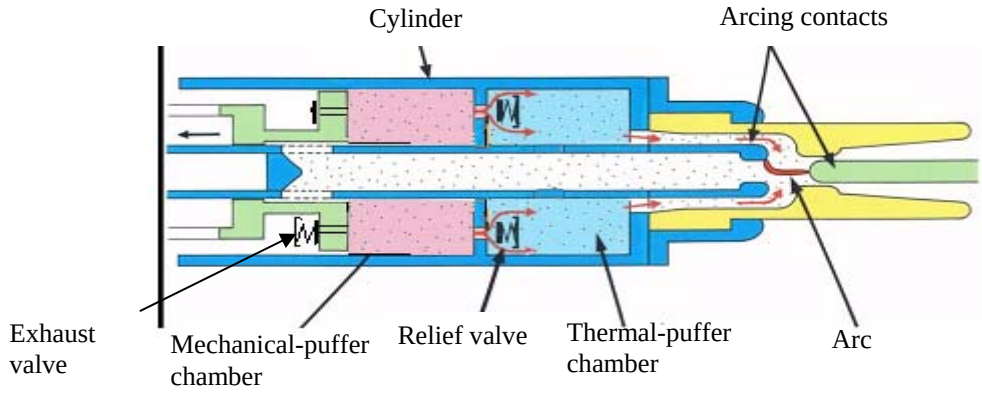

(b) Small current interruption

Figure 5.1 Schematic fugure of a tandem-puffer-type chamber

5.3 Calculations of thermodynamic and transport properties of SF_6-PTFE gas

The thermodynamic and transport properties of pure SF_6 gas up to 10 MPa and 30000 K were used in Chapter 4. In this Chapter, PTFE gas ablated from a nozzle was additionally considered, and properties of SF_6-PTFE mixture were calculated. This section outlines the calculation methods for the properties followed by their results.

5.3.1 Calculation methods

Calculation method is the same as one explained in the Chapter 4, but particles relating PTFE shown in Table 5.1 are taken into account. In addition to electrons, 22 kinds of particle originated from SF_6 gas, and another 22 from PTFE gas. Equilibrium compositions of SF_6-PTFE mixed gas at various pressures were obtained. Using the results of gas composition, the properties in high-pressure and -temperature gas with a mixture of related molecules, atoms, ions, and electrons were calculated.

5.3.2 Calculation results

Figures 5.2 to 5.6 show examples of the calculation results of gas constant R, enthalpy h, specific heat ratio γ, electrical conductivity σ, and thermal conductivity κ, respectively. Each figure includes the lines for PTFE mass ratios of 0, 25, 50, 75, and 100% at pressures of 1 MPa. Similarly, the results for pressures up to 10 MPa were obtained successfully.

Table 5.1 Considered particles in SF_6-PTFE gas

	Originate from SF_6	Originate from PTFE
Molecules	SF_6, SF_5, SF_4, SF_3, SF_2, SF, SSF_2, FSSF, F_2, S_2	C_2F_6, C_2F_4, C_2F_2, CF_4, CF_3, CF_2, CF, CS_2, CS, C_5, C_4, C_3, C_2
Atoms	F, S	C
Ions	F-, F+, S+, F_2^+, S_2^+, S^-, S_2^+, F_2^+, SF^+, SF^-	CF_3^+, CF_2^+, C^+, C^-, C_2^+, CS^+, C_2^+, C_2^-
Electrons	e^-	

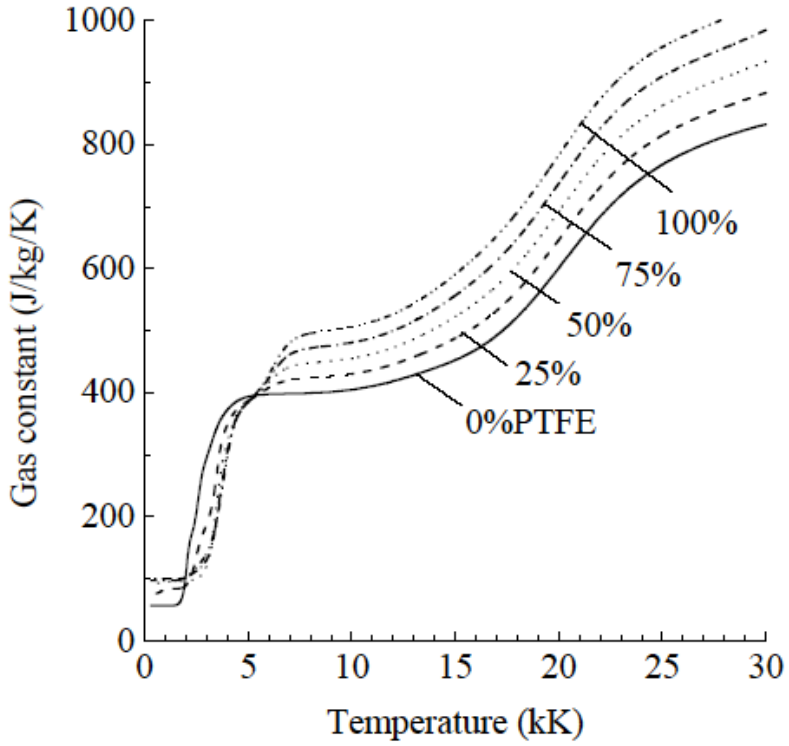

Figure 5.2 Gas constant R of SF_6-PTFE at a pressure of 1 MPa for different mixture ratios

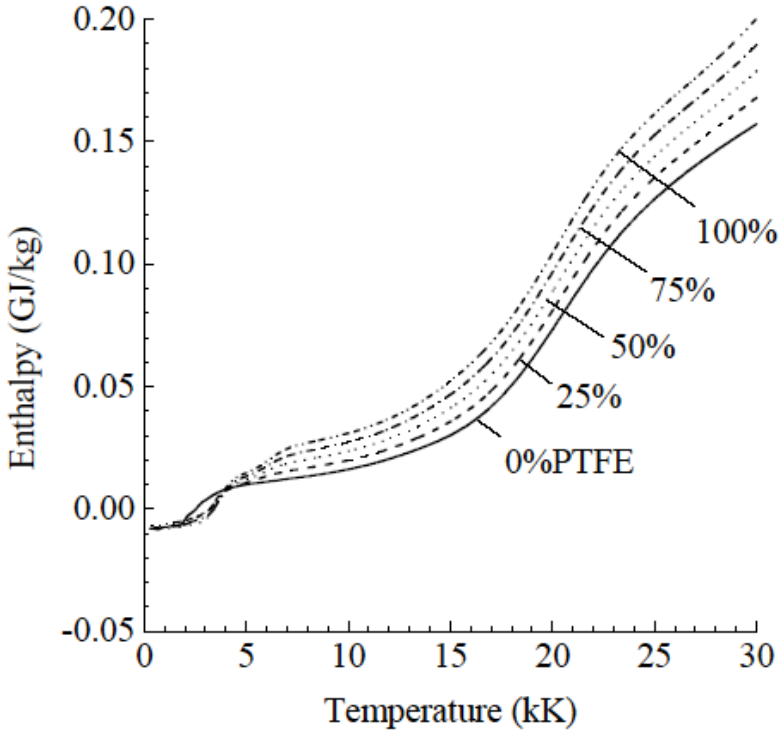

Figure 5.3 Enthalpy h of SF_6-PTFE at a pressure of 1 MPa for different mixture ratios

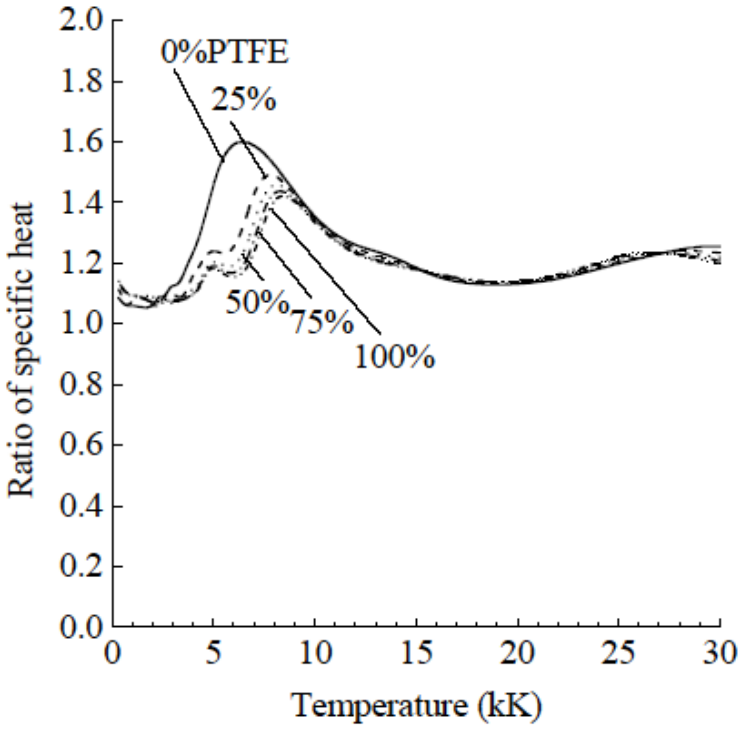

Figure 5.4 Specific heat ratio γ of SF_6-PTFE at a pressure of 1 MPa for different mixture ratios

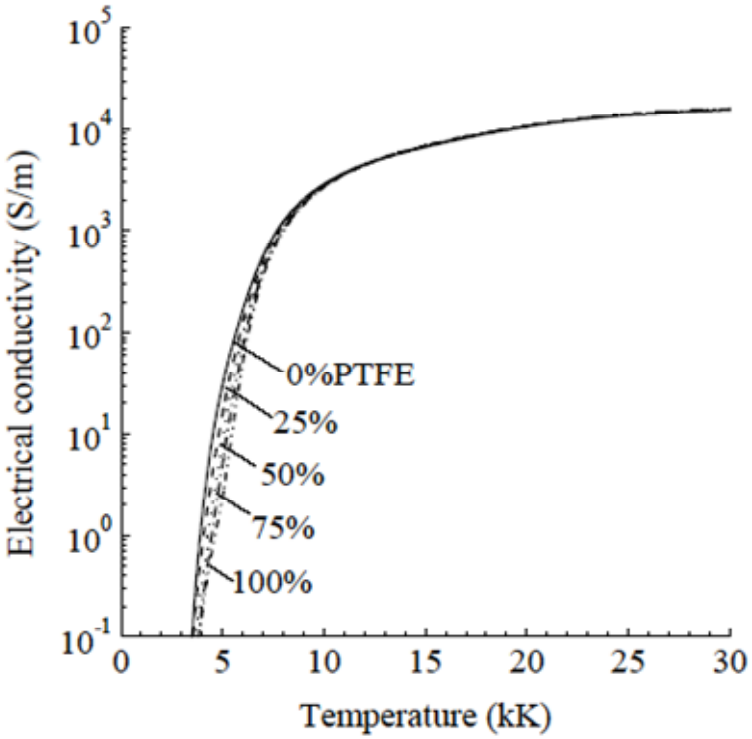

Figure 5.5 Electrical conductivity σ of SF_6-PTFE at a pressure of 1 MPa for different mixture ratios

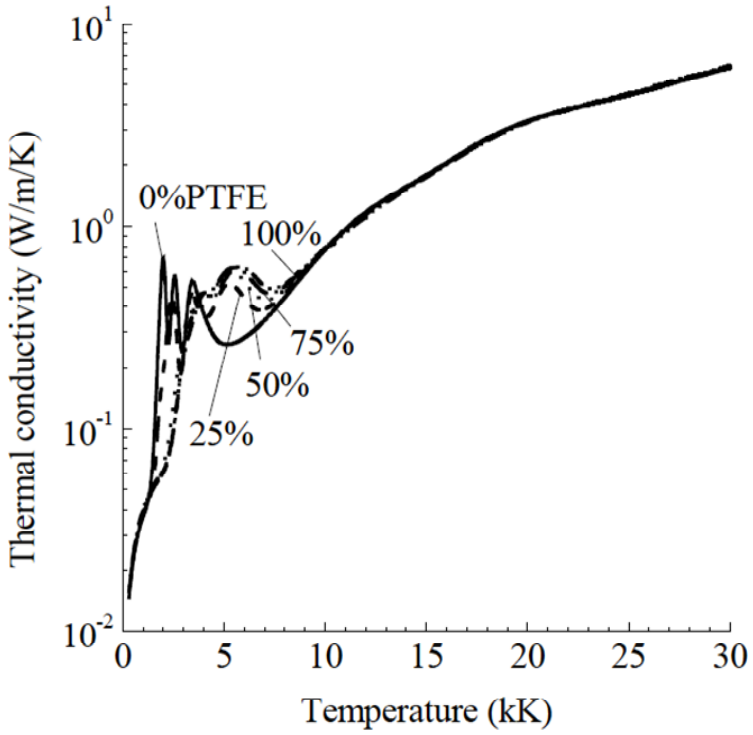

Figure 5.6 Thermal conductivity κ of SF_6-PTFE at a pressure of 1 MPa for different mixture

5.4 Programs of gas-flow simulations

Four revisions of the modified FLIC were compared in this chapter with the following features, where the SMM (Stationary parts Moving Method) was adopted because holes on the operating rod do not move in the puffer chamber in the simulations.

a FLIC-A : This revision was developed in Chapter 4 as the SMM2. Arc energy was given by multiplying arc current and average arc voltage, which was specified by referring to experimental measured values in similar cases. The ablated PTFE and copper, which were materials of nozzles and arcing contacts, were represented as masses appearing on the surfaces of nozzle walls or electrodes [3]. The total amounts

of ablated materials were estimated from experimental results. Thermodynamic and transport properties of pure SF_6 gas up to a pressure of 10 MPa and a temperature of 30000 K were adopted [4].

b FLIC-B : In addition to FLIC-A, the thermodynamic and transport properties of SF_6 gas in the arcing area were multiplied by constants to model pure PTFE gas. The multiplied constants were determined for 0.1 MPa from literature [8][9], and the same values were used for other pressures. Here, literature [10] suggests that the assumption of pure PTFE gas could not be so unrealistic in high current conditions.

c FLIC-C : In addition to FLIC-B, the electrical conductivity of the arcs was derived at every cell in the arcing area. The cells in the arcing area were modelled as grids of resistors, and arc current was distributed among parallel cells in inverse proportion to resistance. The arcing energy in each cell was calculated as Joule heat energy. The current could concentrate in cells along the axis, and arc diameters could be smaller under lower current conditions. Here, the arc resistances were too high under very low current conditions. Therefore, a higher limit of resistance was set. This is because current density becomes low in practical size cells, while actual arc diameter can be small and current density becomes high to maintain high temperature arc core.

d FLIC-D : In addition to FLIC-C, thermodynamic and transport properties of SF_6-PTFE mixed gas up to 10 MPa and 30000 K had been considered in the entire simulated area, instead of the multiplier only in the arcing area introduced in FLIC-B and -C. PTFE mass which had already been given in FLIC-A could flow in every area, therefore the program calculated mixture ratio of SF_6 and PTFE in every cell.

5.5 Simulation results

Figure 5.7 shows puffer pressures in a tandem-puffer-type chamber obtained by FLIC-A, FLIC-B, FLIC-C and FLIC–D. The pressure values with FLIC-A were much lower than

experimental data, while the puffer pressures by FLIC-A agreed quite well with experimental data in an Advanced Hybrid-puffer as shown in Chapter 4. The pressure values with FLIC-B, FLIC-C, and FLIC–D indicated higher values than the former, respectively. FLIC-D agreed with experimental data best among the four approaches.

5.6 Evaluations of considered factors

All of the new methods introduced in FLIC-B, FLIC-C and FLIC-D contributed to obtaining a higher puffer pressure. The reason cannot be stated easily because the simulation treats non-linear phenomena, and the effects might appear as accumulations of many factors. However, it can be explained qualitatively as described below.

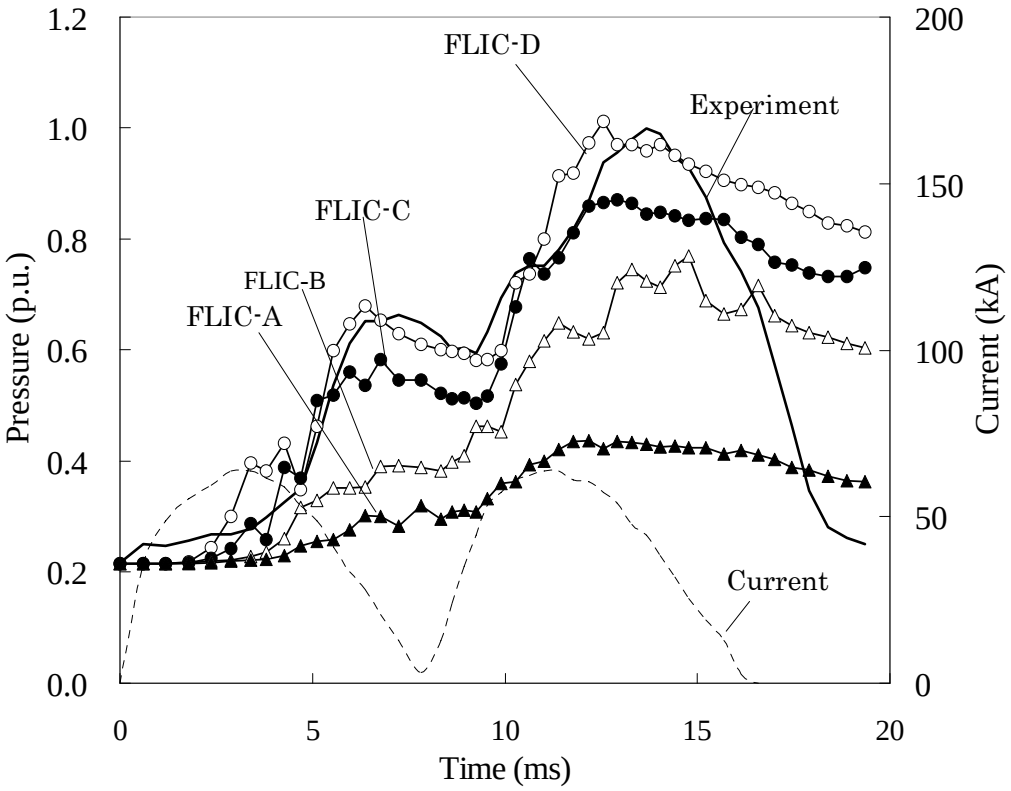

Figure 5.7 Puffer pressure in a tandem-puffer-type chamber
(Current: 50 kA, Arcing time: 20 ms)

5.6.1 Thermodynamic and transport properties of high-pressure and -temperature SF_6-PTFE gas

Comparing FLIC-A with FLIC-B, and FLIC-C with FLIC-D leads to the conclusion that the thermodynamic and transport properties of SF_6-PTFE gas greatly affect the gas pressure in the puffer chamber. Gas constant R shown in Fig. 5.2 is higher for higher rate of PTFE. For example, R at 15000 K is 590 J/kg/K for 100% PTFE which is 1.3 times of 450 J/kg/K for 0% PTFE. Gas constant R affects pressure p proportionally at each cell as shown in the Eq. (1.11),

$$R = \frac{p}{\rho T}, \tag{1.11}$$

where, ρ is gas density and T is gas temperature. Although there are both factors for increments and decrements of gas pressures, judging from the results in Fig. 5.7 and the Eq. (1.11), the increments of R values could be the main factor increasing puffer pressure.

It can be also concluded that consideration of the properties of SF_6-PTFE in all simulated area gives more accurate results than considering them only in the arcing area. This means that the diffusion of PTFE gas in the puffer chambers contributes to increasing pressure, and temperature rise and mass-flow are not all of sources of the pressure rise.

5.6.2 Conductivities and diameters of arcs

The puffer pressures by FLIC-C are higher than that obtained by FLIC-B. This might be caused by temperature rises in the lower current region. In the calculation by FLIC-B, the current flowed uniformly in the arcing area, even in case of a lower current, which made current density and pressure lower. On the other hand, calculation by FLIC-C, the current concentrated towards the centre axis in case of a lower current, which makes the current density higher than that by FLIC-B. Therefore, even after peak current, temperature within an arc remained high, which might produce a high pressure as derived by the Eq. (1.11). Moreover, the arc voltage with FLIC-C is higher than the given constant value by FLIC-B in

the lower current region. However, when the current became very low around current zero in FLIC-C, the arc diameter shrank and the gas-flow through the nozzle throat around the arc differed from the flow around the large current arc, even though the arc maintained high temperature and pressure. This might be the reason why FLIC-C and FLIC-D indicated decrements around 9 ms in Fig. 5.7, which agreed with experimental data very well.

5.6.3 The reason why FLIC-A does not agree in the tandem-puffer-type chamber

There remains a question as to why FLIC-A did not agree with experimental data in the tandem-puffer-type chambers while it was relatively useful in the advanced Hybrid-puffer^{TM}-type chambers. Figure 5.8 shows examples of ratios of P_{L90} (measured maximum pressure in puffer chamber with short-line fault (SLF) 90% current interruption) against $P_{no\text{-}load}$ (that with no-load operation). The value of $P_{L90}/P_{no\text{-}load}$ for the tandem-puffer-type chamber is twice of that of the advanced Hybrid-puffer^{TM}-type. This suggests that the thermal energy in the tandem-puffer-type chambers dominates the formation of puffer pressure with a high current interruption, while the advanced Hybrid-puffer^{TM}-type still depends on mechanical

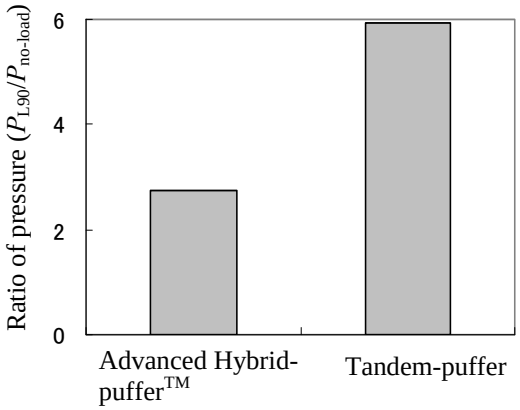

Figure 5.8 Ratio of maximum puffer pressure in L90 interruption against that in no-load operation

compression. In high-temperature condition, presence of PTFE makes the gas pressure higher , therefore, it might not be mandatory to consider PTFE properties or arc diameter for the advanced Hybrid-puffer^{TM} or the Hybrid-puffer^{TM}-type chambers, while it might be mandatory after featuring hot gas in the tandem-puffer-type chambers. The literature [11] reports that multi-molecule simulations of pure SF_6 gas are much different from mono-molecule simulation in the tandem-puffer-type chambers, while both simulation methods were not so different in puffer-type chambers. This phenomenon seems to be due to similar reasons.

5.7 Conclusions

This chapter described how taking account of thermodynamic and transport properties of SF_6-PTFE mixed gas in a large area in a simulated chamber was important for obtaining reasonable values in hot-gas-flow simulations for tandem-puffer-type chambers. This indicated that one of the important mechanisms of pressure rise in a tandem-puffer-type chamber was gas properties along with temperature rise and mass contamination. Furthermore, taking account of arcing diameter according to the properties was one of the relevant factors.

On the contrary, to simulate conventional puffer-type chambers, they were not so relevant and it could be unnecessary to consider the above, which might make a simulation simpler and faster. Users of hot-gas-flow simulations should select simulation methods carefully.

By adopting the simulation described in this chapter, a new 300-kV GCB had been developed with appropriate configurations

References

[1] T. Shinkai, M. Ooi, T. Uchii, H. Kawano, T. Nakamoto, and H. Ikeda: “Gas density and temperature in thermal volume for self-blast interrupting chambers,” *Proc. of IEEE/PES T&D Conf. and Ex. 2002: Asia Pacific*, Vol.1, pp. 419-423, 2002

[2] M. Okamoto, M. Ishikawa, K. Suzuki, and H. Ikeda: “Computer simulation of phenomena associated with hot gas in puffer-type gas circuit breaker,” *IEEE Trans. Power Delivery*, Vol. 6, pp. 833-839, April 1991

[3] T. Mori, K. Iwamoto, T. Nakamoto, and K. Suzuki: “Development of gas flow simulation method considering ablation for GCB chambers,” *The Papers of Technical Meeting on Switching & Protecting Eng., IEEJ*, SP-99-86, pp.61-66 (1999) (In Japanese)

[4] H. Kawano, K. Iwamoto, N. Kato, Y. Tanaka, and T. Sakuta: “Gas flow simulation for GCB chambers by moving movable parts,” *The Papers of Technical Meeting on Switching & Protecting Eng., IEEJ*, SP-01-33, pp.57-62 (2001) (In Japanese)

[5] U.S Patent No.4139752 (Japanese patent No.1176027)

[6] W. Hofbauer and J. Stechbarth: “Strategic tools-application for the development of a 300kV/50kA GIS self-blast circuit breaker”, *CIGRE*, SC13-110, August 1994

[7] F. Leclerc, P. Chevrier, G. Charot, G. Gaudart and A. Giboulet: “Compactness and reliability of new gas insulated switchgear with a rated voltage of 420 kV”, *CIGRE*, SA3-105, August 2006

[8] L. S. Frost and R. W. Liebermann: “Composition and transport properties of SF_6 and their use in a simplified enthalpy flow arc model,” *Proc. IEEE*, Vol. 59, pp. 474-485, April 1971.

[9] P. Kovitya: “Thermodynamic and transport properties of ablated vapors of PTFE, alumina, perspex, and PVC in the temperature range 5000-30000 K,” *IEEE Trans. Plasma Sci.*, Vol. PS-12, no. 1, pp. 38-42, Mar. 1984.

[10] P. Chévrier, M. Barrault, C. Fiéver, J. Maftoul, and J. Millon Frémillon: “Industrial applications of high-, medium- and low-voltage arc modelling,” *J. Phys. D, Appl. Phys.*, Vol. 30, pp. 1346-1355, 1997.

[11] N. Osawa and Y. Yoshioka: “The calculation method of puffer pressure in gas circuit breaker taking decomposition gas effect into consideration,” *IEEJ Trans. PE*, Vol. 123, No. 8, pp. 1002-1010, 2003

Chapter 6 Diagnostic Measurements on Rotary-arcs in Hollow Polymeric Cylinders

6.1 Introduction

The tandem-puffer-type gas circuit breaker (GCB) which has a mechanical-puffer has been being developed. The tandem-puffer-type GCBs require less operating energy than the conventional type ones. However, there are further demands for GCBs with lower operating energy. To respond such trends, some high voltage interrupters utilise a combination of electromagnetic fields and polytetrafluoroethylene (PTFE) nozzles in order to provide a suitable arc quenching environment [1][2], and the 72-kV GCB is the highest class one which has manufactured without a mechanical-puffer chamber so far [3]. On the other hands, the physical conditions occurring within such an environment have been investigated by many researchers [1]-[6], and shown to be complex and only partly understood, especially in case of long length and large current arcs in high voltage GCBs. To develop higher voltage mechanical-puffer-less GCBs in future, this chapter describes some experiments conducted on high current, electromagnetically rotated electric arcs within such an environment. Moreover, interaction between the rotary-arcs and PTFE was also focused in this chapter, because it was found in Chapter 5 that the PTFE could affect interruption ability.

The experiments have been carried out by using different diameter PTFE chambers within which the electric arcs burn and also include a chamber without PTFE. The arcing atmosphere was SF_6 and arc currents up to 20 kA. Magnetic fields, up to magnetic flux density 1.1 T at chamber centre, were applied by a coil (B-field coil, herein after) which was set out of chamber cylindrically. The measurements have been taken with the time variation of arc current and B-field coil current, arc voltage, and dielectric strength below the arc gap.

Moreover, optical observations using high-speed photography and optical fibre probes have been made.

Empirical mathematical expressions have been derived from the experimental results to quantify the dependence of various electrical parameters such as post arc breakdown voltage and pre current zero voltage extinction peak. Operating conditions were variable on peak fault current, arc driving magnetic flux density and the dimensions of the arcing volume within the polymeric cylinders.

6.2 Experimental set up

6.2.1 Model chambers

Figure 6.1 shows the experimental model arc chamber which was arranged to observe the interaction among a rotary-arc, a magnetic field and an ablating material. The left half within glass fibre tube in Fig. 6.1 represents an opening position of the contacts and the right half represents a closing position. The contacts consisted of a stationary plate and a movable contact, which had a diameter of 24 mm and was withdrawn by a hydraulic mechanism of which the full stroke was 240 mm. A non moving ring electrode of 170 mm inner diameter was installed around the movable central contact, and connected to the stationary contact. All three were made of copper. A hollow PTFE cylinder was located centrally inside the ring electrode, within which the movable contact was allowed to move. All of these components were assembled in a glass fibre tube of 200 mm inner diameter, which was filled with SF_6 gas.

B-field coil was installed outside of the fibre tube, which enabled a magnetic field to be produced inside the chamber. The magnetic flux density at the centre of the B-field coil was calculated to be 1.1 T at a maximum energising current of 700 A.

It was expected that the arc would be transferred from the stationary contact to the ring electrode by the electromagnetic force after arc ignition between the stationary contact and the

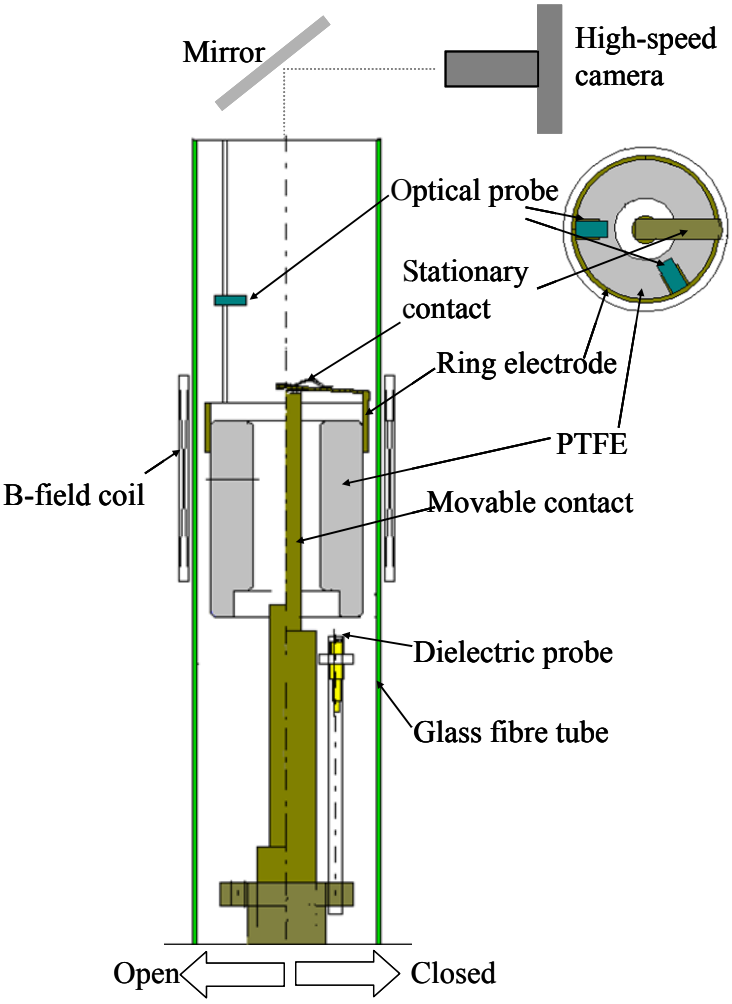

Figure 6.1 Experimental model chamber

movable contact. The experiments were conducted with different hollow diameters of 76 mm (large-bore) and 42 mm (small-bore). The 76-mm diameter was the cylinder itself and the smaller size was formed by a sleeve which was interchangeable. This is shown schematically in Fig. 6.2. In some tests, the cylinders or sleeves were removed to examine their condition.

6.2.2 Measurements

As shown in Fig. 6.1, a dielectric probe [7] was installed below the PTFE cylinder as shown to monitor the dielectric strength of the gas at that location to which hot gas possibly containing ablated material might expand.

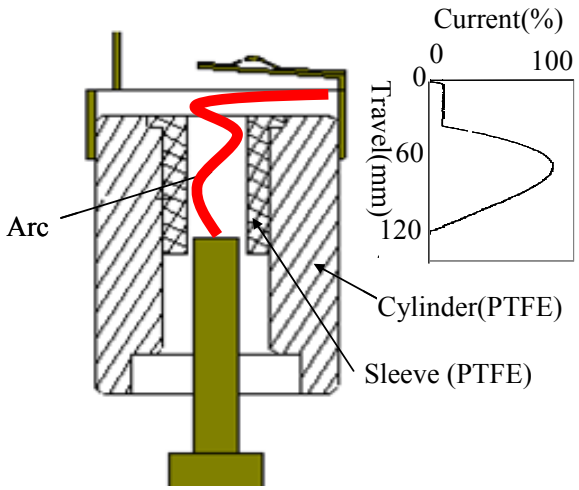

Figure 6.2 Detail of experimental chamber

High-speed photography was undertaken at a framing rate of up to 15000 frames/second observing the chamber through a window located within the top plate of the rig.

Two optical fibre probes [2][8] were set above the PTFE and the contacts, to observe light from the arc in the chamber. In the case of the presence of a cylinder, another optical probe was also installed in the wall of the PTFE, to observe light from the bore in which the arcs burned.

The main arc current and the coil current were measured by co-axial shunts, and a 1000:1 voltage probe was used to measure the arc voltage.

6.2.3 Test circuit

The electrical circuit for the experiment is shown in Fig. 6.3. There were two sets of capacitor banks, one for the main circuit including the arc and one for the B-field coil situated outside the arc chamber as shown in Fig. 6.1.

Ignitron 1 was triggered to permit current to flow in the coil. Then ignitron 2 in series with resistors was triggered to allow a small quasi steady DC current to flow. As the circuit breaker contacts opened and an arc was generated, ignitron 3 was triggered to short the

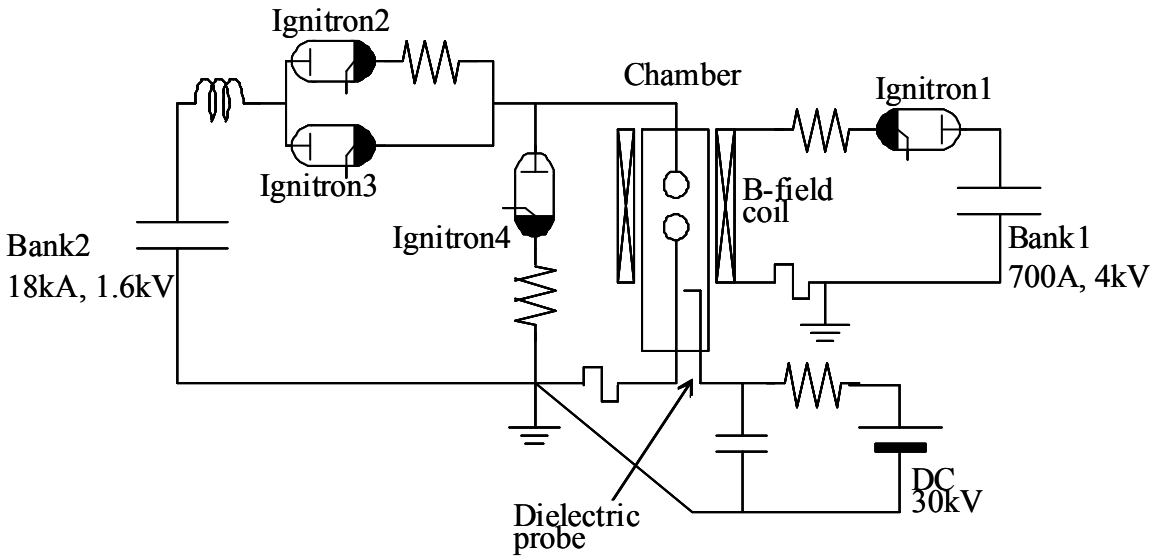

Figure 6.3 Experimental circuit

current limiting resistor, and then the main half cycle sinusoidal current was produced. Ignitron 4 was triggered 30 ms after the switching of ignitron 3 in order to dump the remaining capacitor bank charge.

The voltage for the dielectric probe was supplied by a capacitor, which was charged continuously from a high voltage DC supply via a current limiting resistor, and the dielectric probe was expected to break down repeatedly.

6.3 Experimental results

6.3.1 Waveforms

The main arc current consisted of a quasi-DC period followed by a main half-cycle AC. The arc voltage and the coil current were measured and are shown in Fig. 6.4. The coil current producing the magnetic field remained high while the main arc current continued, since the time constant of the coil current was relatively long. Figure 6.2 shows the position

of the tip of the movable contact as a function of the current waveform. The contacts of the circuit breaker separated at almost the same time as the start of the quasi-DC main current, and were separated by approximately 120mm at current zero of the main arc.

Outputs from the optical fibre probes were converted into electrical signals with electronic gain to detect optical emission around the current zero. Examples of the probe waveforms are shown in Fig. 6.4.

Waveforms of breakdown voltage on the dielectric probe are also shown in Fig. 6.4. This

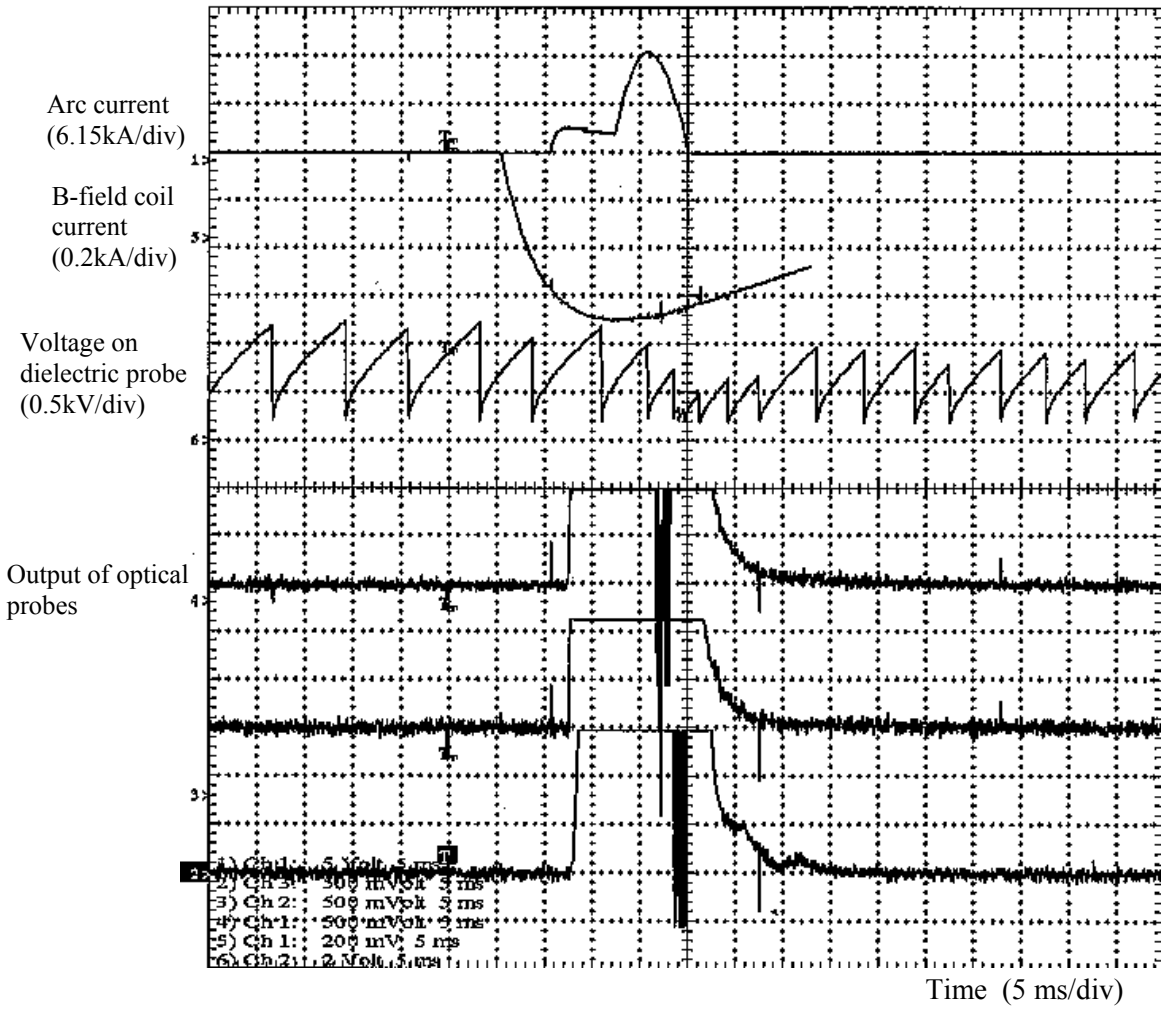

Figure 6.4 Examples of measured waveforms
- large-bore PTFE (diameter: 76mm)
- arc current: 12kA

waveform is a saw tooth nature with a gradual increase in voltage with time followed by an abrupt decrease to a base level. The gradual voltage increase is due to the time constant of the charging RC circuit in Fig. 6.3 whilst the abrupt decrease is due to the breakdown of the dielectric probe leading to a rapid voltage collapse across the probe. Thus the peak voltage to which the probe is gradually charged immediately before the voltage collapse yields the breakdown voltage of the gas in the electrode gap of the probe.

6.3.2 High-speed photographs

Figure 6.5 shows some examples of high-speed photographs taken during an arc test. The arc column was clearly visible as it rotated along the ring electrode. The arc column formed a spiral which was shortened intermittently with sometimes forming a multi-turned spiral, especially during the low currents before current zero as show in Fig. 6.5 (c).

6.3.3 Test conditions

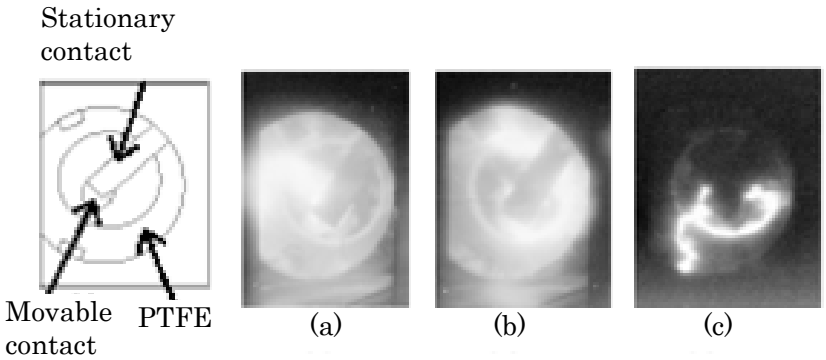

Figure 6.5 Examples of high-speed photographs of rotary arcs
- large-bore PTFE (diameter: 76 mm)
- arc current: 10kA
- coil current: 260A

(a) 1.4ms before current zero
(b) 1.1ms before current zero
(c) 0.1ms before current zero (last shot before extinction)

Table 6.1 Ranges of experiments and their symbols in following figures

	Coil current	
	260A	700A
No-PTFE	N/A	(＊)
Large-bore PTFE (diameter: 76 mm)	(●)	(○)
Small-bore PTFE (diameter: 42 mm)	(▲)	(△)

The experiments were performed under a range of different conditions. These are summarised in Table 6.1. Two levels of coil current were used with three different bore chambers (no-PTFE, small-bore, large-bore). The rig was filled by SF_6 gas at a pressure of 0.1 MPa.

Various results are given on Figs. 6.6, 6.7 and 6.8 where the different symbols (circles, triangles and stars) represent the particular experimental conditions as indicated in Table 6.1.

6.4 Data analysis

6.4.1 Arc voltage

6.4.1.1 Relation of arc voltage and arc length

Piotrowski and Wolny found that there were relationships between arc voltage and arc length in their small chamber of rotary-arcs [9]. To find the relationships for our chamber case, arc lengths L_{arc} were estimated from the contact travel characteristics of the breaker and photo images by using (6.1),

$$L_{arc} = \sqrt{{L_{2D}}^2 + {L_{travel}}^2}\ , \tag{6.1}$$

where, L_{2D} is length on the photo images which is two dimension and L_{travel} is distance from the stationary contact to the movable contact. The time variation of these parameters is shown in Fig. 6.6 along with arc voltage. Due to its spiral shape, the arc length was estimated to be as long as 0.3 m while the distance between contacts was only 0.12 m maximum.

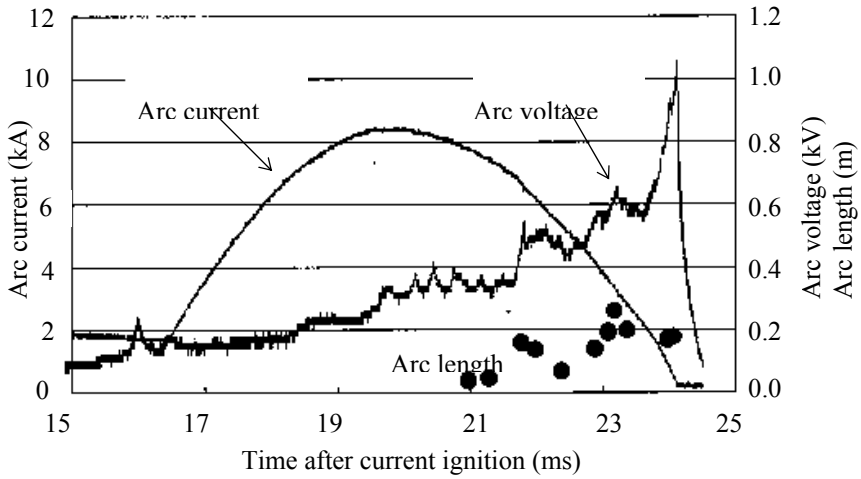

Figure 6.6 Arc voltage and arc length
- large-bore PTFE (diameter: 76 mm)
- arc current: 10kA
- coil current: 260A

Although small oscillations were not observable in the arc length data due to limitations of the frames rate of the photography, the arc voltage nonetheless varied in a similar manner to the arc length.

6.4.1.2 Extinction peaks

For a given current level just prior to current zero, a higher arc voltage is indicative of greater power dissipation (iV), hence a higher rate of energy loss from the arc plasma leading to more rapid arc extinction [10][11]. Therefore, the extinction peak on the arc voltage (V_{EXT}) before current zero is one significant indicator of current interruption ability. Extinction peaks on arc voltages are plotted against current peak values in Fig. 6.7. This figure suggests the following trends:

1. The extinction peaks for the higher magnetic field (open symbols) are higher than those for the lower field (closed symbols).
2. The extinction peaks for the large-bore chamber are higher than those for the small one.

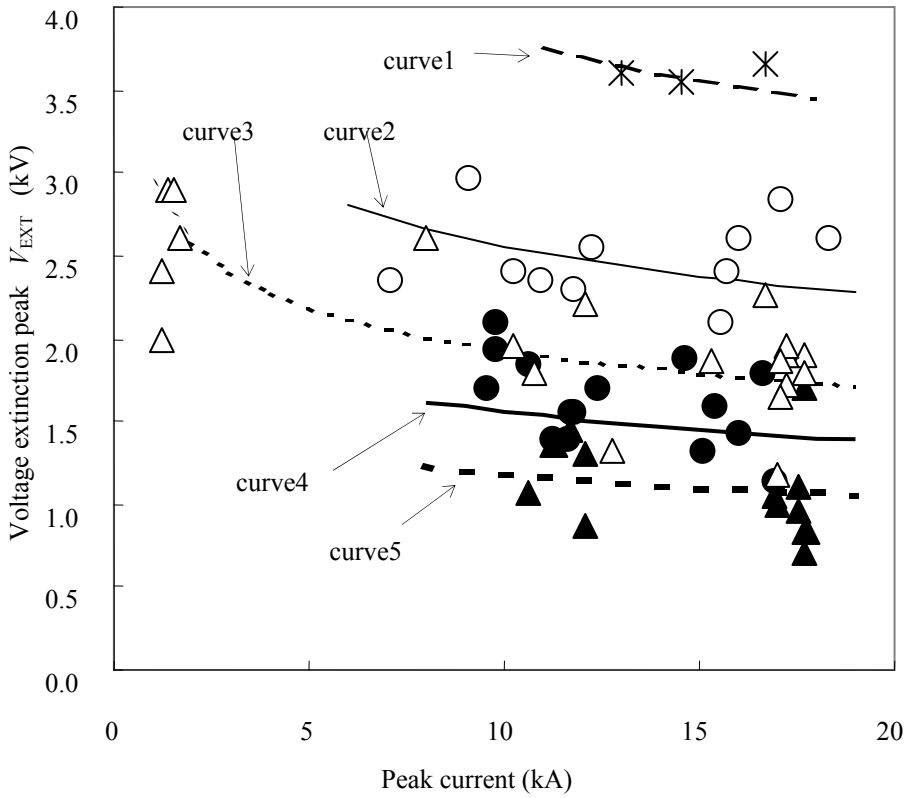

Figure 6.7 Extinction peak on arc voltage against current peak
- curve 1 : no-PTFE, coil current 700A
- curve 2 : large-bore PTFE, coil current 700A
- curve 3 : small-bore PTFE, coil current 700A
- curve 4 : large-bore PTFE, coil current 260A
- curve 5 : small-bore PTFE, coil current 260A
(See Table 6.1 for symbols)

3. The no-PTFE chamber had the highest peaks.
4. The extinction peaks for higher peak currents are lower in the small-bore chamber.

6.4.1.3 Current waveforms distortion

Rates of decrease of arc current (di/dt) before current zero against peak currents are shown in Fig. 6.8. The rate (di/dt) for an ideal sinusoidal waveform should be proportional to peak current and is shown as a dashed line on Fig. 6.8. However, most of measured di/dt values shown in Fig. 6.8 were higher than the ideal line, especially in the case of lower peak current conditions (corresponding to lower voltage charging (≤2.5 kV) of the capacitor bank). In

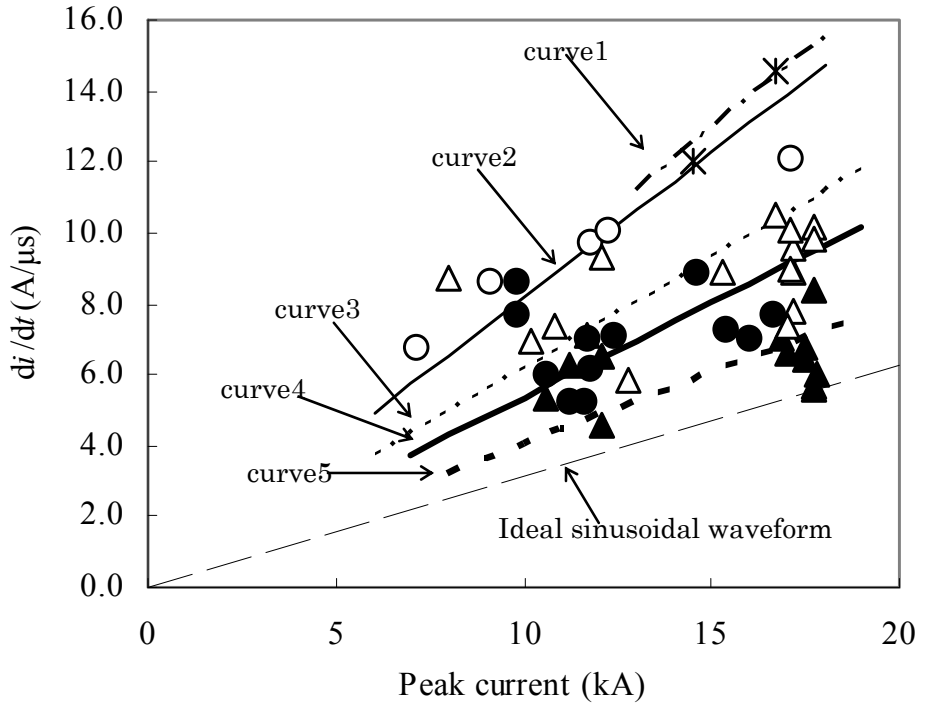

Figure 6.8 d*i*/d*t* against current peak values
- curve 1 : no-PTFE, coil current 700A
- curve 2 : large-bore PTFE, coil current 700A
- curve 3 : small-bore PTFE, coil current 700A
- curve 4 : large-bore PTFE, coil current 260A
- curve 5 : small-bore PTFE, coil current 260A
(See Table 6.1 for symbols)

other words, these higher (d*i*/d*t*) results correspond to higher equivalent 50 Hz peak currents.

6.4.2 Dielectric strength

Breakdown voltages determined with the dielectric probe are shown in Fig. 6.9 as a function of time after arc ignition for various operating conditions. The results are shown in term of the "ratio of breakdown voltage"($V_B^{(t)} / V_{BO}$) which is the ratio of the breakdown voltage ($V_B^{(t)}$) measured at a given time *t* after arc ignition to the breakdown voltage (V_{BO}) before arcing. This figure shows the following trends for the dielectric strength at the probe location.

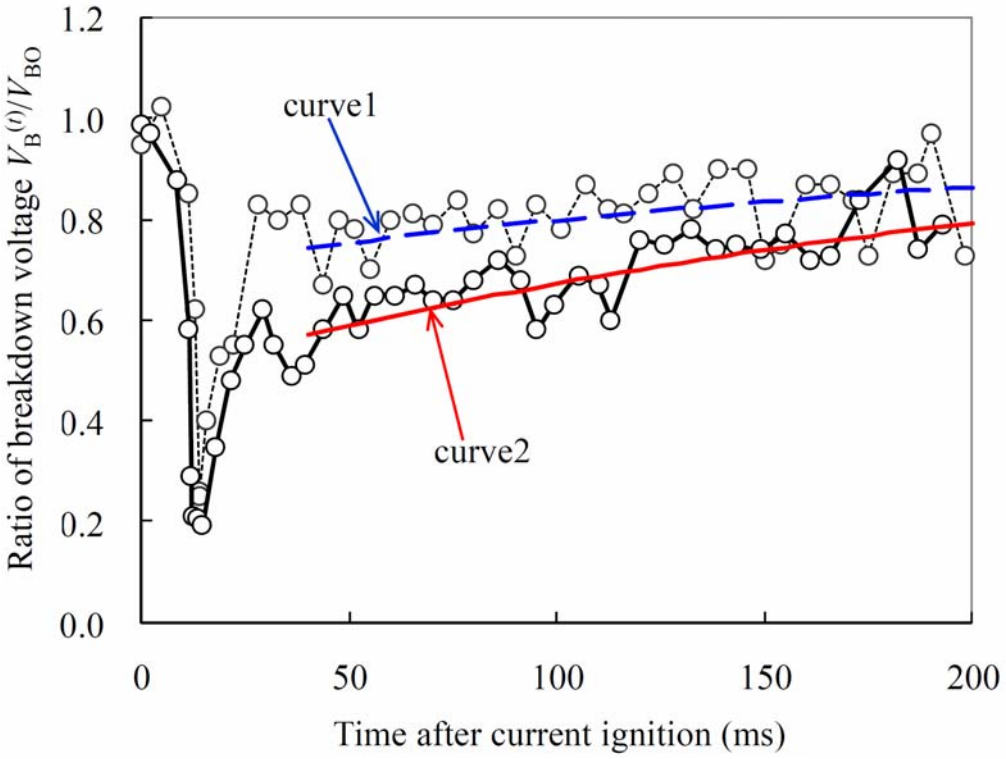

(a) High- and low- current

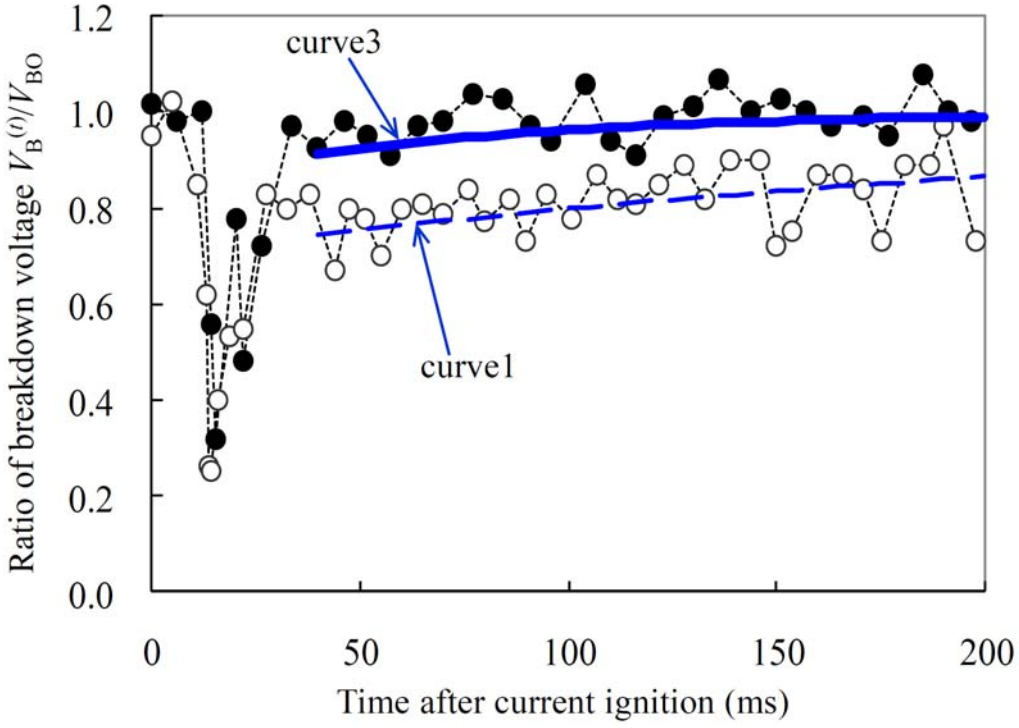

(b) High- and low- magnetic field

Figure 6.9 Breakdown voltage ration on dielectric probe (to be continued)

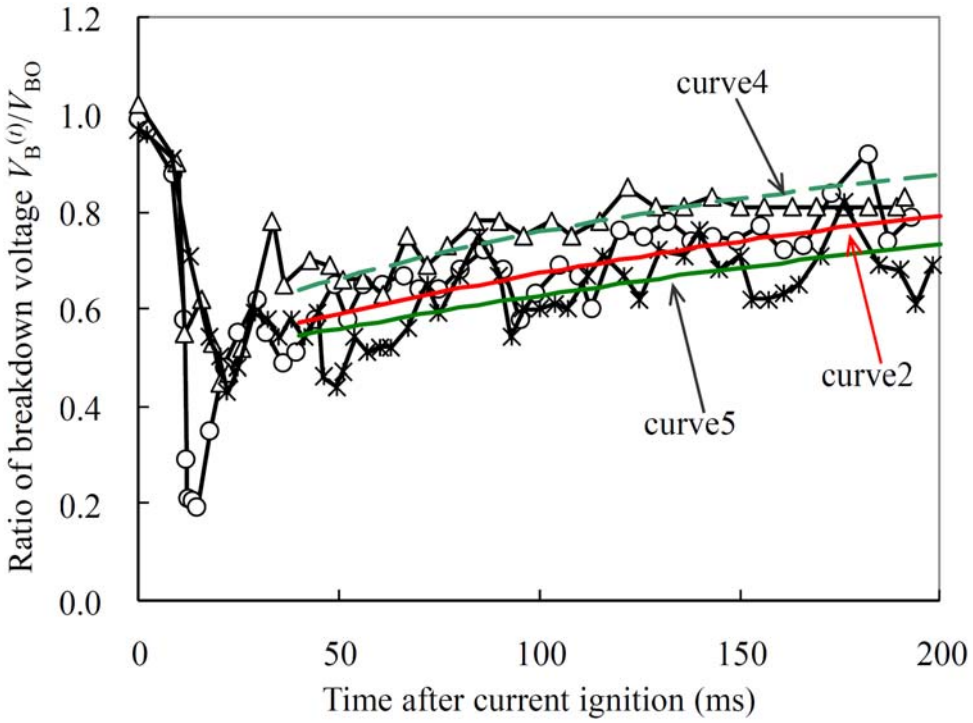

(c) Small- and large-bore PTFE, and No-PTFE

Figure 6.9 Breakdown voltage ration on dielectric probe
Experimental data
-solid lines: peak of arc current between 15-18kA
-dash lines: peak of arc current between 10-13kA
Approximated curves
-curve 1: large-bore PTFE, coil current 700A, arc current 10.2kA
-curve 2: large-bore PTFE, coil current 700A, arc current 16.0kA
-curve 3: large-bore PTFE, coil current 260A, arc current 9.5kA
-curve 4: small-bore PTFE, coil current 700A, arc current 17.2kA
-curve 5: no-PTFE, coil current 700A, arc current 13.0kA
(See Table 6.1 for plots symbols)

1. The dielectric strengths reduced sharply for 10 to 30 ms after current ignition before rapidly recovering.
2. The dielectric strengths after the recoveries were lower than the initial levels.
3. For higher current tests (solid lines), the dielectric strength reduced further than with lower currents (dashed lines).

4. The dielectric strength in large-bore PTFE tests dropped the most and no-PTFE the least.
5. In higher magnetic field tests, the dielectric strengths after the recoveries were lower than - in the lower magnetic field.
6. In small-bore PTFE tests, the dielectric strength after the recoveries were higher than that in large-bore PTFE or no-PTFE tests.

6.4.3 Luminous emission after current zero

6.4.3.1 Luminous images from high-speed photographs

Figure 6.10 shows photographs which were the first frames recorded after current zero with the different configuration of arc chambers. Luminous regions could be observed on images of the large and small-bore chambers which persisted for 4.5 ms in the large-bore chamber and 1.3 ms in the small-bore chamber. On the other hand, considerably less luminosity was observed after current zero in the case of the no-PTFE chamber.

6.4.3.2 Post arc signals on optical probes

The optical fibre probes also detected luminous signals after current zero as indicated by the records shown in Fig. 6.4. The signal continued for several tens of milliseconds, which was much longer than the persistence of the luminous emission on the photographic records. Significantly, this kind of post arc luminous signal appeared even with the no-PTFE chamber for the optical probes, while the luminousity was barely visible on the photographic records.

6.5 Discussion of results

The arc conditions investigated are complex involving electromagnetically driven (Fig. 6.3 and Fig. 6.4) convoluted arc columns (Fig. 6.5) within different annular spaces (Fig. 6.2), sustained by a sinusoidally varying current (Fig. 6.6), with dielectrically weakened gas post

arcing away from the main arc gap (Fig. 6.1) with evidence of persisting post arc luminosity (Fig. 6.10 and Fig. 6.4). Detailed theoretical modelling of such a complex environment is extremely difficult and beyond the scope of this chapter. However it is possible to draw upon the empirical modelling of previous publications in order to interpret results and to yield additional empirical models based on the present work.

A qualitative discussion of the results shown in Fig. 6.4 to Fig. 6.10 is presented first, followed by some empirical modelling based upon these results, and then some general operational principles can be derived.

6.5.1 Qualitative observations

The arc voltage and arc length results (e.g. Fig. 6.6) indicate that the arc voltage increases with the arc length which depends not only on the separation of the arc contacts but also the helical shape (pitch and radius) of the arc produced by the driving magnetic field. The latter effect is transitory since the helical arc may short circuit itself periodically [5] as indicated by fluctuations in arc length and the correlation with the periodic variations in arc voltage

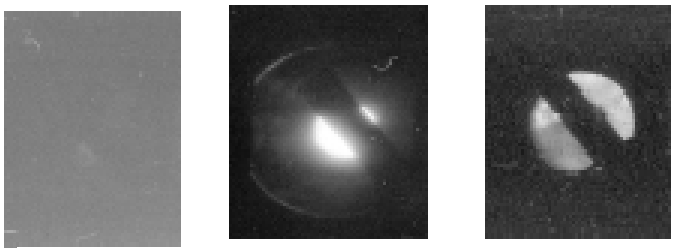

Figure 6.10 Luminous images after current zero
(a) no-PTFE, 0.08ms after current zero
arc current 16.7kA, coil current 700A
(b) small-bore PTFE, 0.08ms after current zero
arc current 17.7kA, coil current 700A
(c) large-bore PTFE, 0.13ms after current zero
arc current 11.2kA, coil current 700A

(Fig. 6.6). The longer arcs result in greater power dissipation due to increased ohmic losses. The arcs in the small-bore PTFE chamber are geometrically restricted so limiting the convoluted arc length compared with the no-PTFE chamber in which the arc is free to expand. However there are likely to be greater gas pressure rises in the small-bore chamber due to the containment of the hot gas [12]. On the other hand, it has been found that arc voltages per arc lengths along the helical shape were not constant but indicated high values in shorter arc lengths. For example, arc voltages per arc length are 2.9 and 2.4 kV/m at two local peaks while the values for shorter arcs are between 5.5 and 7.8 kV/m. This result suggests that the shorter arcs have a larger ohmic loss per unit length implying either a more constricted arc or a lower temperature plasma. Either way it indicates more severe power extraction from the arc which would encourage extinction.

The voltage extinction peaks in Fig. 6.7 are higher with a large magnetic field (open circles, triangles) compared with lower fields (filled circles, triangles). In the larger bore or no-PTFE (circle, asterisk), the extinction peak becomes higher due to less containment of hot gas around the arc and hence increased convection losses. As a result the voltage extinction peak decreases more strongly with peak current in the small-bore chamber compared with the larger chambers.

In Fig. 6.8, the steeper di/dt values observed at current zero with the higher magnetic field are caused by the increase in arc resistance due to elongation. The increment of arc resistance leads to the nature of the test circuit changing from being mainly capacitive in nature to a more resistive one.

In Fig. 6.9, the major reduction in breakdown voltage between 16-20 ms corresponds approximately to the main current half cycle through the arc. At longer times (approx. 30 ms) there persists reduced breakdown strengths except the large-bore chamber with lower magnetic field (curve 3). The reduced breakdown strength in the higher magnetic field (asterisks, open circles and triangles) may be explained in terms of the longer arc lengths

produced leading to increased heating of the surrounding gas which has a reduced dielectric strength [13] [14]. Utilising the data of the literatures [13][14] and assuming a constant gas pressure, relative breakdown strengths of 0.7 and 0.2 (Fig. 6.9) would correspond to SF_6 gas temperatures of 1800 K and 2500 K respectively. This implies that the gas close to the dielectric probe would be ionised.

The dielectric strength below the contacts was reduced to about 20 % of its nominal value, and then gradually recovered to levels dependent on chamber geometry and magnetic field at longer times (~150 ms) after arc interruption. A high-magnetic field in a no-PTFE condition enhances power dissipation from the arc with good early current zero recovery properties (i.e. high voltage extinction peaks). It nonetheless produces the worst dielectric recovery because of the excessive amount of thermal energy due to the high power dissipation from the arc.

The high-speed photographs in Fig. 6.10 and optical fibre measurements in Fig. 6.4 showed that luminous conditions persisted long after arc extinction in the PTFE based chambers but not in the non PTFE chamber. The optical fibre signal persisted longer than the photographic luminosity because the fibre instrumentation was more sensitive to infrared emissions. Thus the source of such long duration luminosity appears to be associated with ablated PTFE material rather than simply evaporated metallic contact material (copper) or SF_6 by-products. The luminosity may therefore be associated with the phosphorescence of PTFE [15] or glowing PTFE microparticles. The slowest recovery of breakdown voltage (asterisk, Fig. 6.9) occurred for the no-PTFE case for which little post arc luminosity was observed. On the other hand, the most rapid breakdown voltage recovery occurred for the large-bore with the low-magnetic field for which post arc luminosity occurred.

This kind of post arc luminosity has also been observed in conventional GCB. For example Uchii et al [14] have observed luminous gas on photographic images downstream of a circuit interrupter unit before electrical breakdown occurred. In the case of the present experiments such luminosity persistence was not observed in the absence of the PTFE

cylinders indicating that the effect is associated with PTFE related phenomena such as phosphorescence of glowing microparticles. This fact indicated that PTFE existed between contacts during current interruptions, which meant that considering PTFE in hot gas simulation as described in Chapter 5 was proper method.

The slow recovery of dielectric strength is not dominantly associated with such PTFE related luminous events since the most retarded recovery was observed in the absence of PTFE.

6.5.2 Empirical modelling

The results of Fig. 6.6 to Fig. 6.9 along with the qualitative discussions of section 6.5.1 enable some approximate empirical expressions to be derived. The empirical expressions describe the dependence of the thermal recovery of the arc gap and the dielectric recovery of the quenching gas (SF_6) remote from the arc gap upon the operating conditions.

The magnitude of the current zero extinction peak in Fig. 6.7 is indicative of the rate of energy dissipation in the extinguishing arc [10][11] and also therefore of the thermal recovery rate of the arc plasma. The post arc breakdown voltage in Fig. 6.9 is indicative of the longer term dielectric recovery of the arc heated gas well after arc extinction. Good thermal and dielectric recoveries are needed for successful current interruption.

The results shown in Fig. 6.7 yield the following approximate empirical relationship,

$$V_{\mathrm{EXT}} \cong K_1(1+\alpha_1 B)^{m_1} d^{n_1} i_{\mathrm{p}}{}^{-l_1}, \tag{6.2}$$

where, the parameters, B, d, i_{p}, are the magnetic flux density, the arc chamber diameter and the peak current respectively; K_1, α_1, m_1, n_1, l_1, are constants determined from Fig. 6.7 having the values 17.0, 1.5, 1.0, 0.47, 0.18 respectively for the operating conditions in this thesis. The curves corresponding to these constants are compared with the experimental data in Fig. 6.7. The effect of contact gap and background gas pressure are not included since they were both unchanged during the tests. The implications of the Eq. (6.2) are that for a given

peak current, large diameters and magnetic flux densities lead to higher extinction voltages. An increase in peak current i_p reduces the extinction voltage.

The results shown in Fig. 6.9 yield the following approximate empirical relationship for times greater than about 40 ms after arc initiation,

$$\frac{V_B^{(t)}}{V_{BO}} \cong 1 - K_2(1+\alpha_2 B)^{m_2} d^{n_2} i_p^{l_2} \exp[-t/\tau(B,d,i_p)], \tag{6.3}$$

where K_2 , α_2 , m_2 , n_2 , l_2 , are constants determined from Fig. 6.9 having the values 3.3×10^{-6}, 1.6, 1.1, 0.3, 1.2 respectively for our operating conditions. $\tau(B,d,i_p)$ represents a dielectric recovery time constant which is a function of B, d, i_p also derived from Fig. 6.9. The curves corresponding to these constants are compared with the experimental data in Fig. 6.9, where the values of $\tau(B,d,i_p)$ are 150, 250, 70, 220, 300 for the curves 1 to 6 respectively. The effects of contact gap and gas pressure are not included. The implications of the Eq. (6.3) are that for a given fault current, large hollow diameters and magnetic flux densities lead to a substantial lowering of breakdown voltage remote from the arc gap which can be as low as 70 % of the pre arc breakdown voltage even 200 ms after arc extinction. An increase in peak current i_p reduces the breakdown voltage substantially.

The results of Fig. 6.8 lead to the following empirical relationship between peak current i_p and di/dt for our particular test circuit,

$$\frac{di}{dt} \cong i_p K_3 d(1+\alpha_3 B), \tag{6.4}$$

with α_3 a constant determined from the results Fig. 6.8 having the value 1.1. K_3 represents a constant which is a function of d determined from Fig. 6.8, and has the values 280, 370, 390 for small, large-bore and no-PTFE chamber respectively in the case of our operating conditions. The curves corresponding to these constants are compared with the experimental data on Fig. 6.8. The implications of the Eq. (6.4) are that the rate of decrease before current zero increases more rapidly than the natural rate of a 50/60-Hz current wave (i.e.

$\mathrm{d}i/\mathrm{d}t \cong i_\mathrm{p} K_3 \alpha_3$), and the extent of the deviation increases with hollow diameter d and magnetic flux density B. As already indicated in Section 6.1, this effect is associated with the capacitive-resistive nature of the arc test circuit interaction.

Figure 6.11 shows summary of the above-mentioned arguments.

Inspection of Eqs. (6.2) and (6.3) shows that for a given peak current i_p the effects on $V_\mathrm{B}^{(t)}/V_\mathrm{BO}$ and V_EXT respectively are contrary to each other in that lower values of d and B are needed to maximise $V_\mathrm{B}^{(t)}/V_\mathrm{BO}$ whereas higher values of d and B are needed to maximise V_EXT.

Since $V_\mathrm{B}^{(t)}/V_\mathrm{BO}$ and V_EXT are indicators of dielectric and thermal recovery strengths respectively, the relative trends of dielectric and thermal recovery with respect to changes in

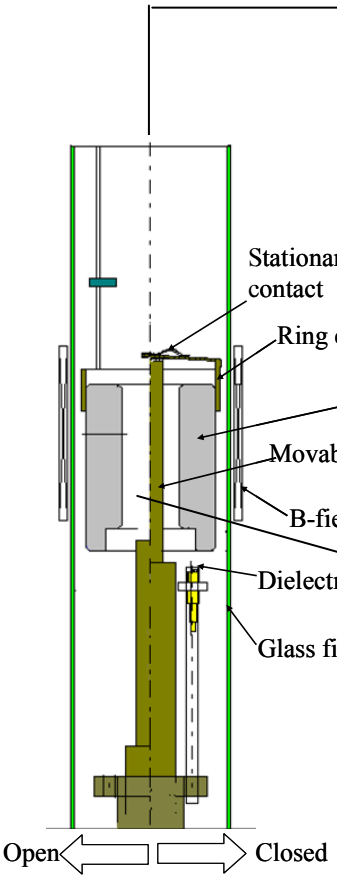

	Thermal recovery (Extinction peak of arc voltage) V_EXT	Dielectric strength V_B	Rate of decrease of current $\mathrm{d}i/\mathrm{d}t$
Bore d	d: large V_EXT: high	d: large V_B: low	d: large $\mathrm{d}i/\mathrm{d}t$: large
Magnetic field B	B: large V_EXT: high	B: large V_B: low	B: large $\mathrm{d}i/\mathrm{d}t$: high
Arc current i_p	i_p: large V_EXT: high	i_p: large V_B: low	i_p: large $\mathrm{d}i/\mathrm{d}t$: high

$$V_\mathrm{EXT} \cong K_1 (1+\alpha_1 B)^{m_1} d^{n_1} i_\mathrm{p}^{-l_1} \tag{6.2}$$

$$\frac{V_B^{(t)}}{V_{BO}} \cong 1 - K_2 (1+\alpha_2 B)^{m_2} d^{n_2} i_\mathrm{p}^{l_2} \exp[-t/\tau(B,d,i_\mathrm{p})] \tag{6.3}$$

$$\frac{\mathrm{d}i}{\mathrm{d}t} \cong i_\mathrm{p} K_3 d (1+\alpha_3 B) \tag{6.4}$$

Figure 6.11 Summary of effects on the chamber

$n_2 < n_1$, so that increasing B would lead to proportionately a stronger degradation of dielectric strength, and d would be opposite.

The stronger degradation of dielectric recovery compared with thermal recovery should not be regarded negatively. Because the opposite trend (i.e. thermal degrading more strongly than dielectric) implies that the subsequent potential dielectric recovery is irrelevant to d or B, which means the dielectric recovery ability cannot be improved by adjusting the d or B. What might be regarded as optimum would be for the degradation in both thermal and dielectric recovery to be similar and minimised. In principle the Eq. (6.5) allows such a condition to be sought by identifying appropriate values for m, n, l. This result suggests that thermal and dielectric recovery ability can be controlled in practical GCBs in future.

6.6 Conclusions

Results of experiments performed on rotary-arcs in hollow polymeric cylinders have been summarised. Voltage, dielectric strength and optical measurements have been obtained.

The results show that the arc voltages are affected by the presence and configuration of the PTFE (polymeric) cylinders. The fact that more constraining the PTFE geometry generates lower arc voltages leads to the conclusion that arc length was probably the more dominating factor.

The experimental results reported under a range of different conditions have enabled empirical mathematical equations to be derived for quantifying trends of parameters $V_{\mathrm{B}}{}^{(t)}/V_{\mathrm{BO}}$ and V_{EXT} which are indicative of thermal and dielectric recovery, which involves operating conditions i_{p}, B, d and t. Overall the dielectric recovery appears to degrade more rapidly than the thermal recovery as the operating parameters are changed. The empirical expressions therefore allow some approximate predictions to be made a priori for producing performance conditions to meet different operational needs.

Following arc extinction both high-speed photographic records and optical fibre probe results show the persistence of luminosity post arc extinction for periods of tens of milliseconds in the presence of PTFE. The persistence of luminosity is at best only a secondary consideration in the reduction of breakdown strength at post arcing.

The results on this chapter are expected to contribute to application on rotary-arc-type GCBs in future. The fact that dielectric strength under the interruption chamber becomes lower for larger magnetic field means larger amount of hot gas energy spreads to the area. This suggests that if the rotary-arc is set in the self-blast -type chamber, hot gas energy spreads in the thermal chamber and pressure possibly rise higher effectively. It is also useful information that the thermal interruption ability and dielectric strength can be controlled by magnetic field, chamber diameter. A translation of those conditions into the practice would require further investigation.

References

[1] H. Sasao, S. Hamano, Y. Wada, H. Hasegawa and N. Kobayashi: "Development of a magnet-assisted autopuffer GCB", *IEEE 90 WM 158-6 PWRD*, 1990

[2] K. A. Young and J. W. Spencer: "Optical diagnostics for studying a rotating arc in SF_6 gas", *Proceedings of 14th International Conference on Gas Discharges and their Applications*, Vol.II, pp.353-356, September 2002

[3] Y. Kittaka: "Outline of XAE7-type 72/84 kV GIS for general consumers", *Electrical Review*, pp. 32- 35, March 2004.

[4] L. Niemeyer, W. Widl: "Rotating arcs in SF_6-circuit-breaker", *Proceedings of 9th International Conference on Gas discharge and their applications*, Venezia, pp95-98, September 1988

[5] M. G. Ennis: "Investigation of fundamental processes affecting the behaviour of electric arcs in electromagnetic interrupters", Thesis for PhD. at the University of Liverpool, April 1996

[6] A. D. Wonlny and A. D. Stokes: "Effect of axial magnetic field on ablation arc", *Proceedings of 12th International Conference on Gas Discharges and their applications*, Vol.I, pp.131-134, September 1997

[7] H. Oohashi, J. W. Spencer and G. R. Jones: "The recovery of dielectric strength of SF_6 and air", *Proceedings of 21st International Conference on Phenomena in Ionised gas*, Vol.2, pp.66-67, 1993

[8] J. W. Spencer and G. R. Jones: "Fibre optic monitoring of electrical discharges", *IEE Colloquinm on Measurement and Plasmas*, 1997

[9] J. B. Piotrowski and A. D. Wolny: "Longitudinal magnetic field effect on arc voltage of electric arcs confined in organic enclosures", *Proceedings of 13th International*

Conference on Gas Discharge and their Applications, Vol.I, pp.190-193, September 2000.

[10] G. R. Jones: "High pressure arcs in industrial devices", Cambridge University, ISBN 0 521 331285, 1988

[11] C. H. Flurscheim: "Power circuit breaker theory and design", Peter Peregriuns Ltd. (IEE), ISBN 0 906048 70 2, 1982

[12] H. M. Ryan and G. R. Jones: "SF_6 switchgear", Peter Peregriuns Ltd. (IEE), ISBN 0 86341 123 1, 1989

[13] G. J. Cliteur, Y. Hayashi, E. Haginomori, and K. Suzuki: "Calculation of the uniform breakdown field strength of SF_6", *IEEE Transactions on DEI*, Vol.5, No.6, pp.843-849, 1998

[14] T. Uchii, T. Nakamoto, S. Nishiwaki, M. Toyoda, K. Bannai and S. Higashi: "Investigation of hot gas behavior during a large current interruption for a compact and reliable dead-tank-type GCB", *Proceedings of cigre SC15 annual meeting*, Dubai, UAE, May 2001.

[15] R. S. Becker: "Theory and interpretation of fluorescence and phosphorescence", John Wiley & Sons, Inc., 1969, (translated into Japanese by Y. Kanda, Tokyo Kagaku Dozin Co., Ltd., 1971)

Chapter 7 Summary

7.1 Introduction

This thesis contributed to development of compact and reliable GCBs through some types which are Hybrid-puffer^{TM}-type, advanced Hybrid-puffer^{TM}-type, tandem-puffer-type, and rotary-arc-type for the future products. The direction of the changing types of the interruption chambers was 'using thermal energy to raise puffer chamber pressure' to minimise required energy on operating mechanisms. Many kinds of experiments and simulation along with improvements of simulation programs have been carried out. This chapter summarise the thesis.

7.2 Summary of the thesis

In Chapter 2 technologies for developing new 300-kV 63-kA GCB keeping its size the same with 300-kV 50-kA GCB were discussed.

An inner-nozzle has employed to control the mass-flow properly in high current interruption and to cool arcs effectively. It was found that the inner-nozzle successfully improved the balance of the arcing energy to be cooled by mass-flow of two directions, and contributed to improvement of short-line fault (SLF) interruption ability. Combined use of the Hybrid-puffer^{TM} and an inner-nozzle was effective on the efficient pressure rise in a puffer chamber. The friction of gas pressure around arcing contact was measured to improve the small capacitive current interruption, and it was also found that the inner-nozzle affected on it favourably. The large current interruption was achieved successfully with investigation hot gas-flow measurements and simulation.

As the results, the new 300-kV 63-kA GCB was successfully developed with compatibility

to the conventional 50-kA GCB.

The knowledge found on this chapter has also contributed to developments of other new Hybrid-puffer^{TM}-type GCBs.

In Chapter 3, on the purpose of developing 245-kV 50-kA GCB with operating mechanism of 1500 J, 2vol-2pis and 1vol-1pis interruption chambers were compared from viewpoints of opening characteristics by one-dimensional simulation of puffer pressure and travel characteristics.

It was confirmed that both of interruption chambers could satisfy required pressure rise for SLF90% (L90) interruption, and could be operated without unusual travel characteristics by repulsive force on puffer piston in breaker-terminal fault (BTF) with rating interruption current. As the results, 1vol-1pis was selected for a further investigation as a new product as the advanced Hybrid-puffer^{TM}-type chamber.

In Chapter 4, the hot-gas-flow simulation called the modified fluid-in-cell (FLIC) was improved for the advanced Hybrid-puffer^{TM}-type GCB chamber. The advanced Hybrid-puffer^{TM}-type chamber took more amount of hot gas energy from arcs. Therefore, the gas pressure in the puffer chamber and arcing area was expected much higher than that of the Hybrid-puffer^{TM}-type chamber.

The thermodynamic and transport properties of SF_6 gas were considered for the gas pressure up to 10 MPa and gas temperature up to 30000 K. The simulation results by the modified FLIC taking into account these values gave lower puffer pressures which were closer to measured values.

Movable parts in a GCB were moved in the new method simulation Movable parts Moving Method (MMM) rather than Stationary parts Moving Method (SMM). In a comparison of MMM and SMM with the new range of gas properties in both of them, MMM resulted in

better agreements with the experimentally measured values than in SMM. This difference on puffer pressure also resulted in later and lower drops of density at the top of exhaust cylinder in MMM, which had to be much closer to real phenomena. It was found that the differences between MMM and SMM arose from differences on movement of holes on an operating rod, and MMM should be employed for precise simulation when the holes moved in the puffer chamber.

The simulation methods were adapted to develop new GCBs of 145- and 245-kV.

In Chapter 5, tandem-puffer-type chambers which had a thermal chamber and mechanical compressive chamber in series were subject to be considered under demands for adopting spring operating mechanism of which output force decreased in an operation. The tandem-puffer-type chamber raises gas pressure in the thermal chamber by arcing energy in the large current interruption. Therefore, the hot gas should be modelled more precisely than ever.

Thermodynamic and transport properties of SF_6-PTFE mixed gas were calculated and introduced hot-gas-flow simulation program the modified FLIC. It was found that the results were better agreement to experimental results than before. This indicated that one of the important mechanisms of pressure rise in a tandem-puffer-type chamber was gas properties along with temperature rise and mass contamination.

Furthermore, taking account of arcing diameter according to the properties was one of the relevant factors.

In Chapter 6, as an investigation for a future chamber requiring less operating energy, experiments have performed on rotary-arcs in hollow polymeric cylinders. Arc voltage, dielectric strength and optical measurements were measure on long gap arcs with external magnetic field.

The results show that the arc voltages are affected by the presence of the applied magnetic

field and configuration of the PTFE (polymeric) cylinders.

The dielectric strength below the interrupter unit was reduced to about 20 % of its nominal value during arcing before gradually recovering to levels dependent on chamber geometry and magnetic field at longer times (~150 ms) after arc interruption. The most effective recovery was shown by the large-bore PTFE with low-magnetic field: the worst recovery was shown by the no-PTFE high-magnetic field condition.

The fact that arc voltage and dielectric strength under the chamber vary is that interruption ability will be controllable by the parameters, such as external magnetic field and diameter of arc channel, in development of a rotary-arc-type chamber in future.

7.3 Future works

Gas circuit breakers are still expected to become more compact, low cost with high reliability. Especially the low-cost GCBs are required in international market. Therefore, GCBs which require only low operating mechanism will be preferable ongoingly.

One of solutions for reducing operating mechanism is self-blast -type interruption chamber, and the tandem-puffer-type chamber is the most practical application at this moment. The tandem-puffer-type chamber has been put into practical use, but up to 300 kV of rated voltage so far. The tandem-puffer-type chamber will be expected to be applied to GCBs of up to 550 kV of rated voltage. It will be necessary to study phenomena in the tandem-puffer-type chamber, especially dielectric interruption mechanism of middle current. Small and large current interruption phenomena have been well studied by many researchers, including this thesis. But it can be pointed out that the middle current region which can be one of important issue for higher voltage tandem-puffer-type GCB has not investigated enough.

Furthermore, rotary-arc-type GCB is one of possibility to the future GCBs. The effect of rotation of the arc is expected to be large, but it has not investigated well on high voltage

GCB applications. The rotary-arc effects may assist interruption of middle current on the tandem-puffer-type GCBs, for example, or even complete self-blast-type GCB may become in use.

Recently, alternative gases of SF_6, CO_2 for example, are expected to be in use for environmental reasons, but no-gases are superior to SF_6 gas. The technology described in this thesis will be able to contribute coming development of the alternative GCB. Hot gas simulation will be useful and important tools for the development, and the rotary-arc effects may fill the gap of the interruption ability between SF_6 and alternative gases.

The other approach to the future circuit breakers is to reduce duty on the circuit breakers. The demand for power electricity will become larger and fault current can be large, which results in heavy duties on the circuit breakers. To prevent the heave duties, current limiting apparatus on the power electricity network will be very useful, but there will be no practical ones for the purpose. It will be worth to study such kind of apparatus for the future.

Acknowledgements

First, I would like to appreciate to Professor Toshiro Matsumura at Nagoya University for invaluable advice and discussion with kind effort on the thesis.

I would like to express gratitude to Professor Hitoshi Okubo at Nagoya University for reviewing and insightful discussing on research work.

I am deeply grateful to Professor Hideyuki Ohno at Meijo University for taking the time and effort to review the thesis.

I am indebt to Associate Professor Yasunobu Yokomizu at Nagoya University for continuous encouraging and discussion on the thesis.

Professor Yasunori Tanaka at Kanazawa University made enormous contribution to the research shown in the thesis, and I want to express my gratitude.

My deepest appreciation goes to Professor Gordon R. Jones and Professor Joseph W. Spencer at the University of Liverpool for guiding research work and kind hospitality during my stay at Liverpool.

Special thanks to Dr. Katsumi Suzuki at Toshiba Corporation for conducting and encouraging research and progress of the thesis. I owe a very important debt to Dr. Katsuharu Iwamoto at Toshiba Corporation for contributing to research on simulations and experiments on gas-flow. I would particularly like to thank to Dr. Hitoshi Mizoguchi at Toshiba Corporation for conducting and advices on research and development.

I would like to thank Mr. Tetsuya Nakamoto, Mr. Hiromichi Kawano, and members of High Power Technology Group for progressing research and development GCBs together.

Finally, I want thank to my wife Yukiko and daughter Miharu for their support and encouragement.

List of Papers Concerned with this Thesis

Chapter	Title	Journal & Date	Authors
2	Investigation of technology of developing large capacity and compact size GCB	IEEE Trans. on Power Delivery, vol. 12, pp. 747-753, Feb. 1997	T. Mori H. Ohashi H. Mizoguchi K. Suzuki
3	Investigation of two types of interrupting chamber with low drive energy and development of 245-kV GCB	IEEE Trans. on Power Delivery, vol. 10, pp. 158-167, Jan. 2004	T. Mori H. Mizoguchi N. Kato M. Toyoda
4	Gas flow simulation with contact moving in GCB considering high-pressure and high-temperature transport properties of SF_6 gas	IEEE Trans. on Power Delivery, Vol.20, No.4, pp. 2466- 2472, Oct. 2005	T. Mori K. Iwamoto H. Kawano Y. Tanaka E. Kaneko
5	Gas flow simulation in GCB chambers featuring hot gas energy	IEEJ Trans. on Power and Energy, Vol. 125, No. 8, pp. 771-776, Aug. 2005	T. Mori K. Iwamoto H. Kawano Y. Tanaka
6	Diagnostic measurements on rotary arcs in hollow polymeric cylinders	IEEE Trans. on Power Delivery, Vol. 20, No. 2, pp.765-771, April 2005	T. Mori J. W. Spencer J. E. Humphries G. R. Jones